FACULTY OF SCIENCE
UNIVERSITY OF COPENHAGEN

Rastin Matin

Towards Continuous Cavity-Enhanced Nonlinear Spectroscopy in Strontium

Master's Thesis
January 2013

Towards Continuous Cavity-Enhanced Nonlinear Spectroscopy in Strontium

Prepared by
Rastin Matin

Academic advisors
Jan W. Thomsen
Philip G. Westergaard

Quantum Optics and Ultracold Atoms Group
Niels Bohr Institute
University of Copenhagen
Blegdamsvej 17
DK-2100 København Ø
Denmark

www.nbi.ku.dk

This thesis is submitted in partial fulfilment of the requirements for the degree of M.Sc. at University of Copenhagen and represents 60 ECTS points.

Abstract

The improvement in the stability of current optical atomic clocks is obstructed by the linewidth of the clock laser that interrogates the atomic transition. The linewidth of the clock laser is reduced by referencing it against an optical cavity, but cavity length fluctuations due to thermal noise in the mirrors limit the attainable linewidth. This thesis is concerned with theoretical and experimental work that seeks to realize an alternative proposal, which allows stabilizing the clock laser using direct spectroscopy of an ultranarrow optical transition, thereby circumventing the limiting thermal noise. In this respect we show that the nonlinear physics behind the proposal can be derived classically. Additionally, we trap strontium atoms magneto-optically for subsequent spectroscopy. We also suggest an experimental design, which we numerically show is capable of realizing this stabilization proposal in a continuous fashion.

Resumé

Forbedringer i stabiliteten af optiske atomure er begrænset af liniebredden af clock laseren, der interrogerer den atomare overgang. Liniebredden af clock laseren reduceres ved at referere den mod en optisk kavitet, men fluktuationer i kavitetslængden grundet termisk støj i spejlene begrænser den opnåelige liniebredde. Denne afhandling beskæftiger sig med teoretisk og eksperimentielt arbejde, der søger mod at realisere et alternativt forslag, der tillader at stabilisere clock laseren ved brug af direkte spektroskopi på en ultrasmal atomar overgang, hvorved den begrænsende termiske støj omgås. I denne forbindelse viser vi, at den ikke-lineære fysik bag dette forslag kan udledes fuldstændig klassisk. Endvidere fanger vi strontium atomer magneto-optisk med efterfølgende spektroskopi. Desuden foreslår vi et eksperimentielt design, som vi numerisk viser er i stand til at realisere dette forslag kontinuert.

Contents

Chapter 1

Prologue

1.1 Introduction

An atomic clock is based on the same principles as any other clock: A laser acts as the local oscillator (LO), whose frequency has to be referenced against a discriminator largely independent of its environment in order to counteract noise and drift. An atomic transition is an excellent realization of this passive, stable standard. The signal obtained from interrogating the transition depends on the LO frequency and from it the discrepancy between LO and transition frequency can be deducted, whereby the former can be corrected. It is thus possible to represent the atomic transition through the LO by utilizing a proper servo loop.

A timekeeping device is generally characterized by its frequency instability and accuracy, where the latter refers to the difference in the measured oscillation frequency relative to the nominal value. In the framework of atomic clocks it depends on how well systematic shifts in the measured frequency due to environmental perturbations (such as AC Stark shifts, Zeeman shifts, etc.) of the transition can be accounted for. The instability is expressed in terms of the Allan deviation, quantifying how well the device can produce the same oscillation frequency over a given measurement time. An accurate oscillator must then necessarily display low instability over long time scales.

Several noise processes contribute to the Allan deviation, the most fundamental being that of quantum-projection noise (QPN): Quantum fluctuations during detection of the atomic excitation result in white noise, which ultimately sets the lower limit for atomic clocks. The frequency instability for a QPN-limited system after an averaging time τ is characterized by the fractional Allan deviation [1]

$$\sigma_y(\tau) \simeq \frac{1}{\mathrm{SNR}} \sqrt{\frac{1}{Q^2} \frac{T_c}{\tau}}, \tag{1.1}$$

where $Q = \nu/\delta\nu$ gives the experimentally resolved line quality factor of the clock transition and $\mathrm{SNR} = \sqrt{N}$ the signal-to-noise ratio achieved during the clock cycle duration $T_c \leq \tau$.

The ground state hyperfine transition $\left|F = 3, m_F = 0\right\rangle \rightarrow \left|F = 4, m_F = 0\right\rangle$ of Cs is well suited as a reference because of its relatively high transition Q-value approaching 10^{11}. In fact, the second is defined as "the duration of 9 192 631 770 periods of the radiation corresponding to the transition between the two hyperfine levels of the ^{133}Cs atom". The primary standard set by this microwave transition has reached the limit set by the QPN, reaching instabilities at the $10^{-14}/\sqrt{\tau}$-level when interrogated with a cryogenic sapphire oscillator [2]. This corresponds to the clock losing one second every $\sim 10^7$ year, given an averaging time 1 s.

To lower the long-term instability further, current work is focused on utilizing optical transitions with frequencies $\sim 10^{15}$ Hz, which increases the Q-factor by almost five orders of magnitude given all other parameters are kept constant. Many systematic effects are reduced by moving to this part of the spectrum, since the relative frequency bias due to frequency-independent external perturbations is scaled down accordingly. The bane of working with these frequencies is that conventional electronics only provide sufficient resolution to measure microwave frequencies, not optical frequencies. However, the link between the microwave and optical domain has been established by the recent development of high-resolution octave-spanning frequency combs [3]: By heterodyning the optical stabilized LO with the closest comb line, a beat frequency in the microwave domain is created, which is then readily measured. Given that the comb is referenced to the primary Cs standard, it is thus possible to extract the absolute optical frequency of the LO through this downconversion. The beat frequency with other modes conveniently falls outside the bandwidth of current detectors.

Other sources of white noise originate from shot-noise limited detection and LO noise through aliasing effects. The latter affects the instability, since current optical clocks are sequentially operated: The interrogation time, during which the LO noise is determined, only constitutes a fraction of the total clock cycle duration. The rest of the sequence consists of technical issues such as prepation of atoms and readout, referred to as dead-time. As interrogation happens periodically, the atoms downconvert certain high Fourier-frequency noise components of the stabilized LO. This is referred to as the Dick effect after John Dick, who first adressed it [4]. Following [5, 6], this is neatly illustrated by taking as LO frequency fluctuations a perfect sine with zero average, whose frequency does not coincide with that of the interrogation cycle: Sampling the sine only partially results in a percieved error which the servo incorrectly counteracts, offsetting the stabilized LO from the transition by a different amount after each correction. This serves as a motivation for increasing the interrogation time, since stability degradation due to this aliasing phenomenon is practically eliminated for continuously operated systems. In turn this puts high requirements on the LO, since the interrogation time is bound by its coherence time.

1.1.1 Neutral Atom Clocks

Current state-of-the-art optical clocks are based on using $\sim 10^3$ neutral atoms trapped in an optical lattice, ensuring that motional effects such as the first-order Doppler broadening are suppressed. In one dimension such lattices are created by retro-reflecting a single red-detuned beam capable of dipole trapping, thus creating an interference pattern of high-intensity regions separated by half the wavelength in which the atoms are held. The strength of the harmonic potential determines the degree of suppression, characterized by the Lamb-Dicke parameter [7]. In this limit the photon recoil energy is absorbed more by the lattice than the atom itself such that recoil effects are also suppressed. The lattice is operated at the magic wavelength, where the AC Stark shift of both levels compromising the clock transition cancels out [8], which would otherwise obstruct a precise frequency measurement. Since the trap constitutes a conservative potential, the process leading to this confinement must go through several initial stages of laser cooling.

To begin with atoms effuse out of a resistively heated oven. In the specific case of Sr the vapor pressure is low ($\simeq 1\,\mathrm{Pa}$ at $523\,^\circ\mathrm{C}$), so the oven has to be heated to 500–600 °C in order to obtain an appropriate output flux. At these temperatures atoms have thermal velocities approaching $500\,\mathrm{m/s}$ due to which they have to be decelerated before lattice confinement. The most common approach is to employ a Zeeman slower, consisting of a spatially varying magnetic field along the atomic propagation axis. Its purpose is to compensate the changing

first-order Doppler shift associated with the atomic deceleration by a corresponding Zeeman shift in order to keep the atoms resonant with the decelerating laser beam, which has a fixed detuning. After reaching velocities around 30 m/s the atoms are able to be captured by a standard magneto-optical trap. Depending on the specific transition for the trap, the atoms are cooled down to the μK-level such that they can be transferred to the optical lattice.

These optical lattice clocks have the immediate advantage that the SNR is very favorable due to the large number of simultaneously interrogated atoms in addition to long interaction times approaching 1 s, thereby also increasing the resolution $\delta\nu$. These clocks operate with alkaline earth-like atoms such as Sr and Mg since they have a magic wavelength, but also due to the broad $\left|{}^1S_0\right\rangle \rightarrow \left|{}^1P_1\right\rangle$ transition, which is used for efficient deceleration after effusing from the oven and for the initial capture in the trap. Furthermore, they possess the narrow intercombination line $\left|{}^1S_0\right\rangle \rightarrow \left|{}^3P_1\right\rangle$, which has a Doppler temperature low enough for the atoms to be transferred to an optical lattice. A clock running on the doubly-forbidden transition $\left|{}^1S_0\right\rangle \rightarrow \left|{}^3P_0\right\rangle$ of fermionic ^{87}Sr with natural linewidth of ~ 1 mHz [9] has recently demonstrated a fractional instability at the 10^{-17}-level after averaging for 10^3 s [10].

1.1.2 Local Oscillator

A requirement for interrogating a transition is that the carrier spectral density of the LO is narrow and stable enough to resolve the transition during the spectroscopy. In optical clocks this is typically accomplished by stabilizing the free-running clock laser to a high-finesse cavity by a Pound-Drever-Hall servo-lock (see appendix A), resulting in high bandwidth control and low short-term instability. Short-term in this context refers to fluctuations over periods < 100 s [11]. The cavity-reference is highly isolated from the external environment and vibration-induced length fluctuations are strongly suppressed by a proper design and mounting [12]. Despite this, any residual noise perturbing the reference degrades the oscillation stability since it is practically written onto the LO, making it difficult to take advantage of the high $Q \sim 10^{17}$ offered by optical clock transitions.

The fundamental limit to the instability at any time-scale for this passive setup is due to Brownian thermo-mechanical noise in the cavity mirrors, which leads to fluctuations in the optical length [13]. Current state-of-the-art cavities have been able to offer linewidths narrow enough to resolve the doubly-forbidden intercombination line of ^{87}Sr, limited by the Fourier limit of the pulse [13]. Recently, a linewidth below 40 mHz has been achieved by locking a free-running diode laser to an optical cavity based on a single silicon crystal [14].

Stabilizing an LO can also be achieved by locking it to an atomic transition[1] via spectroscopy, thereby circumventing the thermal noise floor of reference cavities. However, performing direct spectroscopy on ultranarrow sub-Hz optical transitions is extremely challenging, since the dipole is driven very weakly. As we will see, there are in theory ways to ease this task through cavity-enhanced nonlinear spectroscopy [15], which forms the basis of this thesis.

1.2 Thesis Outline

This thesis deals with a recently proposed scheme by the authors of [15], which theoretically allows direct spectroscopy on an ultranarrow optical transition through cavity-enhancement of the atomic optical depth. This will allow for stabilization against these atomic transitions, serving as an alternative to stabilization against a high-finesse optical cavity. In the current experiment the scheme is to be implemented using the intercombination line $\left|{}^1S_0\right\rangle \rightarrow \left|{}^3P_1\right\rangle$ of

[1] For an extended-cavity diode laser preliminary stabilization to a high-finesse cavity is neccessary in order to resolve linewidths at the Hz-level and below.

^{88}Sr, but given that the experiment is in its initial stage, this thesis merely deals with work that will enable implementing the proposed spectroscopy.

The thesis is organized as follows. Chapter 2 describes the theory behind cavity-enhanced nonlinear spectroscopy in detail and investigates what to anticipate when using ^{88}Sr. Issues regarding its implementation are also quantified and discussed. In chapter 3 a Zeeman slower for Sr is designed and built in order to deliver a sufficient flux of cold atoms for interrogation. The device is integrated in the vacuum system and its efficiency is measured. Concurrently, a semiclassical Monte Carlo simulation of the atomic deceleration in the slower is developed. Chapter 4 describes the magneto-optical trap for ^{88}Sr and investigates the atomic cloud lifetime both analytically and experimentally. In chapter 5 an alternative realization of an atomic beamline is investigated. More specifically, a beamline is suggested which is capable of producing a sufficient flux of cold atoms for continuous cavity-enhanced nonlinear spectroscopy. A semiclassical stochastic model is employed to investigate the beamline, and the obtained parameters are compared to those required. The thesis is concluded with an outline of future prospects.

Chapter 2

Cavity-Enhanced Spectroscopy

The purpose of this chapter is to introduce the concept of cavity-enhanced nonlinear spectroscopy. This in principle enables a novel stabilization scheme, where a laser is locked directly to an ultranarrow optical atomic transition, thereby circumventing the thermal noise floor present when referencing against a passive optical cavity. This spectroscopy is performed in a highly saturated limit, so we start by briefly reviewing the driven Jaynes-Cummings model with dissipation. Following the work by the authors of [15], this will allow us to investigate the dynamics associated with driving a coupled atom-cavity system with an arbitrary strength, from which the desired stabilization scheme follows. Concurrently, the results are also obtained in a purely classical framework. After applying the results to the intercombination line $\left|{}^1\mathrm{S}_0\right\rangle \rightarrow \left|{}^3\mathrm{P}_1\right\rangle$ of ${}^{88}\mathrm{Sr}$, considerations on the scheme and its implementation are presented.

In what follows the two-level atom is assumed to be in the Lamb-Dicke regime, where motional effects are suppressed such that only the internal atomic degrees of freedom are of interest.

2.1 Coherent Atom-Light Interaction

A system consisting of a single atom interacting with a single mode of an optical cavity is described in the Jaynes-Cummings model. The cavity mode is represented by a harmonic oscillator with an infinite number of equally spaced levels, and the two-level atom is compromised of a ground state $\left|g\right\rangle$ and an excited state $\left|e\right\rangle$ with transition linewidth Γ, separated in frequency by ω_a. We assume that all atomic decay processes are due to energy relaxation, i.e. the dipole dephasing rate T_2^{-1} is merely given by $\Gamma/2$, so there are no pure dephasing processes present in the system. The cavity-mode with linewidth κ has the resonant frequency ω_c. Given that the combined system is continuously driven by a coherent external laser with frequency ω_l, the Hamiltonian in a frame rotating at ω_l under the usual dipole-approximation and RWA reads [16]

$$\hat{H}_{\mathrm{JC}} = \hbar\Theta\hat{a}^\dagger\hat{a} + \hbar\Delta\hat{\sigma}_+\hat{\sigma}_- + i\hbar g(\mathbf{r})(\hat{a}^\dagger\hat{\sigma}_- - \hat{a}\hat{\sigma}_+), \tag{2.1}$$

where the laser-term has been neglegted for now. The detunings are relative the system constituents, i.e. $\Delta = \omega_a - \omega_l$ and $\Theta = \omega_c - \omega_l$. In what follows the laser linewidth Γ_{laser}, given by its inverse coherence time, is assumed vanishing. These definitions are summarized in figure 2.1.

The Pauli operators $\{\hat{\sigma}_z = \left|e\right\rangle\!\left\langle e\right| - \left|g\right\rangle\!\left\langle g\right|, \hat{\sigma}_+ = \left|e\right\rangle\!\left\langle g\right|, \hat{\sigma}_- = \hat{\sigma}_+^\dagger\}$ correspond to inversion, raising and lowering of the atomic state and obey the pseudo-spin algebra $[\hat{\sigma}_+, \hat{\sigma}_-] = \hat{\sigma}_z$ and $[\hat{\sigma}_z, \hat{\sigma}_\pm] = \pm 2\hat{\sigma}_\pm$. The creation and annihilation operators for photons in the mode of the cavity

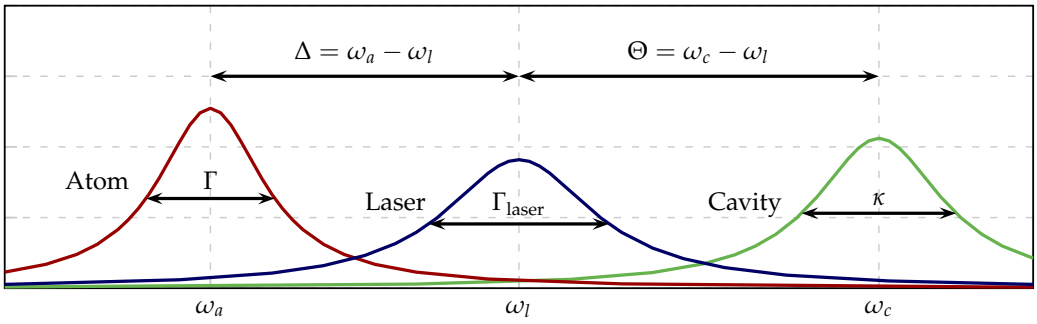

Figure 2.1: The Lorentzians associated with the atomic transition at ω_a and linewidth Γ (FWHM), external coherent laser with frequency ω_l and linewidth $\Gamma_{\text{laser}} \to 0$ and cavity mode with resonant frequency ω_c and linewidth κ. Also shown are the detunings (Δ, Θ) of the two system constituents, both defined relative the laser. Linewidths are not drawn to scale.

$(\hat{a}^\dagger, \hat{a})$ satisfy the bosonic commutator relation $[\hat{a}, \hat{a}^\dagger] = 1$ and $\hat{n} \equiv \hat{a}^\dagger \hat{a}$ is the intracavity photon number operator relative the vacuum.

The first two terms in (2.1) describe the cavity mode and atom, respectively. The dipole coupling $g(\mathbf{r})$ between the cavity mode and atom characterizes their coherent interaction. It depends on the standing wave structure of the resonator TEM_{00}-mode profile $\psi(\mathbf{r})$ with $1/e^2$-waist w_0 (radius) through $g(\mathbf{r}) = g_0 \psi(\mathbf{r})$, where [17]

$$g_0 = \sqrt{\frac{\omega_c}{2\hbar\varepsilon_0 V_{\text{eff}}}} \langle g | \hat{\mathbf{d}} | e \rangle. \tag{2.2}$$

Under the assumption that the Rayleigh length of the cavity mode is longer than the cavity length, the effective cavity mode volume reads

$$\begin{aligned} V_{\text{eff}} &= \int |\psi(\mathbf{r})|^2 dx dy dz && (2.3)\\ &= \int \left| \cos(2\pi z/\lambda) e^{-(x^2+y^2)/w_0^2} \right|^2 dx dy dz && (2.4)\\ &= \frac{1}{4} \pi w_0^2 L, && (2.5) \end{aligned}$$

where L is the cavity length and z denotes the axial cavity direction. This last term of (2.1) describes processes where an excitation of the cavity mode is annihilated (created) while exciting (de-exciting) the atom, thus forming the bare states $|g\rangle \otimes |n\rangle \equiv |g, n\rangle$ and $|e\rangle \otimes |n-1\rangle \equiv |e, n-1\rangle$. The dynamics is completely confined to this two-dimensional space of bare states for a fixed number of n cavity excitations.

The eigenstates can be found by diagonalization of (2.1), which in the case $\omega_c = \omega_a = \omega$ $(\Theta = \Delta)$ yields the system eigenstates [18]

$$|n, \pm\rangle = \frac{1}{\sqrt{2}} \left(|g, n\rangle \pm |e, n-1\rangle \right) \tag{2.6}$$

with eigenenergies $E_{n,\pm} = n\omega \pm g_0 \sqrt{n}$ for $n \in \mathbb{N}_0$. These are the well-known dressed states that constitute the Jaynes-Cummings ladder of doublets, and represent the equal distribution of excitation between atom and field. The coupling g_0 breaks the degeneracy of the uncoupled resonance, where the anharmonic level spacing increases with the square root of n as illustrated

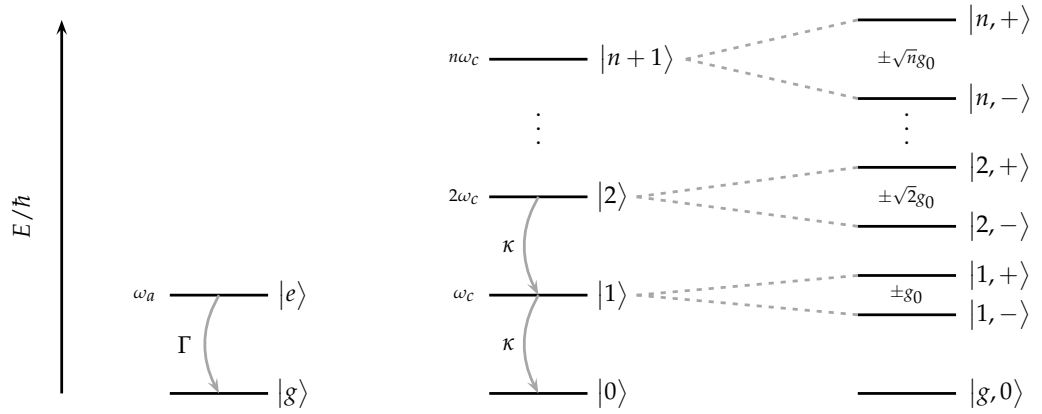

Figure 2.2: Left column: Energy spectrum for an unperturbed two-level atom. Middle column: Energy spectrum for an empty cavity with linewidth κ, represented by a harmonic oscillator with an infinite number of equally spaced modes. Right column: Energy spectrum for the coupled system, where the Lorentzian cavity transmission has split into two resonances. These states are the tensor products of the two former.

in figure 2.2. The resonances of the first doublet is separated by $2g_0$, known as vacuum Rabi splitting.

From the Schrödinger equation it follows that for a system initially prepared in $|e,0\rangle$, the inversion $\langle\hat{\sigma}_z\rangle$ oscillates between $|e,0\rangle$ and $|g,1\rangle$ with a maximum rate given by the single photon Rabi frequency $2g_0$, showing that the interaction of this closed system is highly coherent. This is similar to the dynamics displayed by the semiclassical Rabi model [18].

2.1.1 Dissipation

The model treated so far has assumed negligible dissipation, a most unphysical feature since signal transmission is required in order to extract information from the system. The dominant loss channel associated with the cavity is due exponential field decay through the mirrors. Since the intracavity electric field decays with rate κ, the intracavity number of photons decays with 2κ, specifying the quality factor Q of the cavity, $Q = \omega_c/2\kappa$ [19]. This does not add to the decoherence of the combined system, since the light can be reintroduced into the system again. In contrast, spontaneous emission into field modes different from the preferred cavity mode with rate Γ will add to the decoherence.

Fast coherent excitation exchange between atom and cavity mode reduces dissipative decay into free space, since the probability for a photon to escape the cavity is reduced. The strong coupling required to see the vacuum Rabi splitting in figure 2.2 is consequently quantified by the condition $g_0 \gg (\Gamma, \kappa)$. This requirement is also clear when recalling that the FWHM of the combined resonances must scale by $\sim(\kappa + \Gamma)$, effectively setting a lower limit on g_0 if the splitting is to be resolved. The coupling is then conveniently characterized by the cooperativity parameter $\mathcal{C}_0$, which for a system containing a single atom is defined as $\mathcal{C}_0 \equiv g_0^2/\kappa T_2^{-1}$.

Counteracting losses requires the inclusion of an external drive, and in the current setup the system will be externally excited by a laser entering through one of the cavity mirrors. Assuming perfect mode-matching and negligible mirror absorption, excitation of the cavity

mode by the laser is included by adding to (2.1) the term

$$\hat{H}_P = \hbar\eta(\hat{a}^\dagger + \hat{a}), \tag{2.7}$$

where η characterizes the strength. This term shifts the amplitude of the intracavity coherent state, which is verified in the following. Here the relation between η and the physical laser power P_{in} will also be established, which is necessary in order to predict the experimental outcome.

2.2 Maxwell-Bloch Equations

At this stage it is necessary to formally take into account the couplings (κ, Γ) to external modes of the thermal reservoir. The extension to this so-called open quantum system requires explicitly including the reservoir degrees of freedom, thus introducing the total density matrix operator $\hat{\varrho}$. The part pertaining only to the system $\hat{\varrho}_S$ is obtained by tracing over the reservoir degrees of freedom $\hat{\varrho}_S = \text{Tr}_R[\hat{\varrho}]$ under the usual Born-Markov approximation. The former states that the interaction between reservoir and system is sufficiently weak such that the reservoir is left unperturbed by the system. The Markov approximation assumes that the atom interacts with a structureless reservoir, equivalent to it being memoryless on the natural system timescale $1/(g_0, \kappa, \Gamma)$. This yields the system master equation given by [20]

$$\frac{\mathrm{d}\hat{\varrho}_S}{\mathrm{d}t} = -\frac{i}{\hbar}[\hat{H}_{\text{JC}}, \hat{\varrho}_S] + \kappa\hat{\mathcal{L}}_a\hat{\varrho}_S + \frac{\Gamma}{2}\hat{\mathcal{L}}_\sigma\hat{\varrho}_S \tag{2.8}$$

$$\equiv \hat{\mathcal{L}}\hat{\varrho}_S, \tag{2.9}$$

where the coherent evolution of the closed system is described by the commutator. The Liouvillians $(\hat{\mathcal{L}}_a, \hat{\mathcal{L}}_\sigma)$ are written in the usual Lindblad form

$$\hat{\mathcal{L}}_a\hat{\varrho}_S \equiv 2\hat{a}\hat{\varrho}_S\hat{a}^\dagger - \hat{a}^\dagger\hat{a}\hat{\varrho}_S - \hat{\varrho}_S\hat{a}^\dagger\hat{a} \tag{2.10}$$

$$\hat{\mathcal{L}}_\sigma\hat{\varrho}_S \equiv 2\hat{\sigma}_-\hat{\varrho}_S\hat{\sigma}_+ - \hat{\sigma}_+\hat{\sigma}_-\hat{\varrho}_S - \hat{\varrho}_S\hat{\sigma}_+\hat{\sigma}_- \tag{2.11}$$

and describe the dissipation of the system, namely the coupling of the cavity mode and atom to the reservoir, respectively. The master equation (2.9) can be used to find the temporal evolution of an arbitrary system operator expectation value $\langle\hat{O}\rangle$ through the general relation

$$\frac{d\langle\hat{O}\rangle}{dt} = \text{Tr}(\hat{O}\hat{\mathcal{L}}\hat{\varrho}_S). \tag{2.12}$$

This enables relating the drive strength η to its physical intracavity power P_{in}. This we do by first disregarding terms involving atomic operators in (2.1), since they serve no purpose for this specific calculation: The stationary stable state of this system is a coherent state, whose amplitude is shifted by the laser. We can then make the shift $\hat{a} = \bar{a} + \hat{p}$ in the Hamiltonian, where $\hat{p}^\dagger\hat{p}$ is the intracavity photon number operator relative to the new ground state amplitude $\bar{a}$. With this displacement the cavity-dissipation term (2.10) becomes

$$\kappa\hat{\mathcal{L}}_a\hat{\varrho}_S = \kappa\hat{\mathcal{L}}_p\hat{\varrho}_S + \frac{\kappa}{2}[(\bar{a}^*\hat{p} - \bar{a}\hat{p}^\dagger), \hat{\varrho}_S], \tag{2.13}$$

and with (2.8) in mind it is seen that the Hamiltonian gains the term $(\bar{a}^*\hat{p} - \bar{a}\hat{p}^\dagger)(i\hbar\kappa/2)$, since the last term in (2.13) has the form of a commutator. By choosing

$$\bar{a} = \frac{\hbar\eta}{-\Theta + i\hbar\kappa/2} \tag{2.14}$$

the drive η and all terms linear in $\hat{p}$ are eliminated in the Hamiltonian [21], which can be shown by straightforward substitution. Thus, we have diagonalized the Hamiltonian since it only contains the term $\hbar\Theta\hat{p}^\dagger\hat{p}$, where the new stable (with decay and drive included) coherent ground state has amplitude $\bar{a}$, which is related to η through (2.14). We are more interested in the intracavity photon number $\bar{n} = |\bar{a}|^2$, which in the abscence of a laser decays[1] as 2κ. In steady-state this decay is compensated by the laser such that $2\bar{n}\kappa = P_{\text{in}}/\hbar\omega_l$, so when the laser is resonant with the cavity ($\Theta = 0$) the two quantities are thus related by

$$\eta = \sqrt{\frac{\kappa P_{\text{in}}}{2\hbar\omega_l}} = \sqrt{\frac{\kappa\Phi_{\text{in}}}{2}}, \tag{2.15}$$

where Φ_{in} is the incoupled photon flux.

Now η has been calibrated, so we are in a position to realistically investigate the system under the influence of a laser. Utilizing the commutator relations, the cyclic properties of the trace and taking advantage of the fact that we work in a basis where $\hat{\sigma}_z\hat{\sigma}_\pm = \pm\hat{\sigma}_\pm$ it is straightforward to derive the Maxwell-Bloch equations using (2.12)

$$\frac{d\langle\hat{a}\rangle}{dt} = -(\kappa + i\Theta)\langle\hat{a}\rangle + g_0\langle\hat{\sigma}_-\rangle + \eta \tag{2.16}$$

$$\frac{d\langle\hat{\sigma}_-\rangle}{dt} = -(T_2^{-1} + i\Delta)\langle\hat{\sigma}_-\rangle + g_0\langle\hat{a}\hat{\sigma}_z\rangle \tag{2.17}$$

$$\frac{d\langle\hat{\sigma}_z\rangle}{dt} = -\Gamma(\langle\hat{\sigma}_z\rangle + 1) - 2g_0(\langle\hat{a}^\dagger\hat{\sigma}_-\rangle + \langle\hat{\sigma}_+\hat{a}\rangle), \tag{2.18}$$

which describe the dynamics of the system. An analytical solution to the set (2.16)-(2.18) is not possible, since it is not closed. Nonetheless, the set reveals the consequences of the coupling g_0 on the combined dynamics: The atomic radiation adds to the intracavity field through the term $g_0\langle\sigma_-\rangle$ in (2.16) in addition to the cavity field driving the atomic transition through $g_0\langle\hat{a}\hat{\sigma}_z\rangle$ in (2.17). The expected atomic behavior is obtained for $g_0 \to 0$ in (2.18), since the inversion $\langle\hat{\sigma}_z\rangle$ then decays.

The expansion to N noninteracting atoms is readily carried out by generalizing the master equation according to the new Hamiltonian

$$\hat{H}_{\text{JC}} = \hbar\Theta\hat{a}^\dagger\hat{a} + \sum_{j=1}^{N}\hbar\Delta\hat{\sigma}_{j,+}\hat{\sigma}_{j,-} + \sum_{j=1}^{N} i\hbar g_j(\mathbf{r})(\hat{a}^\dagger\hat{\sigma}_{j,-} - \hat{a}\hat{\sigma}_{j,+}) + \hbar\eta(\hat{a}^\dagger + \hat{a}) \tag{2.19}$$

$$\hat{\mathcal{L}}_\sigma\hat{\varrho}_S \equiv \sum_{j=1}^{N}\left(2\hat{\sigma}_{j,-}\hat{\varrho}_S\hat{\sigma}_{j,+} - \hat{\sigma}_{j,+}\hat{\sigma}_{j,-}\hat{\varrho}_S - \hat{\varrho}_S\hat{\sigma}_{j,+}\hat{\sigma}_{j,-}\right). \tag{2.20}$$

The semiclassical limit is obtained when both $N \to \infty$ and the cavity field is very large. Here adding/removing an atom leaves the system largely unchanged, due to which each atom contributes only weakly to the overall coupling. Consequently, $\mathcal{C}_0 \to 0$ and $\mathcal{C}_0 N \to$ const, and in this limit the two subsystems are approximately uncorrelated, allowing for the compound expectation values in the equations of motion to be factorized, $\langle\hat{a}^\dagger\hat{\sigma}_{j,-}\rangle \approx \langle\hat{a}^\dagger\rangle\langle\hat{\sigma}_{j,-}\rangle$. Utilizing this assumption yields the closed set of multi-atom Maxwell-Bloch equations ($o \equiv \langle\hat{o}\rangle$) given

[1] Taking $g_0 \to 0$ in the total Hamiltonian (2.1) and utilizing the cyclic properties of the trace operator, one readily finds that $d\langle\hat{a}^\dagger\hat{a}\rangle/dt = -2\kappa\langle\hat{a}^\dagger\hat{a}\rangle$.

by [15–17]

$$\frac{da}{dt} = -(\kappa + i\Theta)a + g_0 N\sigma_{j,-} + \eta \tag{2.21}$$

$$\frac{d\sigma_{j,-}}{dt} = -(T_2^{-1} + i\Delta)\sigma_{j,-} + g_0 a\sigma_{j,z} \tag{2.22}$$

$$\frac{d\sigma_{j,z}}{dt} = -\Gamma(\sigma_{j,z} + 1) - 2g_0(a^\dagger\sigma_{j,-} + \sigma_{j,-}a^\dagger). \tag{2.23}$$

Note that it has been assumed that g_j is constant for all atoms, resulting in considerable simplification since we can ignore the spatial features of $\psi(\mathbf{r})$. This is valid when the atom cloud size is much smaller than the probe laser field and the cavity is in a running-wave configuration. Introducing the collective pseudospin operators

$$\hat{\sigma}_- = \sum_{j=1}^{N} \hat{\sigma}_{j,-} \quad \text{and} \quad \hat{\sigma}_z = \sum_{j=1}^{N} \hat{\sigma}_{j,z} \tag{2.24}$$

allows casting the Maxwell-Bloch equations into the form

$$\frac{da}{dt} = -(\kappa + i\Theta)a + g_0\sigma_- + \eta \tag{2.25}$$

$$\frac{d\sigma_-}{dt} = -(T_2^{-1} + i\Delta)\sigma_- + g_0 a\sigma_z \tag{2.26}$$

$$\frac{d\sigma_z}{dt} = -\Gamma(\sigma_z + N) - 2g_0(a^\dagger\sigma_- + \sigma_+ a). \tag{2.27}$$

These equations form the starting point for a numerical analysis of the system dynamics in different domains.

2.2.1 Vacuum Rabi Splitting

As was illustrated in figure 2.2, a weakly driven single atom strongly coupled to a cavity mode displays splitting of the Lorentzian resonance into two equal-amplitude dressed states $|1, \pm\rangle$. The cavity resonance will emerge again with increasing atom-cavity detuning, since the coupling is decreased. The weak-drive limit is formally quantified in the following section, but until then it (vaguely) denotes drive strengths η, where the splitting occurs.

To a good approximation vacuum Rabi splitting scales as 2Σ in multi-atom systems, where $\Sigma \equiv g_0\sqrt{N}$ is the collective coupling [17, 22, 23]. Figure 2.3 shows the steady-state intracavity photon number $|a|^2$, obtained by numerically solving (2.25)-(2.27) for three different relative detunings. The resonances form an avoided crossing with the anticipated distance 2Σ occuring for zero atom-cavity detuning $\omega_a = \omega_c$ ($\Theta = \Delta$). In addition to reducing the coupling, increasing the atom-cavity detuning will also affect the resonance amplitudes, since the two decoupled constituents have different transmissions. The parameters used here are $(\kappa, \Gamma) = 2g_0(1, 1)$. With $N = 4 \cdot 10^2$ atoms we are well within the strong coupling limit $\Sigma > (\kappa, \Gamma)$, which corresponds to the collective cooperativity $\mathcal{C} = N\mathcal{C}_0 = 200 \gg 1$. These parameters will also be used in the following, unless otherwise stated.

These systems have also been realized physically. As an example the system treated in [23] is in the limit $(g_0, \kappa, \Gamma)/2\pi = (0.12, 0.8, 2.6)$ MHz such that each atom-cavity interaction is governed by incoherent free-space decay. However, the presense of $N \simeq 10^5$ atoms increases $\mathcal{C}$ to the degree $\mathcal{C} \gg 1$ that the Rabi splitting survives the dissipation, rendering it possible to explicitly verify the linear dependence of $g_0\sqrt{N}$ on $\sqrt{N}$.

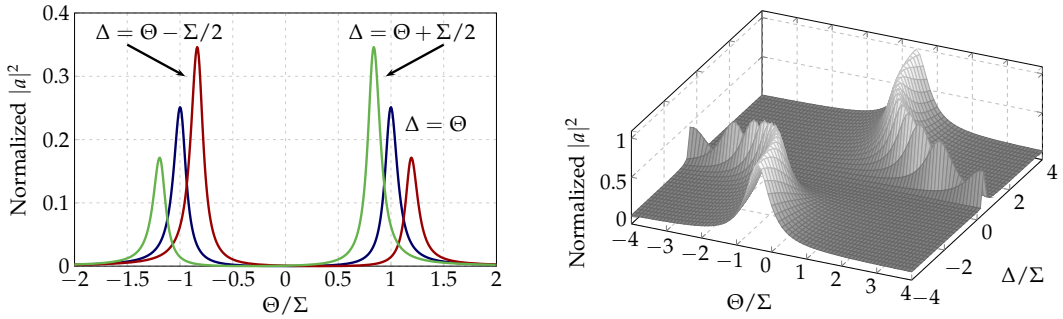

Figure 2.3: Left: The Rabi splitting for various relations between the detunings $\Delta = \omega_a - \omega_l$ and $\Theta = \omega_c - \omega_l$ in a system with $N = 4 \cdot 10^2$ atoms and $(\kappa, \Gamma) = 2g_0(1, 1)$. Right: The general case for arbitrary detunings, normalized to the maximal value attained on the interval. The case $\Delta = \Theta$ in the left figure corresponds to the diagonal.

Vacuum Rabi splitting can be explained classically, since (2.8) reduces to the master equation for two coupled harmonic oscillators in the weak-drive limit [17]. This is reasonable since the cavity mode in the quantum picture by itself is a quantized harmonic oscillator, and for weak drives the atom mimics a harmonic oscillator. The two observed resonances in figure 2.3 are thus similar to those obtained from this classical treatment, due to which their splitting is also dubbed normal mode splitting (NMS).

An alternative way to derive this behavior in an entirely classical setting is by treating the stationary atom as a classical dipole, where it merely acts as to coherently scatter the continuously incoming narrowband radiation, represented by a Gaussian TEM_{00} mode. The steady-state intracavity amplitude in this framework is determined by the resonance condition that the combined field originating from the laser, cavity and dipoles after an integer number of round trips is unchanged. In the RWA this leads to the following normalized transmitted power P_T [24]

$$P_T = \frac{1}{[1 + \mathcal{C}\mathcal{A}(\Delta)]^2 + [2\Theta/\kappa + \mathcal{C}\mathcal{D}(\Delta)]^2}, \tag{2.28}$$

where $\mathcal{A}(\Delta)$ and $\mathcal{D}(\Delta)$ designate the atomic Lorentzian absorptive and dispersive response to the applied field for a weak drive,

$$\mathcal{A}(\Delta) = +\frac{\Gamma^2}{\Gamma^2 + 4\Delta^2} \tag{2.29}$$

$$\mathcal{D}(\Delta) = -\frac{2\Delta\Gamma}{\Gamma^2 + 4\Delta^2}, \tag{2.30}$$

which are related to each other through the usual Kramers-Kronig relations. This solution is shown in figure 2.4 for the case $\Theta = 0$ alongside the solution originating from solving (2.25)-(2.27). The expected behavior is observed, c.f. figure 2.3 (right), where the intracavity power goes to zero at exact resonance due to the avoided crossing.

As seen in (2.28), the atomic absorption decreases P_T, whereas the dispersion acts as to displace the cavity resonance. A classical explanation of NMS is thus readily apparent in this picture: For strong coupling $\mathcal{C} \gg 1$, the atomic absorption heavily degrades the cavity finesse around resonance. However, the phase shift due to the atomic medium compensates the phase mismatch between cavity and intracavity light when the laser is detuned by the right amount,

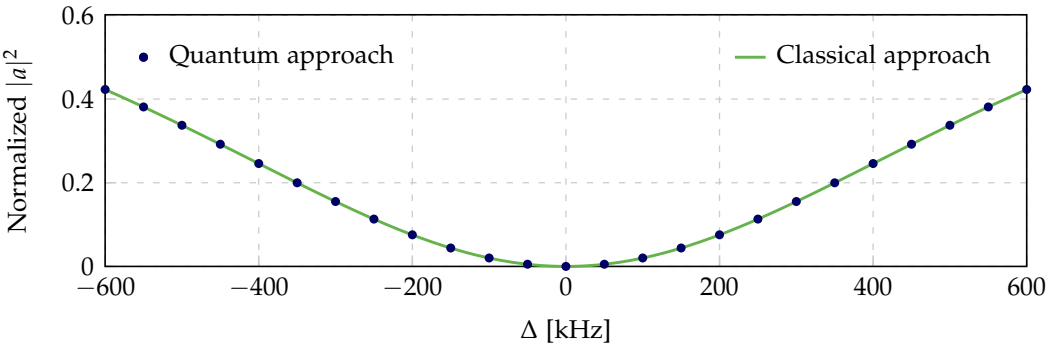

Figure 2.4: The normalized intracavity photons given $\omega_l = \omega_c$ ($\Theta = 0$) for a system with $N = 5 \cdot 10^6$ atoms, $\kappa/2\pi = 2.5\,\text{MHz}$, $\Gamma/2\pi = 7.6\,\text{kHz}$ and $P_{\text{in}} = 30\,\text{nW}$, corresponding to $g_0\sqrt{N}/2\pi = 8.3\,\text{MHz}$.

resulting in constructive interference and thus an enchanced P_T at these points. Due to (2.30) being odd, there are two such peaks symmetric with respect to $\Delta = 0$.

2.2.2 Optical Bistability

We will now go beyond the limit of a weak drive, and the analysis will follow the same lines as in [15, 17]. The analytical steady-state solution to (2.25)-(2.27) for a system with $\Theta = 0$ ($\omega_c = \omega_l$) is given by

$$\sigma_- = \frac{g_0}{\Gamma/2 + i\Delta} a\sigma_z \tag{2.31}$$

$$\sigma_z = -\frac{N}{1 + (|a|^2/n_0)/(1 + 4(\Delta/\Gamma)^2)} \tag{2.32}$$

$$|a|^2 = \frac{\eta^2}{\kappa^2} \frac{1 + 4(\Delta/\Gamma)^2}{(1 - \mathcal{C}_0\sigma_z)^2 + 4(\Delta/\Gamma)^2}, \tag{2.33}$$

where $n_0 \equiv \Gamma T_2^{-1}/(4g_0^2) \propto \Gamma/\lambda^3$ is denoted the saturation photon number. As seen later, in the framework established by these equations it is natural to define the incoupled intensity as $I_{\text{in}} \equiv \eta^2/(n_0\kappa^2)$, which is also a physically reasonable definition. Relating I_{in} to P_{in} is done by (2.15).

The behavior of $|a|^2$ with I_{in} is illustrated in figure 2.5, showing that three different domains exist: The first domain is quantified by $I_{\text{in}} < 4\mathcal{C} = 800$ and is that of a weak drive, which has been treated so far: In the dispersive limit $\Delta \gg \Gamma$ the atom-cavity interaction is very weak, resulting only in a minor reduction in intracavity intensity. For $\Delta \sim 0$ the drive is far detuned from the normal modes and the decrease in $|a|^2$ is from (2.33) seen to be $\sim \mathcal{C}^2 = 4 \cdot 10^4$ compared to the saturated case $\sigma_z \to 0$. With figure 2.3 in mind, this is the expected behavior.

New behavior emerges for $4\mathcal{C} = 800 < I_{\text{in}} < \mathcal{C}^2/4 = 10^4$, where three real distinct values for $|a|^2$ exist out of which one is unstable, a signature of absorptive optical bistability [16, 17]. The dots in figure 2.5 show such a solution for the case $\Delta = 15\Gamma$: The rightmost arrow indicates the increase in intracavity photons that occurs when adiabatically scanning from low to high I_{in} across the bifurcation point. The leftmost arrow indicates the decrease in intracavity photons occuring when tracing back again, similar to hysteric behavior. The unstable solution thus constitutes a separator. For the strongly saturated case $I_{\text{in}} > \mathcal{C}^2/4 = 10^4$ the atoms leave the transmission practically unaltered, since the atomic transition is maximally driven and consequently transparent, in which case a unique solution appears again.

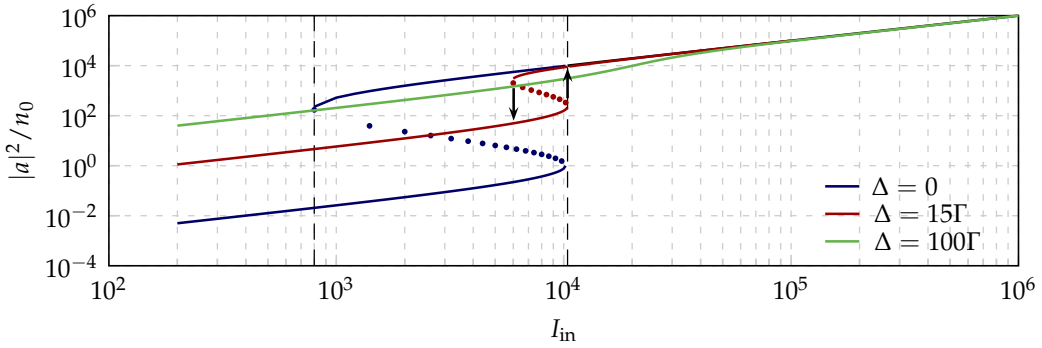

Figure 2.5: Semiclassical calculation (2.33) of the intracavity steady-state intensity as a function of incoupled intensity for different detunings $\Delta = \omega_a - \omega_l$ given $\Theta = 0$. Vertical dashed lines indicate the threshold for bistability.

Figure 2.6 illustrates the corresponding behavior of the NMS. The normal modes bend towards each other to form a closed structure when going beyond $4\mathcal{C} = 800$, showing that the atoms no longer act in a coherent fashion with the cavity, since they are becoming saturated. As expected, the Rabi peaks have formed a singlet structure at large saturations $I_{\text{in}} > 10^4$ resembling that of an empty cavity.

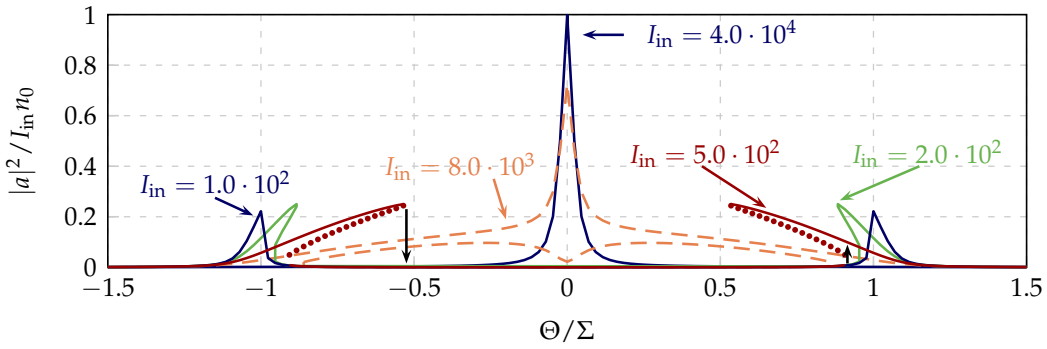

Figure 2.6: Evolution of the two vacuum Rabi peaks as a function of $\Theta = \Delta$ for various the incoupled intensities. For small incouplings $I_{\text{in}} \lesssim 10^2$ the normal modes are recovered.

The spectra along $\Theta = 0$ ($\omega_c = \omega_l$) corroborate our observations for low-to-medium saturation $I_{\text{in}} = \{0.5 \cdot 10^3, 8.0 \cdot 10^3\}$, as seen in figure 2.7 (left). However, for $I_{\text{in}} > 10^4 = \mathcal{C}^2/4$ a peak emerges around resonance. The origin of the peak is visible in figure 2.7 (right), where it is seen to emerge due to a kink around the combined resonance $(\Theta, \Delta) \approx 0$. It occurs as the system modes approach the cavity resonance and it vanishes again for $I_{\text{in}} \gg \mathcal{C}^2/4$, since the atoms are completely transparent to the cavity field in this limit. Beyond this limit only the cavity resonance remains, where $|a|^2/I_{\text{in}}n_0 \to 1$ for all $\Delta = \omega_a - \omega_l$.

Since the transmission is determined by the intracavity field, the cavity output is also increased drastically around $\Delta \sim 0$. At first glance, this peak is not unusual in that its FWHM is much greater than Γ, which increases further with incoupled power due to power broadening. As we will see, however, the presence of the cavity makes this resonance highly desirable from a metrological point of view in that it theoretically enables a novel laser stabilization scheme relevant for ultranarrow transitions. This is explored further in the following section, but first we must conclude the current section on the Maxwell-Bloch equations. It is in order to do

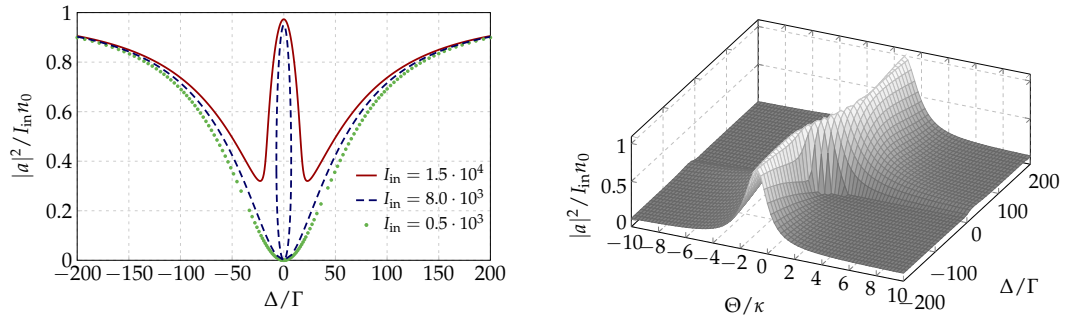

Figure 2.7: Left: Normalized intracavity intensity as a function of the incident laser detuning $\Delta = \omega_a - \omega_l$ for various incoupled intensities and $\Theta = 0$. Right: The normalized intracavity intensity as a function of both detunings for a large intensity, $I_{\text{in}} = 1.5 \cdot 10^4$.

so by showing that the behavior for $I_{\text{in}} > 4\mathcal{C}$ described so far can also be obtained from the classical model (2.28).

2.2.3 Classical Approach to Optical Bistability

It is possible to obtain the medium-to-high saturation phenomena optical bistability in a completely classically framework. This requires extending the model introduced in [24] by generalizing the atomic susceptibilities (2.29)-(2.30) to arbitrary intensities. Since the backaction of the atoms onto the cavity field has already been included in the original derivation of (2.28), the generalization only needs to invoke the optical Bloch equations.

We start by looking at the induced polarization $\mathbf{P}$ in the ensemble of N two-level atoms. Denoting their volume by V, it is readily found by considering them as a dielectric such that

$$\mathbf{P} = \Re\left[\varepsilon_0 \chi(\Delta)\mathbf{E}_0 e^{-i\omega_l t}\right] \tag{2.34}$$

$$= \varepsilon_0 \mathbf{E}_0[\chi'(\Delta)\cos(\omega_l t) + \chi''(\Delta)\sin(\omega_l t)], \tag{2.35}$$

where $\mathbf{E}_0$ denotes the intracavity drive amplitude and $\chi = \chi' + i\chi''$ the ensemble susceptibility. Since the medium is assumed isotropic $\mathbf{P}$ is parallel to $\mathbf{E}_0$ and the tensor nature of χ can be neglegted. Additionally, the medium has been assumed to adiabatically follow the applied laser. The induced dipole moment per volume is also given by $\mathbf{P} = (N/V)\langle\hat{\mathbf{d}}\rangle$, where the single-atom dipole operator is $\hat{\mathbf{d}} = \mathbf{d}_0(\hat{\sigma}_+ + \hat{\sigma}_-)$, purely off-diagonal in the atomic eigenbasis due to parity. The expectation value $\langle\hat{\mathbf{d}}\rangle$ is thus given by [25]

$$\langle\hat{\mathbf{d}}\rangle = \mathrm{Tr}\,(\hat{\varrho}\hat{\mathbf{d}}) \tag{2.36}$$

$$= \mathbf{d}_0(\varrho_{ge}e^{i\omega_l t} + \varrho_{eg}e^{-i\omega_l t}) \tag{2.37}$$

$$= 2\mathbf{d}_0[u\cos(\omega_l t) - v\sin(\omega_l t)], \tag{2.38}$$

where $(u, v, w)^T$ defines the Bloch vector for the two-level atom

$$u = \frac{1}{2}(\varrho_{ge} + \varrho_{eg}) \tag{2.39}$$

$$v = \frac{1}{2i}(\varrho_{ge} - \varrho_{eg}) \tag{2.40}$$

$$w = \frac{1}{2}(\varrho_{ee} - \varrho_{gg}), \tag{2.41}$$

and $\hat{\varrho}$ in this context is the density matrix for a single atom. The steady-state solutions for u and v are [25]

$$u_{t\to\infty} = \frac{\Omega}{2}\frac{\Delta}{\Delta^2 + \Gamma^2/4 + \Omega^2/2} \tag{2.42}$$

$$v_{t\to\infty} = \frac{\Omega}{2}\frac{\Gamma/2}{\Delta^2 + \Gamma^2/4 + \Omega^2/2}, \tag{2.43}$$

where the Rabi frequency $\hbar\Omega \equiv -\mathbf{d}_0 \cdot \mathbf{e}E_0$ has been introduced through the interaction energy. In the adiabatic approximation these solutions can be utilized in (2.38) which, by comparing to (2.35), yields the general expressions for the atomic absorptive and dispersive response

$$\mathcal{A}(\Delta) = +\frac{1}{4}\frac{\Gamma^2}{\Delta^2 + \Gamma^2/4 + \Omega^2/2} \tag{2.44}$$

$$\mathcal{D}(\Delta) = -\frac{1}{2}\frac{\Delta\Gamma}{\Delta^2 + \Gamma^2/4 + \Omega^2/2}. \tag{2.45}$$

These expressions reduce to (2.29)-(2.30) in the limit $\Omega \to 0$ as required. The Ω^2-term in the denominators turns (2.28) into an implicit equation for P_T, which we readily solve numerically. All that remains now is to relate Ω to P_T, which follows from the intracavity intensity I, $\Omega = \Gamma\sqrt{I/2I_{\text{sat}}}$, and the transmission coefficient T is determined by the cavity finesse $\mathcal{F} = \pi\sqrt{1-T}/T$. As illustrated in figure 2.8, this classical approach almost yields the same signal above bistability as the fully quantum mechanical approach, which has a certain novelty to it. In addition it also reproduces bistability. A classical explanation of the peak is that away from atomic resonance the phase shift imparted on the cavity field by the atoms prevents the intracavity field from building up [15].

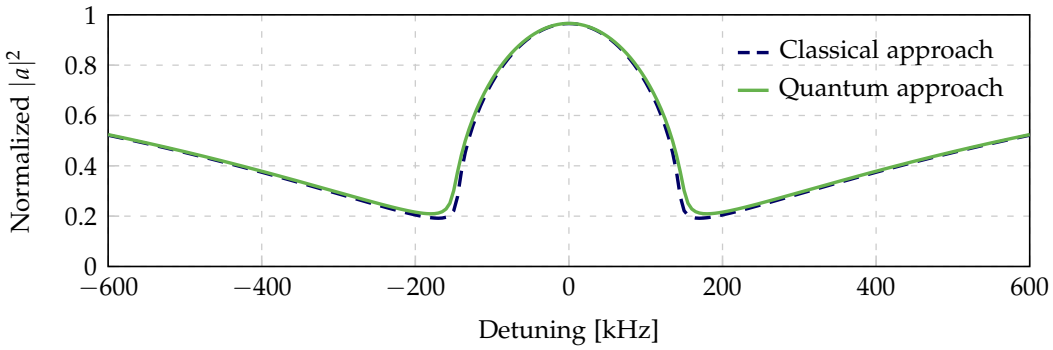

Figure 2.8: The normalized intracavity photons derived in a quantum mechanical and classical framework given $\omega_l = \omega_c$ ($\Theta = 0$), $N = 5 \cdot 10^6$ atoms, $\kappa/2\pi = 2.5\,\text{MHz}$, $\Gamma/2\pi = 7.6\,\text{kHz}$ and $P_{\text{in}} = 9\,\mu\text{W}$. The saturation parameter $I/I_{\text{sat}} = 180$, corresponding to $I_{\text{in}} = 24 \cdot 10^3 > \mathcal{C}^2/4 \simeq 8 \cdot 10^3$.

2.3 Lock Performance

Having introduced the theory, we are now ready to apply the presented results to the inter-combination line $|{}^1\text{S}_0\rangle \to |{}^3\text{P}_1\rangle$ of ^{88}Sr. We start by considering a realistic low-quality cavity 30 cm long with finesse $\mathcal{F} = 120$ ($\kappa/2\pi = 4.2\,\text{MHz}$), containing $N = 5 \cdot 10^6$ atoms. Given that the external coherent laser with waist 0.5 mm probes the transition $|{}^1\text{S}_0\rangle \to |{}^3\text{P}_1\rangle$ (689 nm, $\Gamma/2\pi = 7.6\,\text{kHz}$) of ^{88}Sr, the collective cooperativity is $\mathcal{C} = 110 \gg 1$ such that strong coupling

is present. Utilizing the relation in (2.14) yields that the limit $\mathcal{C}^2/4$ corresponds to the incoupled power $P_{\text{in}} \simeq 2\,\mu\text{W}$. The spectrum for $P_{\text{in}} = 2.5\,\mu\text{W}$ is shown in figure 2.9 (left), displaying a FWHM of 145 kHz. These are realistic parameters so they will be utilized in the following. Going below this N requires a much smaller P_{in}, which is not feasible.

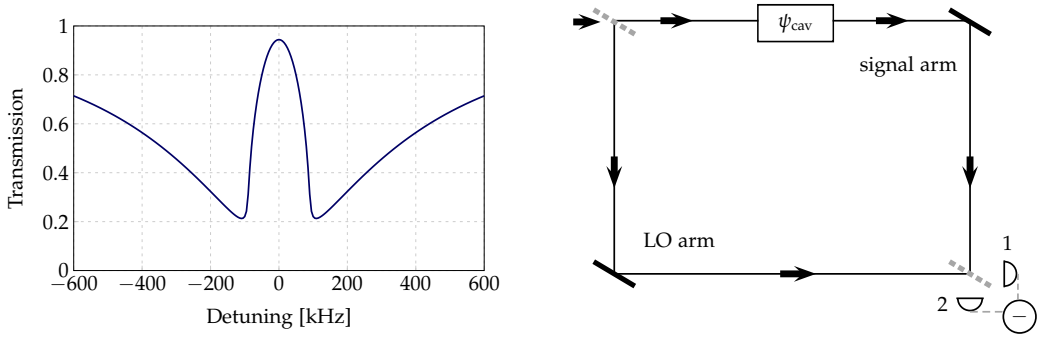

Figure 2.9: Left: The transmission of cavity-enhanced nonlinear spectroscopy on the $\left|{}^1\text{S}_0\right\rangle \rightarrow \left|{}^3\text{P}_1\right\rangle$ of ^{88}Sr. Right: A Mach-Zehnder interferometer, which can be utilized to stabilize a laser to the nonlinear transmission peak, where ψ_{cav} denotes the phase acquired by the light due to interaction with the confined atoms when travelling along the signal arm. Dashed grey lines denote beam-splitters, solid black lines mirrors.

In order to see the practical relevance of the cavity-enhanced peak, we will now investigate the possibility of locking a laser to it following the approach by the authors of [15]. The framework is set by the standard Mach-Zehnder interferometer illustrated in figure 2.9: The laser to be stabilized is incident on a beam splitter (upper left corner), which splits up its power to the signal arm and the local oscillator (LO) arm, both designated in the figure. The cavity containing the atoms is placed in the signal arm, represented by a phase shift ψ_{cav}. It is in order to note that the necessary condition $\Theta = 0$ ($\omega_c = \omega_l$) translates into the cavity being locked to the laser, which can be accomplished by a Pound-Drever-Hall lock (appendix A). The signals from the two arms are recombined by a second beam splitter after which the signals are collected by two photodetectors, whose photocurrents are subtracted. The phase acquired in the signal (LO) arm is denoted ψ_{sig} (ψ_{LO}), where ψ_{sig} consists of a term originating from the cavity ψ_{cav} and from the optical path of the arm ψ_l.

The generated photocurrents will contain the usual two constant terms originating from the direct intensity detection in addition to the heterodyne mixing term, which depends on the total phase difference between the two arms. For the two detectors the photocurrents $i_{1,2}$ are thus given by

$$i_{1,2} = \frac{e\eta_{\text{qe}}}{h\nu}\left(\frac{P_{\text{sig}}}{2} + \frac{P_{\text{LO}}}{2} \pm \sqrt{P_{\text{sig}}P_{\text{LO}}}\cos(\psi_{\text{sig}} - \psi_{\text{LO}})\right) + \delta i_{1,2}(t), \tag{2.46}$$

where P_{sig} (P_{LO}) denotes the power in the signal (LO) pathway, η_{qe} the detector quantum efficiency, $\delta i_{1,2}$ the photocurrent shot-noise at the respective detector and ν the laser frequency. Choosing the relative arm lengths such that $\psi_{\text{LO}} - \psi_l \simeq (2n\pi + \pi/2)$, $n \in \mathbb{Z}$, and assuming

that the laser is close to the atomic resonance, $\psi_{\text{cav}} \ll 1$,

$$i_{\text{diff}} \equiv i_1 - i_2 \simeq \frac{2e\eta_{\text{qe}}}{h\nu}\sqrt{P_{\text{sig}}P_{\text{LO}}}\psi_{\text{cav}} + \delta i(t) \tag{2.47}$$

$$\simeq \frac{2e\eta_{\text{qe}}}{h\nu}\sqrt{P_{\text{sig}}P_{\text{LO}}}\frac{d\psi_{\text{cav}}}{d\nu}\Delta\nu + \delta i(t) \tag{2.48}$$

for $\delta i(t) \equiv \delta i_1(t) - \delta i_2(t)$ and $\psi_{\text{cav}} \simeq (d\psi_{\text{cav}}/d\nu)\Delta\nu$, where $\Delta\nu$ is the detuning from the combined resonance. The assumption of a linear phase shift around resonance is well justified, since we are basically probing an atomic transition close to resonance. This expression for i_{diff} constitutes the error signal provided by the interferometer. An expression for ψ_{cav} can be found by first casting (2.31)-(2.33) into dimensionless form [16, 17]

$$y = x\left(1 + \mathcal{C}\frac{1 - iT_2\Delta}{1 + |x|^2 + (T_2\Delta)^2}\right), \tag{2.49}$$

where $y = \eta/(\kappa\sqrt{n_0}) = \sqrt{I_{\text{in}}}$ determines the normalized incoupled intensity and $x = a/\sqrt{n_0}$ the normalized intracavity buildup. It is clear from (2.33) that $|x|^2 \to I_{\text{in}}$ in the saturated limit $\beta \equiv 4I_{\text{in}}/\mathcal{C}^2 > 1$, which is expected since the transition is bleached. If $\mathcal{C} \gg T_2\Delta$ as well, (2.49) is to first order given by

$$y \simeq x\left(1 + \frac{4}{\mathcal{C}\beta}[1 - iT_2\Delta]\right). \tag{2.50}$$

The phase of the transmitted light relative the incoming light is given by $\psi_{\text{cav}} = \arg(x/y) = \arctan[\Im(x/y)/\Re(x/y)]$,

$$\psi_{\text{cav}} \simeq \frac{4T_2}{\mathcal{C}\beta}\Delta, \tag{2.51}$$

thus concluding the expression for the error signal. It is worth noting that power broadening of the transmission peak is taken into account by β.

The ultimate performance provided by this error signal can be evaluated by finding the quantum-limited linewidth provided by the lock. Since the noise process perturbing the system is random, the autocorrelation function for the shot-noise photocurrent is given by

$$\langle \delta i(t)\delta i(t+\tau)\rangle = \frac{e^2\eta_{\text{qe}}}{h\nu}(P_{\text{sig}} + P_{\text{LO}})\delta(\tau) \tag{2.52}$$

$$\simeq \frac{e^2\eta_{\text{qe}}}{h\nu}P_{\text{LO}}\delta(\tau), \tag{2.53}$$

for $P_{\text{sig}} \lesssim P_{\text{LO}}$, where the prefactor in (2.52) is set by the shot-noise level which depends on the rate of photons hitting the detector converted into photocurrent. During locked operation the feedback control loop forces the DC difference current i_{diff} to zero. However, the residual frequency error $\Delta\nu_{\text{err}}$ due to $\delta i(t)$ is readily found via the conversion factor established by (2.48)

$$\Delta\nu_{\text{err}}(t) = \frac{h\nu}{2e\eta_{\text{qe}}\sqrt{P_{\text{sig}}P_{\text{LO}}}(d\psi_{\text{cav}}/d\nu)}\delta i(t) \tag{2.54}$$

with autocorrelation function

$$\langle \Delta\nu_{\text{err}}(t)\Delta\nu_{\text{err}}(t+\tau)\rangle = \frac{h\nu}{4\eta_{\text{qe}}P_{\text{sig}}(d\psi_{\text{cav}}/d\nu)^2}\delta(\tau). \tag{2.55}$$

Utilizing the Wiener–Khinchin theorem, relating the power spectral density (PSD) of a stationary random process to the corresponding time-domain autocorrelation function, yields the two-sided photocurrent noise PSD corresponding to (2.55)

$$S_{\Delta\nu_{\mathrm{err}}}(f) = \int_{-\infty}^{\infty} \langle \Delta\nu_{\mathrm{err}}(t)\Delta\nu_{\mathrm{err}}(t+\tau)\rangle\, e^{-i2\pi f\tau}\, d\tau \tag{2.56}$$

$$= \frac{h\nu}{4\eta_{\mathrm{qe}}P_{\mathrm{sig}}(d\psi_{\mathrm{cav}}/d\nu)^2}, \tag{2.57}$$

constant for all Fourier frequencies, since the noise process is white. Consequently, the FWHM of the PSD in the carrier-frequency domain is given by $2\pi S_{\Delta\nu_{\mathrm{err}}}(f)$ for all time scales [7]. All that remains is thus to find P_{sig}, which in steady-state satisfies the relation $P_{\mathrm{sig}}/h\nu = 2\kappa|a|^2 = \kappa\mathcal{C}^2 n_0\beta/2$. Inserting the parameters used in figure 2.9 (left), the shot-noise limited linewidth of a laser locked to this resonance is given by

$$\Delta\nu_{\mathrm{FWHM}} = \frac{\mathcal{C}_0}{16\pi\eta_{\mathrm{qe}}\Gamma T_2^2}\beta \tag{2.58}$$

$$\simeq 5.5\,\mathrm{mHz} \tag{2.59}$$

for $\eta_{\mathrm{qe}} = 1$, $\beta = 1.3$ and $\Gamma/2 = T_2^{-1}$, which is below the sub-40 mHz linewidth recently attained in [14]. This is an absolute lower limit since the atomic lifetime has been assumed infinite and their motion has been completely disregarded, but it gives an idea of the performance potentially provided by this nonlinear phenomena. Such a light source could readily be employed as LO in an optical atomic clock due to its long coherence time.

We are now in a position to see why this locking scheme is useful. Placing a cavity around an ensemble of atoms will augment their optical depth, since the average number of photon round trips in a cavity of finesse $\mathcal{F}$ is $\mathcal{F}/\pi$. As a consequence the absorption profile is considerably broadened in the linear regime $I \ll I_{\mathrm{sat}}$, which we have showed both quantum mechanically and classically, c.f. figure 2.4.

Direct spectroscopy on an ultranarrow sub-Hz transition is extremely challenging, since the dipole is driven very weakly. As an example the clock transition $\left|{}^1\mathrm{S}_0\right\rangle \rightarrow \left|{}^3\mathrm{P}_0\right\rangle$ of ^{87}Sr has $\Gamma/2\pi \sim 1\,\mathrm{mHz}$. The usefulness of this setup thus lies in the framework of these ultranarrow optical intercombination transitions, since the augmented optical depth boosts the output power by $\mathcal{C}^2 \sim 10^4$ above bistability, where $P_{\mathrm{sig}} \propto \mathcal{C}^2$. This increase in output power makes it strong enough to be used for feedback to the laser. Since this is the only function of the cavity, it is not required to be high-Q nor is the lock limited by its thermal noise floor, but in turn this is also why a free-space version of this scheme would not be able to reach the required strongly saturated limit. The consequence is, however, that the atomic transition is considerably power broadened, which is reflected in the lock precision $\Delta\nu_{\mathrm{FWHM}}$ through β. Nonetheless, the lock precision is not degraded severely as (2.59) suggests.

2.4 Technical Considerations

Before realizing this scheme, it is in order to review the limitations imposed on us by the current status of the experiment. There is no optical lattice available, so the ^{88}Sr-atoms must be confined by other means during spectroscopy of $\left|{}^1\mathrm{S}_0\right\rangle \rightarrow \left|{}^3\mathrm{P}_1\right\rangle$. One way to do so is simply by keeping the atoms in the initial 461 nm magneto-optical trap (MOT), but this potentially brings about some consequences, which are investigated in the following.

First of all, we start by quantifying which atoms will mainly contribute to the nonlinear signal when interrogation is performed in the 461 nm-MOT. An atom moving with velocity

v_z along the interrogation axis will be resonant with a red-detuned (blue-detuned) counter-propagating (co-propagating) laser. Since the intracavity standing field of a laser is composed of two counter-propagating travelling waves, the profile $\mathcal{P}(\delta)$ in figure 2.9 will be shifted to $\mathcal{P}(\delta \pm v_z/\lambda)$ for some velocity class v_z. The total profile $\mathcal{P}_{\text{tot}}$ can then be obtained by integrating over all velocity classes

$$\mathcal{P}_{\text{tot}}(\delta) = \int_{-\infty}^{\infty} f(v_z)[\mathcal{P}(\delta + v_z/\lambda) + \mathcal{P}(\delta - v_z/\lambda)]\, dv_z, \tag{2.60}$$

where $f(v_z)$ is the Maxwell-Boltzmann velocity distribution. As an example, the total profile for a cloud temperature 0.1 mK is shown in figure 2.10. The signal around resonance is mainly due to atoms with $v_z \sim 0\,\text{m/s}$ and this is found to be the case for cloud temperatures up to $T \sim 5\,\text{mK}$.

We have assumed that all atoms are subjected to the same intracavity power, which is not correct since an atom with $v_z \neq 0\,\text{m/s}$ mainly interacts with one of the intracavity travelling waves for a given detuning δ, whereas atoms with $v_z \sim 0\,\text{m/s}$ interact with both. Nonetheless, taking into account the variation in P_{in} with v_z will not change the fact that only atoms within the velocity class $|v_z| \lesssim v_D = \Gamma/k$ contribute to the nonlinear behavior around resonance. Consequently, only they will be treated in the following, but it is important to keep in mind that a more elaborate analysis is required in order to find the experimental profile that accounts for all velocity classes.

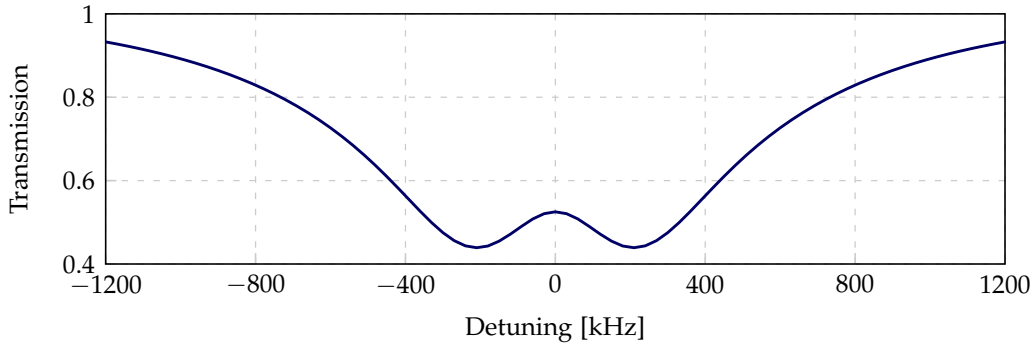

Figure 2.10: The transmission profile $\mathcal{P}_{\text{tot}}(\delta)$ resulting from cavity-enhanced nonlinear spectroscopy of an atomic cloud with temperature $T = 0.1\,\text{mK}$, after integrating over all velocity classes.

Given that only a minor fraction of the velocity distribution is relevant to us, the MOT-population must have a certain value in order to interrogate the desired $5 \cdot 10^6$ atoms that were used to generate the signal in figure 2.9. Specifically, the fraction of atoms probed along z at the realistic cloud temperature $T = 1\,\text{mK}$ with velocities within $v_D = \Gamma/k$ is

$$\chi = \sqrt{\frac{m}{2\pi k_B T}} \int_{-v_D}^{v_D} e^{-mv_z^2/(2k_B T)}\, dv_z \approx 0.01, \tag{2.61}$$

such that $5 \cdot 10^8$ atoms as a minimum must be confined. This will require optimal alignment, since the trapping beams have a significant impact on the cloud temperature, which determines χ. Misalignments between the cloud and the interrogation laser will also make it practically impossible to see a signal, since the contrast between the maximum and minimum of the transmission signal is very sensitive to N, as shown in figure 2.11. Despite this, these trap populations and temperatures are realistic to obtain.

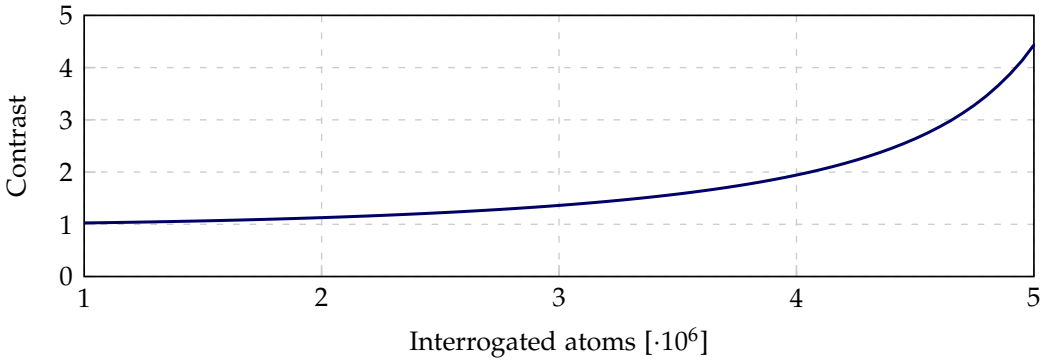

Figure 2.11: The ratio between the maximum and minimum transmission in cavity-enhanced nonlinear spectroscopy. With $P_{\text{in}} = 2.5\,\mu\text{W}$ ensemble sizes $N > 5 \cdot 10^6$ atoms brings us into the optically bistable domain.

Another issue is that the MOT-coils should ideally be turned off during the measurement such that the transition is not Zeeman broadened. This is motivated by the fact that the cloud has a finite spatial extension, so the Zeeman shift is not identical for all atoms. Since a single multi-layered coil basically constitutes an LR-circuit, there is a finite transient time $\tau = L/R \sim 3\,\text{mH}/0.2\,\Omega \sim 15\,\text{ms}$ when switching off the current. As the atoms escape the trap within a few ms after turning it off, it is necessary to retain the magnetic field during interrogation and instead quantify the resulting perturbation. It is not apriori clear what to expect since the quantization axis varies inside the MOT, but this is investigated further in the following section. We will start by introducing the necessary formalism using a two-dimensional model, after which we will analyze the current situation.

2.4.1 Narrow Line Spectroscopy in a Quadropole Magnetic Field

We consider an atom compromised of a $J = 0$ ground state and $J' = 1$ excited state with transition linewidth Γ. We place it at the origin $(0, 0, 0)$ and assume that no external magnetic field perturbs it. The atom is irradiated by a coherent laser, whose polarization direction **E** is parallel to **x**, as illustrated in figure 2.12.

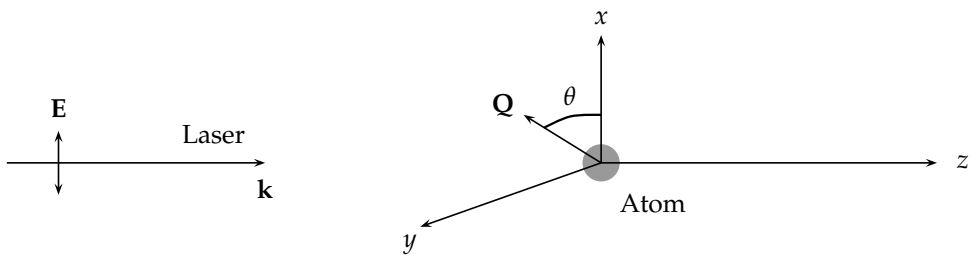

Figure 2.12: An atom irradiated by a coherent, linearly polarized drive. The angle between the polarization direction **E** of the laser and quantization axis **Q** is denoted by θ.

We regard the electron as a classical oscillator: The polarization of the radiation required to excite a given motion, and the corresponding quantum transition, is the same as that emitted. Labelling the electronic motion requires choosing a quantization axis, which is arbitrary in this

case. The natural choice for the present symmetry is **x**, in which case the incoming photons will drive the π-transition ($m_{J'} - m_J \equiv \Delta m_J = 0$) of the atom. However, σ-transitions are driven when it is chosen to lie along **y**, since electronic circular motion about the y-axis looks linear when looking in the (x, z)-plane so the incoming laser only has a σ-component for this choice. We can generalize this to an arbitrary quantization direction **Q** in the (x, y)-plane

$$\mathbf{Q} = (x_Q, y_Q, 0)^T, \tag{2.62}$$

from which the amount of the two transitions driven relative each other can be found by decomposing **E** into a component parallel (π) and perpendicular (σ) to **Q**. Denoting the angle between **E** and **Q** by θ, the π-component is thus determined by the projection $\mathbf{E} \cdot \mathbf{Q} = E\sqrt{x_Q^2 + y_Q^2}\cos\theta = Ex_Q$ such that the relative strength of the π-transition is

$$\cos\theta = \frac{x_Q}{\sqrt{x_Q^2 + y_Q^2}}. \tag{2.63}$$

The remaining part of **E** lies in the plane to which **Q** is normal, so σ-transitions are quantified by

$$\sin\theta = \frac{y_Q}{\sqrt{x_Q^2 + y_Q^2}}. \tag{2.64}$$

The total spectrum $\mathcal{S}(\delta)$ for this configuration as a function of the detuning δ between the two levels is then given by

$$\mathcal{S}(\delta) = \mathcal{L}_\pi(\delta)\cos^2\theta + \left(\frac{1}{2}\mathcal{L}_{\sigma^+}(\delta) + \frac{1}{2}\mathcal{L}_{\sigma^-}(\delta)\right)\sin^2\theta, \tag{2.65}$$

and since $\mathcal{L}_\pi(\delta) = \mathcal{L}_{\sigma^\pm}(\delta)$ in the abscence of a magnetic field, $\mathcal{S}(\delta) = \mathcal{L}_\pi(\delta)$ for an arbitrary choice of θ as required. In the limit $\theta \to 0$ ($\theta \to \pi/2$) the π-transition (σ-transition) is driven as required.

This two-dimensional model calculation has introduced the necessary formalism to treat the three-dimensional case relevant to us, namely where an inhomogeneous magnetic field is applied to the atom. In a MOT the trapped atoms are subjected to the quadropole field

$$\mathbf{B} = (-x, -y, 2z)^T B_0, \tag{2.66}$$

where B_0 is the field gradient in units of T/m. The quantization axis is chosen such that $\mathbf{Q} \parallel \mathbf{B}$ in order to simplify the calculations. We generalize the situation to describe an ensemble of two-level atoms, spatially distributed according to

$$\mathcal{G}(x, y, z) = \frac{1}{(\Sigma\sqrt{2\pi})^3} e^{-(x^2+y^2+z^2)/2\Sigma^2}, \tag{2.67}$$

where $\Sigma \simeq 0.42\,\text{mm}$ such that the cloud FWHM $= 2\Sigma\sqrt{2\ln 2} \simeq 1\,\text{mm}$, which is a realistic number. The interrogation laser will be incident from the radial direction in the experiment, so in order to accomodate the symmetry we will take $\mathbf{E} \parallel \mathbf{z}$ and $\mathbf{k} \parallel \mathbf{x}$, given (2.66). Nonetheless, the same reasoning applies here, so the relative strength of the π-transition at some point $r = (x, y, z)$ is determined by

$$\cos\theta = \frac{2z}{\sqrt{x^2 + y^2 + 4z^2}}, \tag{2.68}$$

where θ refers to the angle between **E** and **B** at r. Similarly we obtain for the σ-transitions

$$\sin\theta = \frac{\sqrt{x^2+y^2}}{\sqrt{x^2+y^2+4z^2}}. \tag{2.69}$$

The respective signal profiles $\mathcal{S}_{\pi,\sigma}$ are determined by integrating over the entire atomic cloud

$$S_\pi(\delta) = \int_{\mathbb{R}} \cos^2\theta\, \mathcal{G}(x,y,z)\mathcal{L}_\pi(\delta)\, dxdydz \tag{2.70}$$

$$S_\sigma(\delta) = \int_{\mathbb{R}} \frac{\sin^2\theta}{2}\, \mathcal{G}(x,y,z)[\mathcal{L}_{\sigma^+}(\delta) + \mathcal{L}_{\sigma^-}(\delta)]\, dxdydz, \tag{2.71}$$

where the normalized Lorentzian profiles are given by

$$\mathcal{L}_\pi(\delta) = \frac{\Gamma}{2\pi}\frac{1}{\delta^2+\Gamma^2/4} \tag{2.72}$$

$$\mathcal{L}_{\sigma^\pm}(\delta) = \frac{\Gamma}{2\pi}\frac{1}{(\delta \mp B_0\nabla_B\sqrt{x^2+y^2+4z^2})^2+\Gamma^2/4} \tag{2.73}$$

with $\nabla_B = \mu_B/h = 1.4\,\mathrm{MHz/G}$. For a vanishing magnetic field gradient we obtain $\mathcal{S}_\pi(\delta) + \mathcal{S}_\sigma(\delta) = \mathcal{L}_\pi(\delta)$ as required. The same is obtained if instead $\sigma \to 0\,\mathrm{mm}$, since the Gaussian distribution tends to a Dirac δ-function centered around the origin. For all other cases the expressions (2.70)-(2.71) have to be evaluated numerically. This can be done efficiently by utilizing the cylindrical symmetry of the problem to express (2.68)-(2.69) in cylindrical coordinates. The resulting profiles for the transition $|{}^1\mathrm{S}_0\rangle \to |{}^3\mathrm{P}_1\rangle$ are shown in figure 2.13.

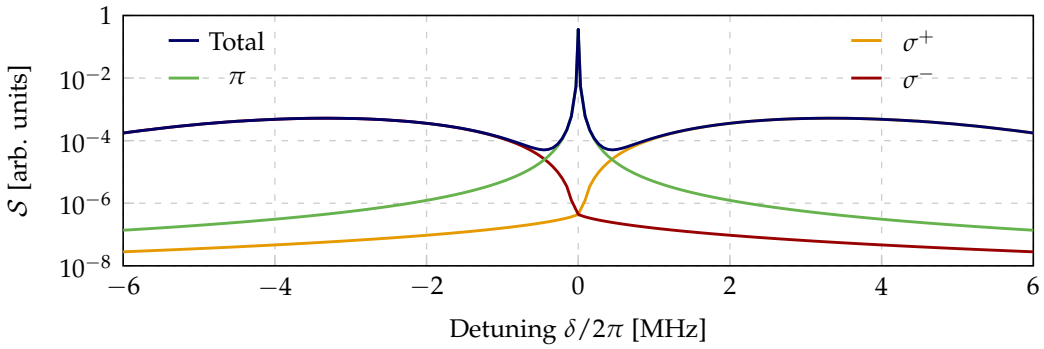

Figure 2.13: Line profile $\mathcal{S}$ for the various transitions of $|{}^1\mathrm{S}_0\rangle \to |{}^3\mathrm{P}_1\rangle$ of ^{88}Sr in a quadropole magnetic field, assuming an atomic cloud normally distributed with FWHM $= 1\,\mathrm{mm}$. The field gradient has the typical value $B_0 = 4\,\mathrm{G/mm}$.

The profiles reveal that the π-transition is unaltered by the presence of the quadropole field, since it is not Zeeman-shifted to first order. In contrast, the σ-transitions are spread out over a large spectral area due to the spatial extension of the atomic cloud and the spatially dependent magnetic field. This latter observation means that the contrast $\mathcal{S}_\pi(\delta=0)/[\mathcal{S}_{\sigma^+}(\delta=0)+\mathcal{S}_{\sigma^-}(\delta=0)]$ increases with increasing magnetic field gradient and/or cloud size.

Specifically, around resonance $|\delta| \lesssim 0.3\,\mathrm{MHz}$ the π-transition is more than five orders of magnitude larger than the σ-transition. Thus, the conclusion is that the anticipated peak in figure 2.9 is not affected by the presence of the quadropole field. If instead $\mathbf{E} \parallel \mathbf{y}$ the σ-transitions are scaled by almost a factor of two due to the quadropole cylindrical symmetry,

but the contrast between the amplitudes still persists and we are, consequently, not sensitive to the specific plane of polarization **E**. The same conclusion holds for any linear combination constituting **E**, which is relevant since experimentally **E** will be slightly elliptical.

This model also reveals why it is important to place the cloud at the origin of the field, since mainly σ-transitions will be driven if the cloud is positioned along **x** or **y** when $\mathbf{E} \parallel \mathbf{z}$.

It should be noted that these observations are ultimately possible since the linewidth $\Gamma \sim$ kHz is narrow enough to see the effect of the varying Zeeman shifts for cloud sizes approaching 1 mm. If instead $\Gamma \sim$ MHz the cloud would have to be at least twice as large to obtain shifts large enough to yield a contrast comparable to the above, or the gradient could be increased as an alternative.

2.5 Summary

This calculation concludes the current chapter, where the basic theory behind the planned cavity-enhanced nonlinear spectroscopy has been presented. Additionally, its relevance to laser stabilization against ultranarrow optical transitions has been treated. The scheme is to be implemented using ^{88}Sr, and due to the lack of an optical lattice, the atoms have to be interrogated while confined in the MOT. We have shown that this is possible in theory, but optimal alignment of the trapping beams is required in order to minimize the cloud temperature, which in turn will maximize the SNR. Furthermore, a stronger requirement is put on the trapped population.

Since the experiment is currently in its initial stages, the next chapters will be concerned with design and construction of the Zeeman slower and MOT needed to obtain the desired trapped population $\sim 5 \cdot 10^8$ atoms.

Chapter 3

Deceleration of Neutral Atoms

An atom has external degrees of freedom related to the motion of its center of mass in addition to its internal degrees of freedom realized by the level structure. Due to conservation of momentum and energy, interaction with an electromagnetic field will thus perturb the external variables of the atom in addition to its internal electronic states, serving as a handle on the atomic velocity and thus position. In the following the theory behind atomic deceleration is presented, which is then utilized to design and construct a device capable of producing slow ^{88}Sr atoms, which enables subsequent optical trapping.

3.1 The Mechanical Effects of Light

Consider a neutral atom of mass m and momentum p in free space perturbed by a monochromatic field with angular frequency ω. The field is quasi-resonant with a single closed atomic transition between the groundstate $|g\rangle$ and the excited state $|e\rangle$ with radiative lifetime $1/\Gamma$. The incident radiation is treated as a classical field with a photon flux much larger than the flux of photons being absorbed by the atom. Any radiative shifts of the levels are assumed included in the eigenfrequencies.

Upon excitation the atom is promoted from the combined state $|p, g\rangle$ to $|p + \hbar k, e\rangle$. This is a simple two-body problem, so the resonance condition of this event is from the kinematics given by

$$\omega_{\text{res}} = (\omega_e - \omega_g) + \frac{(p + \hbar k)^2}{2m\hbar} - \frac{p^2}{2m\hbar} \tag{3.1}$$

$$= (\omega_e - \omega_g) + \frac{pk}{m} + \frac{\hbar k^2}{2m}, \tag{3.2}$$

where the second and third term in (3.2) denote the first-order non-relativistic Doppler shift and the recoil shift of the atom, respectively. Unlike the Doppler shift, the recoil shift is seen to be an inevitable part of a scattering event. The motion of the atom can be treated classically when the step in momentum space due to a single event is so small that the interaction condition for the internal degree of freedom is not changed appreciably, i.e. under the condition

$$\omega_{\text{rec}} \equiv \frac{\hbar k^2}{2m} \ll \Gamma. \tag{3.3}$$

This is an adiabatic approximation stating that the time scale of the internal atom dynamics, characterized by $1/\Gamma$, is much faster than the external perturbation such that the internal dynamics are in equilibrium during the external motion.

The total Hamiltonian $\hat{H}$ for the system reads

$$\hat{H} = \hat{H}_A + \hat{V}_{AF}, \tag{3.4}$$

where the first term refers to the internal and external degrees of freedom of the atom. The changes in the incident classical field due to interaction with the atom are negligible and not accounted for. The atom-field Hamiltonian $\hat{V}_{AF}$ contains two contributions, namely the atom-reservoir interaction $\hat{V}_{AR}$ leading to spontaneous emission and the atom-laser interacton $\hat{V}_{AL}$. The latter term is given by the usual electric dipole approximation

$$\hat{V}_{AL} = -\hat{\mathbf{d}} \cdot \mathbf{E}(\mathbf{r}, t) \tag{3.5}$$

$$= -\hat{\mathbf{d}} \cdot \mathbf{e} E_0(\mathbf{r}) \cos[\omega t + \phi(\mathbf{r})], \tag{3.6}$$

where the external field $\mathbf{E}$ polarized along $\mathbf{e}$ has been written in general form with the atomic center of mass $\mathbf{r}$. In the limit of (3.3), a valid description of the light force acting on $\mathbf{r}$ is obtained through Ehrenfest's theorem [25]

$$\langle \hat{\mathbf{F}} \rangle \equiv \frac{d\langle \hat{\mathbf{p}} \rangle}{dt} \tag{3.7}$$

$$= \frac{1}{i\hbar} \langle [\hat{\mathbf{p}}, \hat{H}] \rangle \tag{3.8}$$

$$= -\langle \nabla \hat{V}_{AL} \rangle. \tag{3.9}$$

With the average dipole given by (2.38) these assumptions yield

$$\langle \hat{\mathbf{F}}(\mathbf{r}, t) \rangle = \sum_l \left\langle \hat{d}_l \right\rangle \nabla E_l(\mathbf{r}, t) \tag{3.10}$$

$$= \sum_l \left\langle \hat{d}_l \right\rangle e_l [\cos(\omega t) \nabla E_0(\mathbf{r}) - \sin(\omega t) E_0(\mathbf{r}) \nabla \phi(\mathbf{r})] \tag{3.11}$$

for $l \in \{x, y, z\}$, where e_l denotes a component of $\mathbf{e}$. The time origin has without loss of generality been chosen such that the phase is zero at the initial position of the atomic center of mass[1]. Due to the adiabatic following in (3.3), (3.11) is thus determined by the steady-state values of u and v, the components of the Bloch vector in phase and in quadrature with the average dipole moment, respectively. Utilizing these expressions in (3.11) and time-averaging $\langle \hat{\mathbf{F}}(\mathbf{r}, t) \rangle$ over an optical period yields the following expression for the mean radiative force $\mathcal{F}$ acting on the atomic center of mass $\mathbf{r}$

$$\mathcal{F}(\mathbf{r}) = (\mathbf{d}_0 \cdot \mathbf{e})[u_{t\to\infty} \nabla E_0(\mathbf{r}) + v_{t\to\infty} E_0(\mathbf{r}) \nabla \phi(\mathbf{r})] \tag{3.12}$$

$$= -\hbar \Omega(\mathbf{r}) u_{t\to\infty} \frac{\nabla \Omega(\mathbf{r})}{\Omega(\mathbf{r})} - \hbar \Omega(\mathbf{r}) v_{t\to\infty} \nabla \phi(\mathbf{r}) \tag{3.13}$$

$$\equiv \mathcal{F}_R(\mathbf{r}) + \mathcal{F}_D(\mathbf{r}). \tag{3.14}$$

The first term is the usual reactive term involving no energy absorption from the driving field, since it is proportional to the first component u of the Bloch vector. Writing out the expression for $\mathcal{F}_R$ yields

$$\mathcal{F}_R(\mathbf{r}) = -\frac{\hbar\delta}{4} \frac{\nabla \Omega(\mathbf{r})^2}{\delta^2 + \Gamma^2/4 + \Omega(\mathbf{r})^2/2} \tag{3.15}$$

$$\approx -\nabla \frac{\hbar \Omega(\mathbf{r})^2}{4\delta} \tag{3.16}$$

[1] A nonzero phase could be retained, in which case it should also be included in the derivation of the optical Bloch equations, since the atomic dipole follows the local phase of the electric field. However, the specific value is rendered irrelevant when taking the temporal average of the mean force.

where $\delta = (\omega - \omega_0) - \mathbf{k}\cdot\mathbf{v} \equiv \delta_0 - \mathbf{k}\cdot\mathbf{v}$ denotes the Doppler-shifted detuning and $\delta \gg \Omega$ has been assumed in the last step. This shows that the reactive force derives from a conservative potential corresponding to the AC Stark shift induced by the applied field. In the dressed state picture, the origin of the reactive force is thus clear [26]: The atoms remain in their ground state for a far off-resonance driving field, but they can reduce their potential energy by moving to a region where the AC Stark shift lowers the ground state energy. The sign of the detuning determines the response of the atoms to $\mathcal{F}_R$, i.e. atoms are attracted to field maxima (minima) for a red-detuned (blue-detuned) driving field. This constitutes the dipole force.

A running wave has a phase gradient given by $\nabla\phi(\mathbf{r}) = -\mathbf{k}$ and in addition $\mathcal{F}_R$ vanishes when no field gradient is present, leaving

$$\mathcal{F}_D(\mathbf{r}) = \hbar\mathbf{k}\frac{\Gamma}{2}\frac{s_0(\mathbf{r})}{1 + s_0(\mathbf{r}) + (2\delta/\Gamma)^2} \tag{3.17}$$

$$= \hbar\mathbf{k}\Gamma\rho_{ee,t\to\infty} \tag{3.18}$$

with the on-resonance saturation parameter defined through the two-level saturation intensity

$$s_0(\mathbf{r}) \equiv \frac{2\Omega(\mathbf{r})^2}{\Gamma^2} = \frac{I(\mathbf{r})}{I_{\text{sat}}}. \tag{3.19}$$

The interpretation of (3.18) is clear: Upon absorbing a photon, the atom recieves a recoil $\hbar\mathbf{k}$. If this is followed by stimulated emission, no net momentum is transferred to the atom since the recoil is in the opposite direction of the absorbed recoil. However, if absorption is followed by spontaneous emission, there is for times $t \gg 1/\Gamma$ a net momentum transfer to the atom as this occurs randomly in 4π. The net dissipative force thus reduces to the absorption recoil $\hbar\mathbf{k}$ weighted by the scattering rate $\Gamma\rho_{ee,t\to\infty}$. Unlike the reactive term, for $s_0 \to \infty$ the dissipative force saturates to

$$\mathcal{F}_D(\mathbf{r}) \to \hbar\mathbf{k}\frac{\Gamma}{2}, \tag{3.20}$$

which is a consequence of the fact that a two-level atom in steady-state absorbs and spontaneously emits a photon at the maximum rate $\Gamma/2$. For the broad transition $\left|{}^1\mathrm{S}_0\right\rangle \to \left|{}^1\mathrm{P}_1\right\rangle$ transition in ^{88}Sr with $\Gamma/2\pi = 32\,\mathrm{MHz}$ this force corresponds to an acceleration $9.90 \cdot 10^5\,\mathrm{m/s^2}$, more than 10^5 times the gravitational acceleration.

3.2 Zeeman Slower for Strontium

In order to load a MOT, a sufficient flux of atoms slower than the trap capture velocity is required. The deceleration associated with the interaction with light suggests the use of the dissipative force to slow the atoms down from thermal velocities after effusing from the oven.

Having an atom interact with a counter-propagating resonant laser beam in a uniform magnetic field will slow it down until the change in Doppler shift takes it out of resonance. This occurs when the Doppler shift is roughly half the natural linewidth, which in velocity space corresponds to merely few tens of m/s. One way to keep the atom in resonance during the slowing process is to chirp the laser frequency to match the varying Doppler shift [27]. In practice the frequency is swept over a range of more than a GHz during a few ms. However, this results in a pulsed slow atomic beam at a rate corresponding to the sweeping rate. Since the resonance condition only depends on speed, transverse losses are invariably increased as a significant amount of atoms are slowed immediately after the oven rather than right before the trap.

A far superior method is to construct a Zeeman slower, which consists of an inhomogeneous magnetic field engineered such that the varying Doppler shift is compensated for by the first-order Zeeman shift, resulting in a continuous cold atomic beam. This also has the advantage that the resonance condition depends on both speed and position. Atoms with velocities below the slower capture velocity will thus satisfy the resonance condition at some later point in the slower and be decelerated for the remaining length. Transverse losses are still prevalent due to transverse heating of the atomic beam associated with longitudinal deceleration, but considerably reduced. The effective detuning for this setup reads

$$\delta = \delta_0 - \mathbf{k}\cdot\mathbf{v} - \frac{\mu'}{\hbar}B(z) \tag{3.21}$$

$$= \delta_0 + kv_z - \frac{\mu'}{\hbar}B(z) \tag{3.22}$$

for $\mu' = (m_{J,e}g_{J,e} - m_{J,g}g_{J,g})\mu_B$, where μ_B is the Bohr magneton, g_J the Landé factor and $B(z)$ the magnetic field along z.

The maximum value of the local deceleration is determined by (3.17) at resonance, $\delta = 0$. Slowing atoms with this maximum force is an unstable process, since any increase in the atomic velocity due to imperfections in the experimental magnetic field profile will decrease the slowing force. As a consequence the discrepancy between the ideal and actual phase space trajectory will increase until the atom is finally irreversibly lost from the slowing process. This can be circumvented by choosing the deceleration $\ddot{z}$ such that $\ddot{z} = \varepsilon\ddot{z}_{\max}$ for some slowing parameter $\varepsilon \in [0,1]$, which is equivalent to imposing a condition on the field gradient along the slower axis since

$$|\ddot{z}| = \left|v_z\frac{dv_z}{dz}\right| = \left|\frac{v_z}{k}\frac{\mu_B}{\hbar}\frac{dB(z)}{dz}\right| < |\ddot{z}_{\max}|. \tag{3.23}$$

The design parameters for this system are seen to depend strongly on the specific atom to be slowed.

Solving for $B(z)$ in $\mathcal{F}_D = \varepsilon\mathcal{F}_{D,\delta\to 0}$ yields a magnetic field profile given by

$$B(z) = \frac{\hbar}{\mu'}\left(\frac{\Gamma}{2}\sqrt{[1+s_0(z)]\frac{1-\varepsilon}{\varepsilon}} + k\dot{z} + \delta_0\right), \tag{3.24}$$

where the negative solution has been chosen. From (3.21) we see that this negative solution corresponds to $\delta < 0$. The need for the parameter ε can be seen with the aid of figure 3.1: Only for $0 < \varepsilon < 1$ and the negative solution $\delta < 0$ will an unexpected increase in the velocity bring the atom closer to resonance. This auto-regulation keeps the atom in resonance despite smaller field deviations, resulting in stable deceleration.

From (3.24) it is seen that a uniform bias field can be applied for a given field profile, which allows three different field configurations. This offset does not alter the decrease in velocity since this is approximately[2] determined by the magnetic field range.

A decreasing-field geometry has its maximum at the beginning of the slowing process, and consequently the slowing laser has to be operated at a small red detuning $|\delta_0| \gtrsim \Gamma$ in order to be resonant with the slow atoms at roughly zero field conditions. This configuration requires slowing with σ^+-polarized light (with respect to $\mathbf{B}$) and was originally used by Phillips and Metcalf [28]. The slowing laser in most cases has to pass through the trap, so the main disadvantage is that the trap operation may be perturbed. Furthermore, it might slow atoms

[2] A rigorous calculation should take power broadening into account.

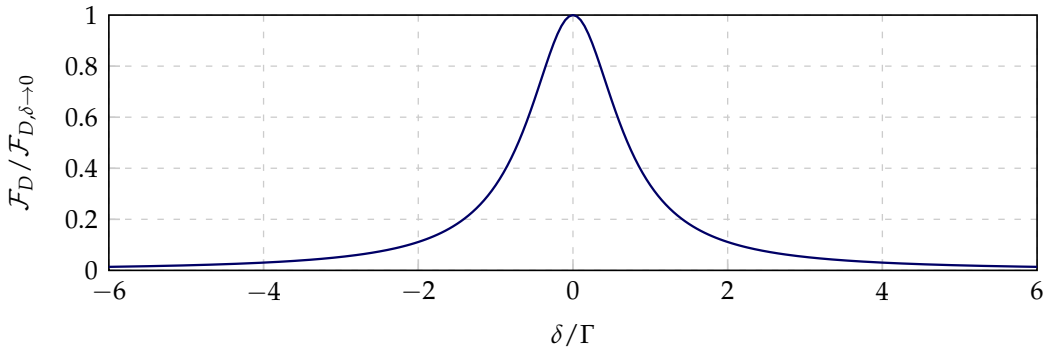

Figure 3.1: The relative dissipative force as a function of the effective frequency detuning δ.

even after they have exitted the slower, yielding a negative final velocity[3]. The advantage of this geometry is that it permits merging the field with the radial field from the MOT-coils, enabling the realization of compact setups.

An increasing-field geometry attains its maximum value at the end of the slowing distance and has zero field at the beginning. This requires slowing with σ^--light and the slowing laser has to be red-detuned by many linewidths. The extraction of slow atoms is greatly improved by the well-defined maximum and abrupt termination in resonance condition. The large residual field at the MOT may have to be balanced somehow, e.g. by compensation coils.

A spin-flip geometry combines the previous two designs: The field profile decreases at first, crosses zero at a point determined by δ_0 and reverses its direction in order to attain a maximum value. This geometry also permits a well defined field termination in addition to avoiding high field gradients close to the MOT. The required absolute field strength is reduced, which minimizes the power consumption and makes it easier to realize. Consequently, such a design is sought in the following.

3.2.1 Quantization Axis

It is in order to briefly review the dynamics during slowing for the chosen configuration. The local direction of the **B**-field defines the quantization axis, which changes direction roughly midway. The slowing transition thus changes label from σ^+ to σ^-, as illustrated in figure 3.2. Most often, however, a fixed quantization axis is chosen such that a zero-crossing of the magnetic field only leads to inversion in the sign of the magnetic sublevel Zeeman shift. This will be the convention used from now on.

Even though the atoms retain their magnetic moment orientation when crossing the zero field, it is flipped in the reference frame of the magnetic field, thus coining the term "spin-flip". It should be noted that it is possible that the atomic spin cannot adiabatically follow the varying quantization axis, which would cause redistribution amongst different magnetic hyperfine sublevels and thus leakage to potential dark states. This poses no issue in the current system since ^{88}Sr has no nuclear spin.

3.2.2 Theoretical Design

The field profile is analytically given for a uniform deceleration, but this assumption is not correct since the slowing light is often tightly focused on the opening aperture of the oven.

[3]It should be noted that these issues can in principle be circumvented entirely by adding a bias field.

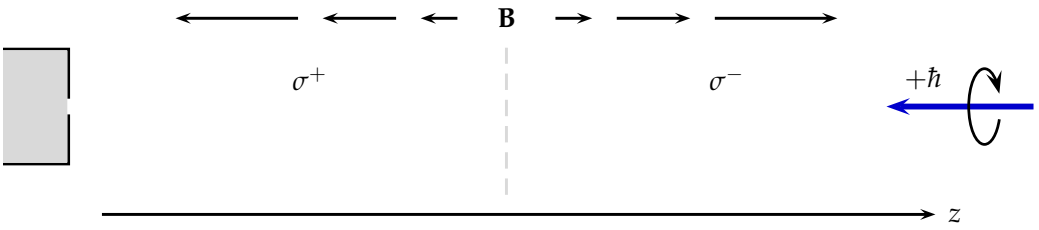

Figure 3.2: The evolution of the slowing light polarization in the atomic frame of reference for a spin-flip Zeeman slower. In the first section, after the atom has effused from the oven, the atomic spin is aligned with the quantization axis, whereas the relative orientation is reversed when the magnetic field increases in the last part. Note that changing the current polarity requires changing the handedness of the slowing light.

This maximizes the overlap between the dissipative force and the expanding atomic beam and provides additional transverse cooling of the atoms. By solving the equations of motion numerically one will find that the assumption of uniform deceleration is invalid even for the simplest case of collimated light. Nonetheless, many successful designs are based on this analytical expression, e.g. [29–31]. In order to keep things general, we abandon this assumption and determine the field profile through the phase space trajectory

$$\dot{v}_z = -\varepsilon \frac{\hbar k \Gamma}{2m} \frac{s_0(z)}{1 + s_0(z)} \tag{3.25}$$

$$\dot{z} = v_z \tag{3.26}$$

which we readily solve for by Runge-Kutta methods. Note that as $\left|{}^1\mathrm{S}_0\right\rangle \rightarrow \left|{}^1\mathrm{P}_1\right\rangle$ with $\Gamma/2\pi = 32\,\mathrm{MHz}$ is used for slowing, this classical picture is valid since (3.3) is satisfied. The on-axis saturation parameter for a Gaussian beam is given by

$$s_0(z) = \frac{2P}{\pi w(z)^2} \frac{1}{I_{\mathrm{sat}}}, \tag{3.27}$$

where the slowing beam has $P = 30\,\mathrm{mW}$ of available power and $I_{\mathrm{sat}} = 42.7\,\mathrm{mW/cm^2}$. In three dimensions this is generalized to

$$s(r,z) = s_0(z) e^{-2r^2/w(z)^2}. \tag{3.28}$$

The beam radius $w(z)$ is determined by the excellent approximation

$$w(z) = w_i + \frac{z}{L}(w_i - w_o), \tag{3.29}$$

where $w_i = 1\,\mathrm{mm}$ ($w_o = 8\,\mathrm{mm}$) denotes the waist at the entry (exit) of the slower and L the slower length. Setting $\varepsilon = 0.4$ and choosing the maximum slowable velocity $410\,\mathrm{m/s}$ results in a theoretical exit velocity of $23\,\mathrm{m/s}$ for $L = 30\,\mathrm{cm}$, sufficiently below the trap capture velocity estimated to be $30\,\mathrm{m/s}$. Choosing $\delta_0/2\pi = -560\,\mathrm{MHz}$ yields a symmetric field profile with $-325\,\mathrm{G}$ and $346\,\mathrm{G}$ at the ends. These parameters are inspired by [32, 33], who have obtained designs with appropriate fluxes of slow atoms and optical traps with as much 10^9 atoms.

There are generally two contributions to the expansion of the atomic beam. Since the divergence is inversely proportional to the transverse velocity component, axial slowing will

increase it. Furthermore, absorption and the subsequent spontaneous emission of photons are intrinsically stochastic processes, such that an atom does a random walk transversely leading to heating. For this reason the design exit velocity was not chosen much smaller than needed.

Slowing of Sr is very efficient due to the broad cooling transition and can be achieved on these relatively short distances, even with a small slowing parameter. In comparison, slowing of ^{87}Rb is performed on a transition with linewidth $\Gamma = 2\pi \cdot 6.07\,\mathrm{MHz}$, yielding typical lengths approaching a meter.

3.2.3 Experimental Realization

Under the assumption that the coils are connected in series, we find the desired coil configuration by summing each individual coil contribution numerically. During optimization an attempt was made to avoid unnecessary steep field gradients due to (3.23). One way to avoid this issue entirely is by using a design based on a single-layer helix with variable pitch [34], but a more conventional approach is chosen here. The final arrangement is shown in figure 3.3.

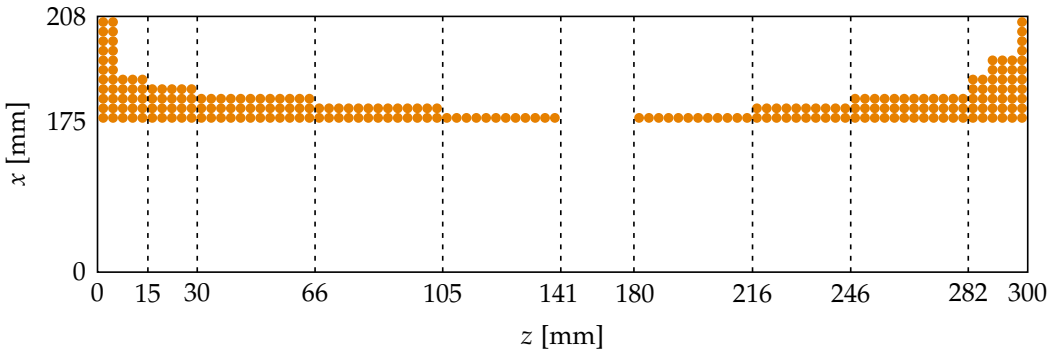

Figure 3.3: The coil configuration of the Zeeman slower resulting in a total wire length 36.4 m and 241 coils. With a Ø3 mm cobber wire the resistance is expected to be around 0.1 Ω.

The coils are wound around a 36 cm CF-16 vacuum tube, which is used to integrate the device in the vacuum system. In order to avoid residual fields at the trap, the slower is operated inside a three-layer magnetic shield. The shield has the advantage that it increases the magnetic field inside the enclosure, making it easier to obtain higher field gradients at the slower ends in addition to providing an abrupt termination of the resonant field. Even though the power consumption is only roughly 29 W, the device is water-cooled due to the enclosure.

During the numerical work the effect of the shield is modelled as creating a mirror image of the field on each side of the shield, and the effect is seen from the measurements in figure 3.4. The measurements with shielding are in good agreement with the numerical model, but the field decreases slightly slower at the edges than expected. This discrepancy may be explained by the fact that the shield is not perfectly reflecting and will ultimately result in a minor decrease in the slower capture velocity, which is readily compensated for by increasing the current and/or the detuning.

In order to verify the experimental field, the equation of motion $m\ddot{z} = F(\dot{z}, z)$ for the atoms is integrated numerically. Since there is no reason to believe that the field is not well-behaved, a smooth representation without discontinuities can be obtained by fitting a polynomial to the discrete data points z_i. Figure 3.5 shows the simulated trajectories with optimized parameters, resulting in a maximal slowable velocity of 500 m/s.

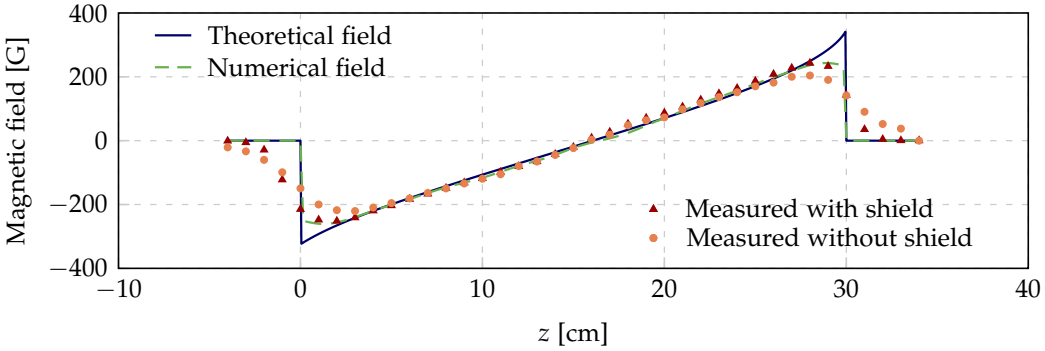

Figure 3.4: A comparison of the theoretical, numerical and experimentally realized slower field at 17 A.

For low powers the atoms drop out of the slowing process at minor field irregularities. Power broadening of the absorption profile at high saturations enables the atoms to stay in resonance at these points. Increasing the power beyond this value will increase losses due to dominating residual transverse velocities, and beyond this limit the atoms are accelerated back towards the oven. The effect of terminating the field abruptly is clearly seen, since the atoms are not slowed significantly after leaving the slower at $z = 30\,\text{cm}$.

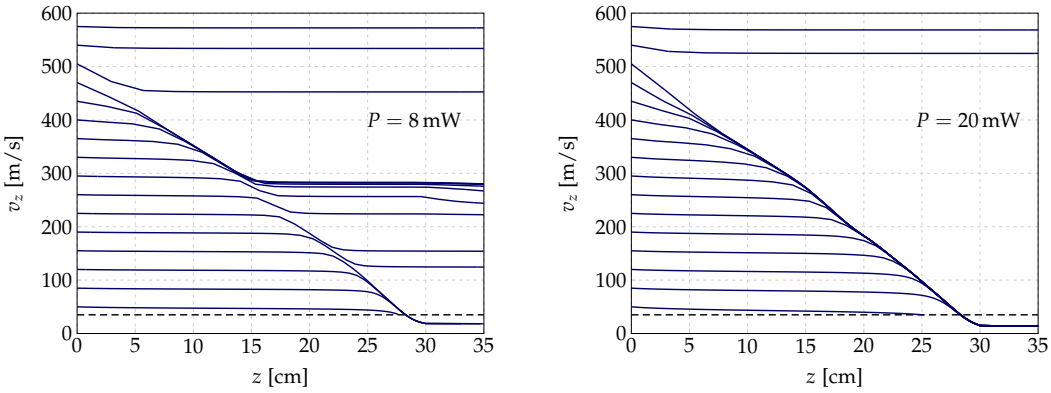

Figure 3.5: Simulated phase space trajectories of atoms in a Zeeman slower at different saturations, given a red-detuned slowing beam at $\delta_0/2\pi = -560\,\text{MHz}$. The lower dashed, horizontal line marks the MOT capture velocity assumed to be $30\,\text{m/s}$.

Following [30], the loading rate provided by the slower can be estimated by first looking at the flux F of atoms leaving the oven through an aperture of surface A in direction (v, θ, ϕ) [35]

$$dF(v,\theta,\phi) = \frac{nA}{\xi^3 \pi \sqrt{\pi}} v^3 e^{-v^2/\xi^2} \cos\theta \sin\theta \, dv d\theta d\phi, \tag{3.30}$$

where $\xi = \sqrt{2k_B T/m}$ and n the atomic number density at vapor pressure P, which is given by the ideal gas law $n = P/k_B T$. In order to accomodate the symmetry of the problem, (3.30) is

transformed to cylindrical coordinates $(v_\perp, \phi, v_z)$

$$dF(v_\perp, \phi, v_z) = \frac{2nA}{\xi^3\sqrt{\pi}} v_z e^{-v_z^2/\xi^2} v_\perp e^{-v_\perp^2/\xi^2} dv_\perp dv_z, \tag{3.31}$$

which is integrated to yield

$$F = \frac{n\xi A}{4}\left(1 - e^{-v_{\perp,\max}^2/\xi^2}\right)\left(1 - e^{-v_{z,\max}^2/\xi^2}\right). \tag{3.32}$$

The upper axial velocity is the capture velocity of the slower. Disregarding transverse heating, the upper transverse velocity is constrained by $v_{\perp,\max} = R_c/t$, where $R_c \approx 10\,\text{mm}$ is the capture radius of the MOT and t the total propagation time from oven to MOT. At thermal velocities, the time-of-flight from oven to slower can be neglegted and with constant deceleration t is given by simple kinematics, which yields

$$\mathcal{L} \simeq 9.9 \cdot 10^{10}\,\text{atoms/s} \tag{3.33}$$

for $T = 530\,^\circ\text{C}$. This is a very optimistic estimate since the main loss mechanism has been neglegted in addition to the focus of the slowing field, but gives an idea of the potential performance of the Zeeman slower. The loading rate is measured in the next chapter.

3.2.4 Transverse Motion

The rms-width of an initially well defined transverse velocity component increases due to the random walk as [36]

$$\left\langle v_\perp^2 \right\rangle = \sigma_{v,\perp}^2 = 0.9\frac{v_{\text{rec}}^2}{3}N, \tag{3.34}$$

where N is the total number of scattered photons. The deviation of the dipolar radiation pattern from an isotropic distribution is taken into account by the factor 0.9. Transverse spreading is more pronounced for lighter atoms since $v_{\text{rec}} \propto 1/\text{mass}$.

We constructed a Monte-Carlo simulation in order to correctly model this effect, utilizing the Mersenne twister [37] as the random number generator in order to avoid artifacts due to biased statistics. This requires taking into account the varying axial field off-axis. The general expressions for the axial and radial magnetic field for a circular current loop of radius R displaced by D from the origin is [38]

$$B_z(\rho, z) = \frac{\mu_0 I}{2\pi}\frac{1}{\sqrt{(R+\rho)^2 + (z-D)^2}}\left[+K(k^2) + \frac{R^2 - \rho^2 - (z-D)^2}{(R-\rho)^2 + (z-D)^2}E(k)^2\right] \tag{3.35}$$

$$B_\rho(\rho, z) = \frac{\mu_0 I}{2\pi}\frac{z-D}{\sqrt{(R+\rho)^2 + (z-D)^2}}\left[-K(k^2) + \frac{R^2 + \rho^2 + (z-D)^2}{(R-\rho)^2 + (z-D)^2}E(k)^2\right], \tag{3.36}$$

where

$$k^2 = 4\frac{R\rho}{(R+\rho)^2 + (z-D)^2} \tag{3.37}$$

and $K(k^2)$ and $E(k^2)$ are the complete elliptic integrals of the first and second kind. The variations off-axis are found to occur primarly at the critical slower ends. They are calculated to be less than 10 G and consequently deemed negligible. Furthermore, the limited power is ultimately the important parameter at large radial distances, not the minor variations in the magnetic field.

The trajectory of an atom through the slower is found by evaluating the scattering probability analogous to (3.17) [39]

$$S \equiv \frac{s_0}{1 + s_0 + (2\delta/\Gamma)^2} \tag{3.38}$$

at each timestep $\Delta t \simeq 1/\Gamma$, which is then compared to a random number $X \in [0, 1]$. An absorption event is simulated if $S > X$, in which case the direction of the subsequent change in atomic momentum is determined by the focus of the slowing beam such that it is perpendicular to the constant-phase wavefront. After a time $1/\Gamma$, the recoil due to spontaneous emission is added randomly in 4π through sphere point picking. The timesteps are chosen such that (3.20) is not violated, i.e. for $S \to 1$ the atom stays a duration $1/\Gamma$ in each state as required for a two-level atom. Due to the low power this scenario is artificial and the specific value of Δt thus not critical.

Even though the following does not constitute a formal proof, there are several observations that corroborate that this method is a valid description of the atomic motion during slowing: The stochastic evaluation of (3.38) takes into account that when the atom is in resonance, it scatters with the maximum allowed rate. In the opposite limit $s_0 \to 0$ no scattering occurs and the procedure reduces to a standard numerical integration of the classical equation of motion. Secondly, as a test 10^5 atoms were slowed from $v_\mathrm{i} = 300\,\mathrm{m/s}$ to $v_\mathrm{i} \simeq 15\,\mathrm{m/s}$, resulting in $28.8 \cdot 10^3$ scattered photons. This is in the same range as the expected value $(v_\mathrm{i} - v_\mathrm{f})/(\hbar k/m_{\mathrm{Sr}}) = 28.6 \cdot 10^3$. In return the atoms gain on average $\sigma_{v,\perp} = 0.87\,\mathrm{m/s}$ in transverse velocity, which is similar to the value $0.91\,\mathrm{m/s}$ predicted by (3.34) for an infinite ensemble. As illustrated in figure 3.6, it is able to reproduce the previous on-axis trajectories. Thus, with a correct value for the timestep Δt, the random walk in velocity space is to a good approximation integrated in real space.

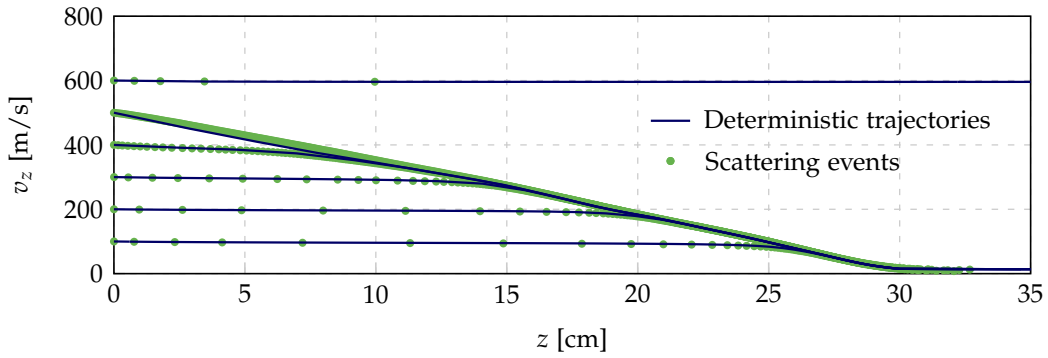

Figure 3.6: A comparison between phase space trajectories found by solving the deterministic equations of motion and by evaluating stochastic scattering events using (3.38). Only every 100th event is displayed.

The time evolution of a single two-level atom between emission events is more accurately described by quantum jumps in terms of the probability density $|\psi(t)|^2 \sim e^{-2\Gamma t}$. Implementing this variable retention time may potentially improve the statistics, but only by a small amount since the expected amount of scattering events is almost reached. Our stepwise approach outlined above is deemed sufficient for a qualitative describtion of the problem. In the presence of absorption the intensity of the slowing laser is ideally a function of atomic density [40], but the consequences of this effect are assumed negligible and not implemented either.

The effect of the slower is seen in the distributions in figure 3.7. Atoms below the capture velocity are effectively bunched into the final velocity class, accompanied by the inevitable transverse heating. This compression of the thermal distribution increases the phase space density, which is why a Zeeman slower cools the atomic beam in addition to slowing it.

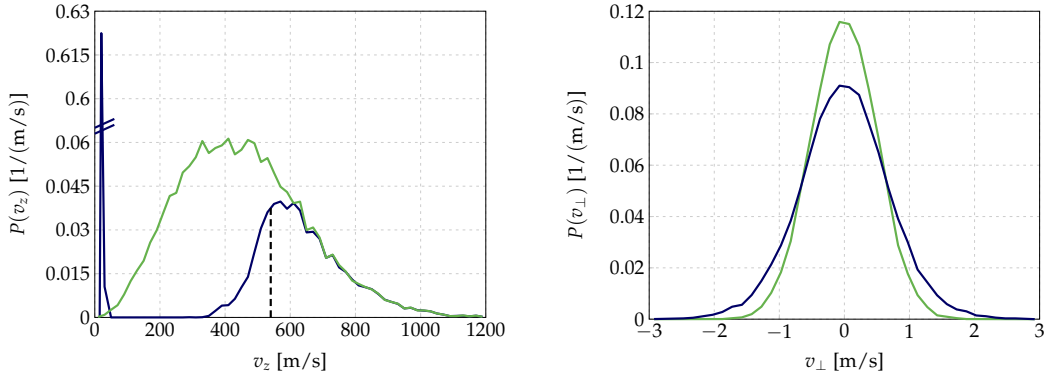

Figure 3.7: A simulation with 10^3 atoms revealing the final (blue) velocity distributions, where the dashed line indicates the slower capture velocity. The initial (green) transverse velocity distribution is assumed to be Gaussian.

3.3 Characterization

For an atom moving at a velocity v and with an angle θ relative to a probe beam, the fluorescence signal will be a Doppler-shifted Lorentzian

$$\mathcal{L}(\delta_0, v) = \frac{\Gamma/2\pi}{(\delta_0 - v\cos\theta/\lambda)^2 + \Gamma^2/4}. \tag{3.39}$$

The velocity of the cold atoms can be determined by first scanning the probe a few hundred MHz across the slowing transition. After this the velocity can be extracted by comparing the spectrum to the Doppler-free signal originating from a 90° reference. The reference is ideally used simultaneously in order to minimize possible drifts, but the feasibility of this depends on how small the velocity to be measured is. The SNR is optimized by choosing an appropriate polarization.

Figure 3.8 shows typical measurements for three different situations: When the slower is operated at 10 A, 6 A and when no slowing light is applied. The expected behavior is observed, where increasing the current increases the slower capture velocity in addition to reducing the exit velocity. There is not a sharp cutoff at the capture velocity $v_c \sim 300\,\mathrm{m/s}$ as one might naïvely expect: For a given laser power, the efficiency is ultimately limited by the atoms that drift too far from the beam center, which are subsequently lost since the small saturation parameter does not decelerate them sufficiently. Thus, slowing atoms with initial velocities around v_c is ultimately terminated if the initial transverse velocity component is too large. This loss channel is also responsible for the spread of $(31 \pm 3)\,\mathrm{m/s}$ at the end of the slower, consistent with a similar system [32] and the numerical prediction at roughly 24 m/s. For currents $\gtrsim 14$ A the cold atoms spend too much time in the probe and are scattered.

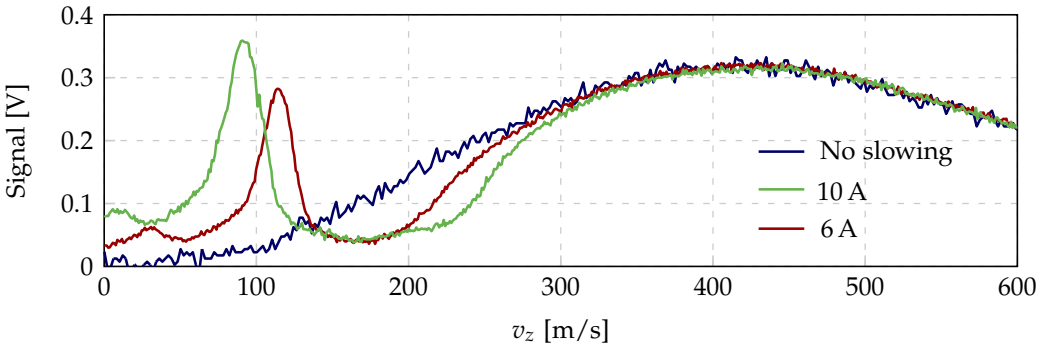

Figure 3.8: Flourescent spectra of the atoms emerging from the slower illustrating their behavior for various currents and when no slower light is applied. The small bumps occuring to the left of the main slowed peaks originate from ^{86}Sr, whose $|^1S_0\rangle \rightarrow |^1P_1\rangle$ transition is detuned by 124.8 MHz [41]. The most probable velocity around 400 m/s agrees with the expected $\sqrt{2k_BT/m} = 395\,\mathrm{m/s}$ at $T \simeq 550\,^\circ\mathrm{C}$.

Using the same parameters as in the experiment, numerically it is found that the slower increases the trap population by almost a factor of 19 compared to slowing with a 0 A-field. As illustrated in figure 3.9 a range close to that value is also found by taking the ratio between the experimental signals. This is supported by the factor of 22 observed in a similar system [42]. It must be emphasized though that currently the model treats the thermal velocity distribution of the atoms effusing from the oven approximatively, since the initial transverse velocities are merely assumed to be Gaussianly distributed. Furthermore, the dynamics of the trap has not been taken into account which may explain the quantitative disagreement. Representing the slowing beam incorrectly will most certainly also have an effect, e.g. we have measured the waists with finite precision and the beam may possess minor structure. Additionally, the experimental current can only be resolved to within 0.1 A. Most importantly, the essential

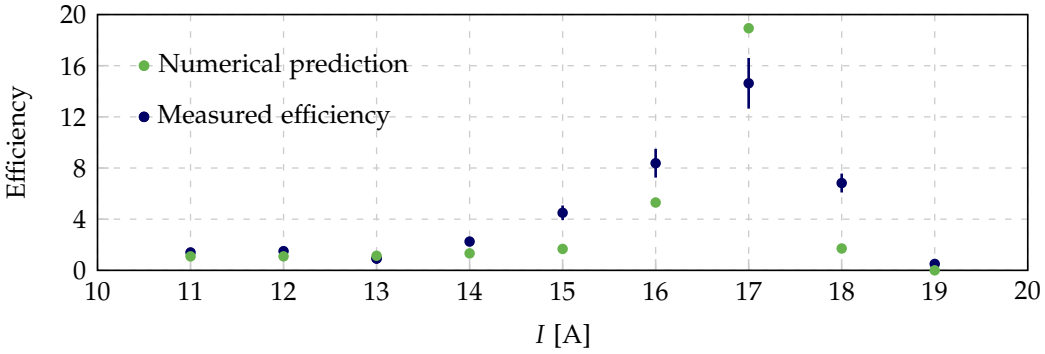

Figure 3.9: Gain in trapped atoms as a function of current through the Zeeman slower.

trends are well captured: For currents < 16 A the exit velocity is too large, whereas for $I > 18$ A all capturable atoms are turned around. The maximum signal is attained around 17 A.

3.3.1 Optimization

For a given laser power, the trap loading rate is limited by the small power away from beam center. Increasing the atomic spatial density by transverse two-dimensional cooling with a red-

detuned beam immediately after effusing from the oven has also proven to be advantageous. The anticipated and measured increase is presented in figure 3.10.

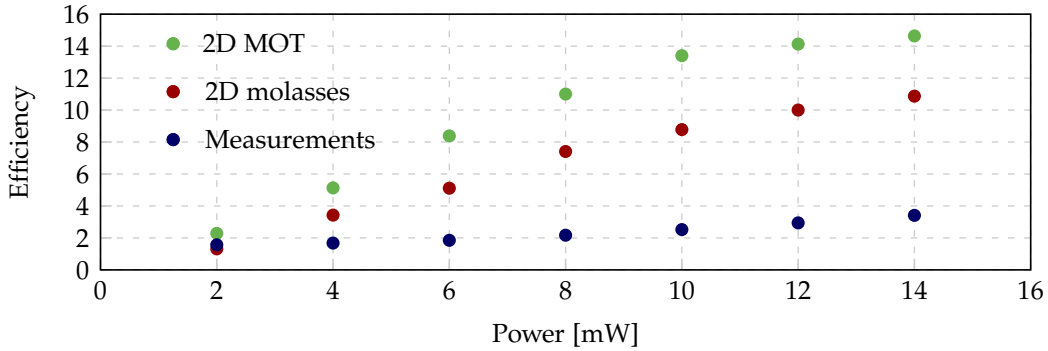

Figure 3.10: The fractional increase in atoms reaching the trap as a function of transverse cooling power. The simulation is based on 10^4 atoms, where each cooling beam measures 16 mm $\times$ 3 mm and the constant magnetic gradient is 60 G/cm. The detuning is set to $\delta_0/2\pi = -40$ MHz, the same used for the trapping beams in the experiment.

The model is optimistic since it assumes perfectly cylindrical beams with evenly distributed power. This is clearly not the case experimentally, where imperfect beam alignment can degrade the gain significantly and interference between optical elements may distort the structure. A single beam was used to cool in both dimensions, thereby maximizing the power but in addition complicating the alignment significantly. These combined effects explain the rather large discrepancy. From the numerical behavior one can infer that using more power will not increase the efficiency due to power saturation.

Applying a constant magnetic field gradient further adds to the dissipation and enables focusing the atomic beam. Including this effect yields almost an order of magnitude more atoms if carried out properly and intuitively it makes sense that the trap population is sensitive to these additions since the initial slowing area is only a few mm wide. With this effect the total slowing force along x (and y) reads

$$F_x = \frac{\hbar k\Gamma}{2}\left(\frac{ns_0}{1+2ns_0+4[(\delta_0-kv-\beta x)/\Gamma]^2} - \frac{ns_0}{1+2ns_0+4[(\delta_0+kv+\beta x)/\Gamma]^2}\right), \tag{3.40}$$

where $\beta \equiv \mu_B(dB/dx)/\hbar$, $n = 4$ is the total number of beams and the additional factor of 2 in the denominator compared to (3.17) takes into account saturation. In practice this can be realized by two sets of permanent magnets, which require less space than manually wound coils. Only 2D molasses was implemented at this stage and the final operational setup is shown in figure 3.11.

The atomic divergence can potentially be reduced further by employing a second cooling stage right after the slower, ideally where the exit velocity is attained. In the current setup geometrical constraints force a second stage to be performed 92.5 mm after the exit. Employing this feature in the model does not increase the loading rate: As trappable atoms that normally overshoot the MOT have $\sigma_{v,\perp} \gtrsim 1.2$ m/s after the slower exit, this second collimation stage does no good since many atoms will still overshoot due to its late occurrence. In fact, the prolonged time-of-flight decreases the loading rate by more than a factor of two and consequently this feature has not been implemented.

As mentioned earlier, the field from the anti-Helmholtz coils used for the MOT can in principle be used to perform the last part of the slowing process. For the present setup it is

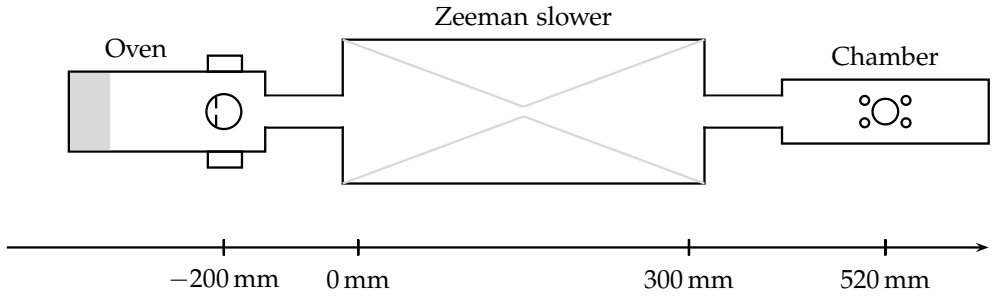

Figure 3.11: Dimensions of the final deceleration setup. Not included in the sketch are two ion pumps, which are connected to the oven (left) and the chamber (right).

thus important to choose the current-polarity of the MOT-coils such that the cold atoms are not slowed further after exitting the slower. However, it is found that when merging the two fields the trap population is experimentally increased by 54 % compared to figure 3.9 and the simulated trajectories in figure 3.12 offer a clear physical explanation: The atoms are slowed all the way to the MOT when combining the fields, effectively removing the 220 mm free time-of-flight that would otherwise occur and the subsequent overshoot by some of the atoms. The model predicts an increase by 75 %, comparable to the observation.

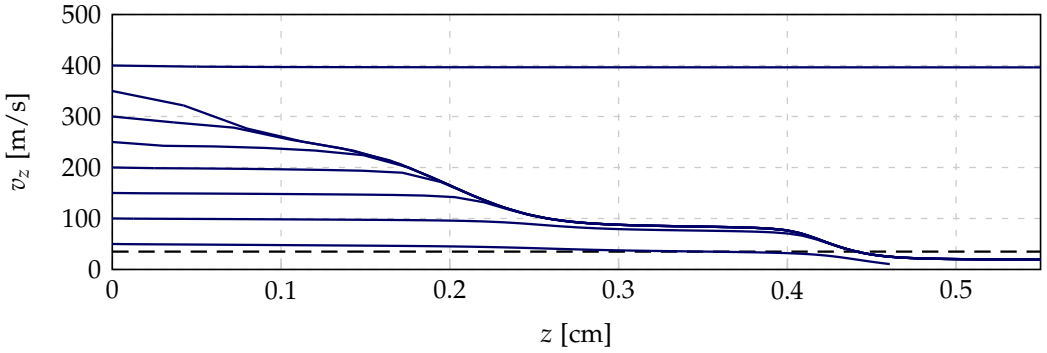

Figure 3.12: Phase space trajectories under the combined field from the Zeeman slower (11 A) and trap coils (56 A each). The field-contribution from the coils follows naturally from $\nabla \cdot \mathbf{B} = 0$ and the rotational symmetry, $-B_z/2 = B_x = B_y$.

It is worth noting that the resulting decrease in slower capture velocity is more than compensated for, showing that considerations about the solid angle with which atoms emerge from the slower are equally important for an optimal system. In retrospect this merging of the two fields should have been approached from the beginning as in [29] due to the relatively long time-of-flight after the slower. This also has the obvious benefit of reducing the total length of the experiment by at least 15 cm, since only a single half of the current slower is needed. No magnetic shield would be required either. A comparison of the steady-state signals for the various slowing configurations is illustrated in figure 3.13.

3.4 Summary

A spin-flip Zeeman slower for ^{88}Sr has been designed, built and implemented in the vacuum system. In the following chapter its loading rate is measured explicitly. In addition a simple

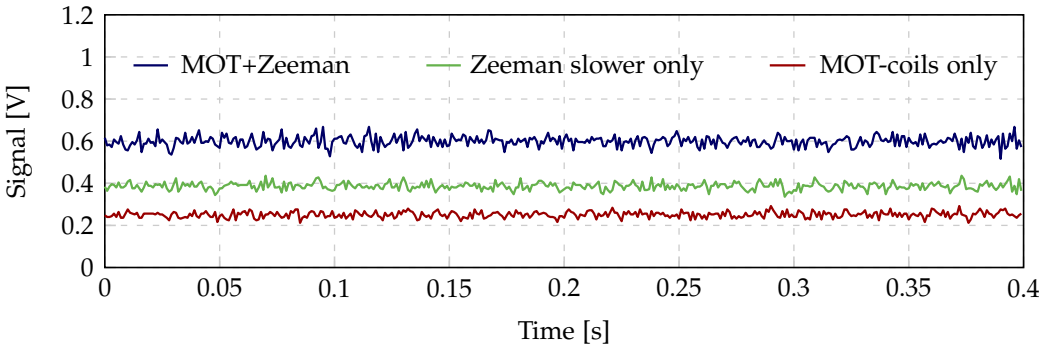

Figure 3.13: The measured steady-state MOT-flourescence for the three possible slowing configurations: Slowing with the field originating from both the slower and the MOT-coils ("MOT+Zeeman"), only the Zeeman-slower and only the field from the MOT-coils. The mean values are 0.60 V, 0.39 V and 0.25 V, respectively, and are directly comparable to eachother.

semiclassical model has been developed, which takes into account the random walk associated with atomic deceleration by photon collisions, displaying good qualitative correspondence between observations and theory. It is not apriori clear what causes the quantitative disagreement, but it is not unlikely that it may be corrected if the trap dynamics is taken into account and/or by varying the trap capture radius/velocity.

Chapter 4

Magneto-Optical Trapping of Strontium

At this stage a Zeeman slower has been implemented, so we are now capable of producing a continuous flux of cold atoms with velocities around 30 m/s. This chapter focuses on the subsequent magneto-optical trapping and optimization, which will eventually lead to the desired atomic population. The general theory of a magneto-optical trap (MOT) will be presented, including considerations on the attainable temperature and trap capture velocity. The light used for the MOT is analyzed and in addition the loss rate of the trapped atoms is investigated both analytically and experimentally.

4.1 Optical Molasses

Up until now the scattering force in form of a single laser beam has been utilized to slow down a counter-propagating atomic beam in one dimension. Atoms move in all three dimensions and their mean square velocity in all spatial directions needs to be reduced in order to cool them down. This can be achieved by three intersecting orthogonal pairs of oppositely directed beams having the same frequency and intensity. A moving atom will always experience a force opposing its direction of motion if the beams are red-detuned, since the counter-propagating beam is closer to resonance. The pair of beams can be assumed to act independently of each other in the low saturation limit $s_0 \ll 1$, in which case the force $\mathcal{F}$ in each dimension is given by

$$\mathcal{F} = \mathcal{F}_D(\delta_0 - kv) - \mathcal{F}_D(\delta_0 + kv) \tag{4.1}$$

$$\simeq 4\hbar k^2 s_0 \frac{(2\delta_0/\Gamma)}{[1 + (2\delta_0/\Gamma)^2]^2} v \tag{4.2}$$

$$\equiv -\alpha v \tag{4.3}$$

for $kv \ll \Gamma$. This represents a viscous damping force over a restricted velocity range since $\delta_0 < 0$, asymptotically reducing the atomic velocity to zero due to which (4.3) is dubbed optical molasses. The capturable velocities are $v_c \sim \pm\Gamma/k$ and the maximal damping occurs for $\delta_0 = -\Gamma/2$.

Denoting the atomic mass by m, the classical equations of motion for this model predict that for times much longer than m/α the velocity goes to zero and consequently that the attainable temperature is zero. However, the stochastic nature of both absorption and emission causes the atom to fluctuate around equilibrium, resulting in a nonzero steady-state Doppler temperature T_D determined by the cooling and heating process. In one dimension it can be estimated as follows: The atomic motion is modelled as being governed by a viscous drag characterized by

$\eta \equiv \alpha/m > 0$ in addition to a classical random Langevin force $F(t)$

$$\dot{p}(t) = -\eta p(t) + F(t). \tag{4.4}$$

By definition $\langle F(t)\rangle = 0$ and $\langle F(t)F(t')\rangle = 2\mathcal{D}G(t-t')$, where $\mathcal{D}$ is the momentum diffusion coefficient. The second-order correlation function $G(t-t')$ is a δ-function $\delta(t-t')$ since $F(t)$ is assumed to be Markovian, i.e. two timescales exist $\tau_c \ll 1/\eta$ where τ_c gives the memory time of F and $1/\eta$ the atomic damping time. Physically, this corresponds to the heavy atom colliding very frequently with the lighter particles that constitute the homogeneous fluid, but the effect of each collision is small. Note that the classical average used here is over all realisations.

The formal solution to (4.4) is readily found by integration [25]

$$p(t) = p(0)e^{-\eta t} + \int_0^t F(t')e^{-\eta(t-t')}\,dt', \tag{4.5}$$

and averaging over timescales much longer than $1/\eta$ results in $\langle p(t)\rangle = p(0)e^{-\eta t}$ as anticipated. The mean square momentum will be affected by the stochastic momentum changes, namely

$$\left\langle p^2(t)\right\rangle = \left\langle \left(p(0)e^{-\eta t} + \int_0^t F(t')e^{-\eta(t-t')}\,dt' \right)^2 \right\rangle \tag{4.6}$$

$$= p^2(0)e^{-2\eta t} + \int_0^t \int_0^t \left\langle F(t')F(t'')\right\rangle e^{-\eta(t-t')}e^{-\eta(t-t'')}\,dt'dt'' \tag{4.7}$$

$$= p^2(0)e^{-2\eta t} + 2\int_0^t \int_{-\infty}^{\infty} \mathcal{D}\delta(t-t')e^{-\eta(t-t')}e^{-\eta(t-t'')}\,dt'dt'' \tag{4.8}$$

$$= p^2(0)e^{-2\eta t} + \frac{\mathcal{D}}{\eta}\left(1 - e^{-2\eta t}\right), \tag{4.9}$$

where terms linear in $\langle F(t)\rangle$ vanish and the limits in (4.8) have been extended to $\pm\infty$, which is valid as $t \gg \tau_c$. The average kinetic energy K thus tends towards $K = \mathcal{D}/(2m\eta)$. In this long-time limit $\eta t \gg 1$ the combined system consisting of atom and bath is in equilibrium, due to which K is also given by its equipartition value $K = k_B T/2$. Comparing expressions yields the first fluctuation-dissipation theorem

$$\mathcal{D} = m\eta k_B T, \tag{4.10}$$

originally derived by Einstein and linking the friction and diffusion $\mathcal{D}$ experienced by the particle to its equilibrium temperature T.

The Doppler cooling limit should ideally be derived by a microscopic Langevin approach, through which the quantum analogue of $F(t)$ can be found. The following line of reasoning is, however, also applicable [43]: In random-walk theory $\mathcal{D}$ is defined as $\mathcal{D} = d\left\langle \Delta p^2\right\rangle/dt$, where $\left\langle \Delta p^2\right\rangle$ is the mean square momentum increase. As spontaneous emission occurs with step size $\hbar k$, in this framework $\mathcal{D} = \hbar^2 k^2 \Gamma \rho_{ee,t\to\infty}$. Absorption events are uncorrelated for $s_0 \ll 1$ and thus follow the same statistics, due to which the total total diffusion coefficient becomes $2\hbar^2 k^2 \Gamma \rho_{ee,t\to\infty}$. Inserting expressions in (4.10) yields

$$k_B T_D = \frac{\hbar}{2}\frac{\delta_0^2 + \Gamma^2/4}{\delta_0}, \tag{4.11}$$

where T_D is known as the Doppler temperature. This has the well-known minimum $\hbar\Gamma/2$ at $\delta_0 = -\Gamma/2$, independent of the atomic mass and optical wavelength. This result also holds in

three dimensions, since the diffusion is generalized to $\mathcal{D} \to 3\mathcal{D}$, where the additional factor is compensated by the factor gained when generalizing K in (4.10) via the equipartition theorem.

A three-dimensional optical molasses is thus a velocity-dependent scattering force, leading to compression in momentum-space. As long as the light can drive transitions between the two states, the incoming polarization does not matter. Often the various magnetic substates of an atom in combination with the polarization of the light are important, in which case the above theory is rendered inexact, resulting in samples approaching the recoil limit through sub-Doppler cooling. As even-isotope alkaline earth atoms have no nuclear spin and thus no magnetic substates, the temperature of ^{88}Sr is ultimately Doppler-limited.

4.2 Magneto-Optical Trap

The concept of optical molasses can be extended beyond momentum-space by adding to it a position-dependent force resulting in spatial confinement as well. Employing a one-dimensional model again, the principle behind a MOT can be explained by looking at an atom with a $J = 0$ ground state and $J' = 1$ excited state[1] with magnetic sublevels $m_{J'} = 0, \pm 1$. The atom is placed in a linearly increasing magnetic field with zero at the trap center, and irridiated by two counter-propagating laser beams of opposite helicity. The beams are red-detuned with respect to the unperturbed transition. For positions $z > 0$ ($z < 0$) the associated Zeeman shift tunes the $\Delta m_J = -1$ ($\Delta m_J = +1$) transition closer to resonance. With the transition selection rules in mind, sending in the $\sigma^{\mp}$-polarized beam in from $\pm z$ thus yields a spatially dependent scattering force, which pushes the atom back towards $z = 0$. Utilizing (3.21) in (4.1) yields for a linear magnetic field $B = B_0 z$

$$F = \mathcal{F}_D^{\sigma^+}(\delta_0 - kv - \mu' B/\hbar) - \mathcal{F}_D^{\sigma^-}(\delta_0 + kv + \mu' B/\hbar) \tag{4.12}$$

$$\simeq 4\hbar k^2 s_0 \frac{(2\delta_0/\Gamma)}{[1 + (2\delta_0/\Gamma)^2]^2} v + 4\hbar k^2 s_0 \frac{\mu' B_0}{\hbar k} \frac{(2\delta_0/\Gamma)}{[1 + (2\delta_0/\Gamma)^2]^2} z \tag{4.13}$$

$$\equiv -\alpha v - \kappa z, \tag{4.14}$$

where $|\mu' B_0 z/\hbar| \ll \Gamma$ has been assumed in addition to the small velocity approximation $kv \ll \Gamma$ in order to linearize around small (v, z) in (4.13). This force describes a damped harmonic oscillator and indicates that atoms inside the MOT perform damped harmonic oscillations around the center of the trap with spring constant κ and damping coefficient α. They are related by

$$\kappa = \frac{\mu' B_0}{\hbar k} \alpha. \tag{4.15}$$

Typical values for ^{88}Sr yield oscillation frequencies of $\sqrt{\kappa/m} \sim 10^4\,\mathrm{Hz}$ and damping rates of $\alpha/m \sim 10^5\,\mathrm{s}^{-1}$, indicating a strongly overdamped motion, where the atoms are effectively pushed towards the trap center.

Extending this principle to three dimensions requires three orthogonal pairs of beams. Two coaxial coils in the anti-Helmholtz configuration produce a spherical quadrupole field, which to first order provide the required uniform field gradient close to the center. Denoting the symmetry axis by z, Maxwell's law $\nabla \cdot \mathbf{B} = 0$ along with the cylindrical symmetry of the field yields

$$\frac{\partial B_x(x,0,0)}{\partial x} = \frac{\partial B_y(0,y,0)}{\partial y} = -\frac{1}{2} \frac{\partial B_z(0,0,z)}{\partial z}, \tag{4.16}$$

[1] These considerations apply equally well for any $J \to J' = J + 1$ optical transition

i.e. the radial spring constant is reduced to half its axial value, resulting in an elongated atomic cloud.

The strong dipole-allowed transition $|^1S_0\rangle \rightarrow |^1P_1\rangle$ at 461 nm used for deceleration is also used to trap the atoms. The trapping beams typically carry a total power of 30 mW and are detuned from resonance by $\delta_0/2\pi = -40$ MHz, which maximizes the trap population [44]. This is not a perfect two-level system, since there is a small decay channel to $|^1D_2\rangle$ as illustrated in figure 4.1. From here the atoms decay towards $|^3P_1\rangle$ and the metastable dark state $|^3P_2\rangle$ with branching ratios 66.7 % and 33.3 %, respectively. Atoms in the former state decay to the ground state. However, in order to ensure that the trap lifetime is not solely constrained by shelving, atoms in $|^3P_2\rangle$ with a 520 s lifetime [45] need to be recycled. This requires a repumper at 707 nm, which excites the atoms into $|^3S_1\rangle$ after which they quickly decay to $|^3P_1\rangle$ and $|^3P_0\rangle$ and finally the ground state through the strong intercombination line $|^3P_1\rangle \rightarrow |^1S_0\rangle$. A 679 nm laser can be employed to prevent repumping leaks due to $|^3S_1\rangle \rightarrow |^3P_0\rangle$.

The use of repumpers will extend both the population and the trap lifetime and thus the timescales on which a measurable signal is available. Note that due to the small branching ratio $1.95 \cdot 10^{-3}$ % of $|^1P_1\rangle$ to $|^1S_0\rangle$, shelving losses did not pose a problem during the relatively quick Zeeman-slowing.

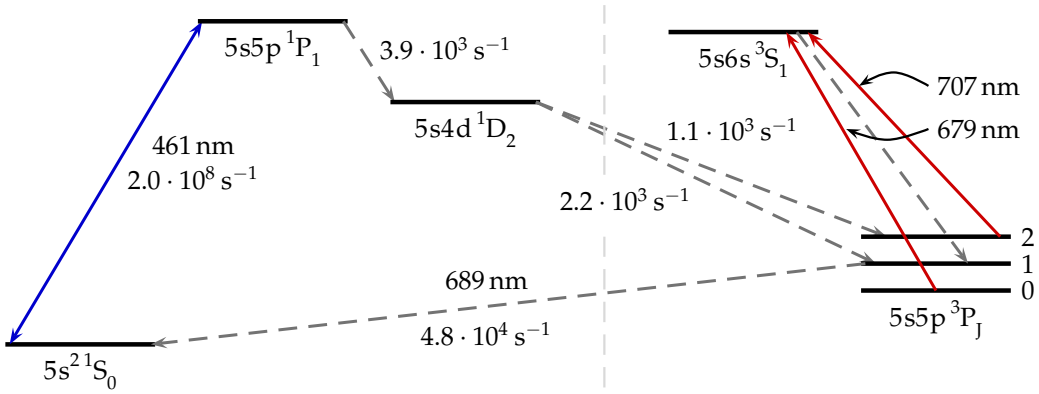

Figure 4.1: A schematic of the partial electronic structure of Sr also showing the radiative decay channels and A-coefficients [46]. The repumpers at 679 nm and 707 nm are also shown. Dashed lines denote decay paths. Note that energies are not to scale.

4.2.1 Capture Range and Velocity

A three-dimensional MOT will only capture the atoms that are slow enough to be decelerated inside its spatial extent, which are then pushed back towards the center. The trap radius R_c is determined by the radius of the trapping beams, which defines the region in which atoms see an effective red detuning of the trapping light. The field gradient B_0 is then estimated through the position at which zero-velocity atoms are in resonance with one of the laser beams, i.e.

$$B_0 \approx \frac{\hbar \delta_0}{\mu' R_c}. \tag{4.17}$$

The beam radius 8 mm is used in the experiment, corresponding to a gradient of roughly 35 G/cm. This is readily achieved with two anti-Helmholtz coils.

The trap population increases with the gradient given modest values < 100 G/cm, since the trap depth κ in (4.15) is increased. Beyond ~ 100 G/cm the maximum (resonant) value of

the light force is already achieved within the trap, and a further increase in the gradient will only shorten the deceleration distance and thus reduce the recapture ability, manifesting itself in a higher collisional loss rate [47].

As in the case with optical molasses, it is possible to define a capture velocity v_c as the maximum velocity for which atoms entering the trap region are slowed down and confined. A rough estimate is obtained by defining v_c such that atoms entering the trap with velocity v_c should come to a complete stop after traversing the trap radius R_c, i.e.

$$v_c^2 = 2R_c a_{\text{eff}}, \tag{4.18}$$

where $a_{\text{eff}} < a_{\text{max}}$ is the effective deceleration experienced by the atoms. A lower bound on a_{eff} can be estimated as $a_{\text{max}} s_0/(1+s_0)$, since it takes into account the dependency on the beam intensity. With an estimated 5 mW per beam the capture velocity is

$$v_c = \sqrt{\frac{\hbar k \Gamma}{2m} \frac{s_0}{1+s_0} R_c} \tag{4.19}$$

$$\simeq 26\,\text{m/s}, \tag{4.20}$$

which is a typical value. Generally, the capture velocity increases with power since the trap depth is increased, but eventually decreases as the cooling transition becomes power broadened. In this limit the counter-propagating radiative forces become indistinguishable, thus reducing the frictional force [48]. Since the trap population for a constant volume is determined by v_c and losses, the population decreases beyond this point.

4.2.2 Trapping Light

Having established the principle behind a MOT, it is in order to review the generation of the 461 nm trapping beams. The 461 nm light derives from continuous-wave second harmonic generation by an AR-coated quasi phase-matched KTP crystal. The fundamental wavelength 922 nm is supplied by an ECDL in the Littrow configuration, the master laser. As the frequency-doubled power scales with the square of the incident power, the 922 nm light is amplified by a tapered amplifier to about 1 W after which it is coupled into a bow-tie cavity consisting of highly reflecting (transmitting) mirrors at 922 nm (461 nm). A mode-matched input yields $\sim$100 mW.

Efficient frequency-doubling requires that the resonance condition of the fundamental beam with respect to the bow-tie cavity is satisfied. In order to minimize the effects of acoustic noise and frequency fluctuations in the incident beam, the Hänsch-Couillaud lock has at an earlier stage been employed to control the cavity length [49]. The lock bandwidth is limited by the first mechanical resonance of the combined piezo-mirror system in the bow-tie cavity, occuring at a few tens of kHz.

4.2.3 Stabilization

Since the number of trapped atoms depend critically on frequency, it is necessary to reference the trapping light against the $\left|{}^1\text{S}_0\right\rangle \rightarrow \left|{}^1\text{P}_1\right\rangle$ transition of ^{88}Sr. This is accomplished by modulating the laser frequency harmonically at $\Omega = 9.1\,\text{kHz} \ll \Gamma$ with depth δ by sending it through an AOM. The first-order diffracted beam then intersects the atoms effusing from an oven transversely in order to minimize the Doppler effect, while the signal is picked up by a photomultiplier. Assuming a low drift of the center frequency ω, the laser frequency is given

by $\omega_l = \omega + \delta \sin(\Omega t)$. Expanding the measured intensity $I_M(\omega_l)$ and collecting terms yields

$$\begin{aligned} I_M(\omega_l) = \mathrm{DC} &+ \sin(\Omega t)\left(\delta \frac{dI_M}{d\omega_l} + \frac{\delta^3}{6}\sin^2(\Omega t)\frac{d^3 I_M}{d{\omega_l}^3} + \dots\right) \\ &+ \cos(2\Omega t)\left(-\frac{\delta^2}{4}\frac{d^2 I_M}{d{\omega_l}^2} + \dots\right) \\ &+ \dots . \end{aligned} \tag{4.21}$$

Performing phase-sensitive detection at Ω will thus extract the first-order derivative of I_M, assuming a sufficiently small modulation depth $\delta \ll \omega_0$. This is accomplished by feeding the detected signal to a lock-in amplifier, whose output V_O is proportional to the frequency decomposition at Ω of the incoming signal V_I

$$V_O \propto G \int_0^T \sin(\Omega t + \phi) V_I(t)\, dt, \tag{4.22}$$

where T is the integration time of the low-pass filter ($T \gg \Omega^{-1}$), G the gain and ϕ a variable phase shift. The detected signal and corresponding lock-in derivative is shown in figure 4.2. The dashed vertical lines show the nearest isotopes relative to ^{88}Sr, specifically ^{86}Sr at -124.8 MHz and ^{87}Sr $(F = 9/2, F = 11/2, F = 7/2) = (-69, -51.8, -9.7)$ MHz [50]. These known values have been used to calibrate the frequency axis.

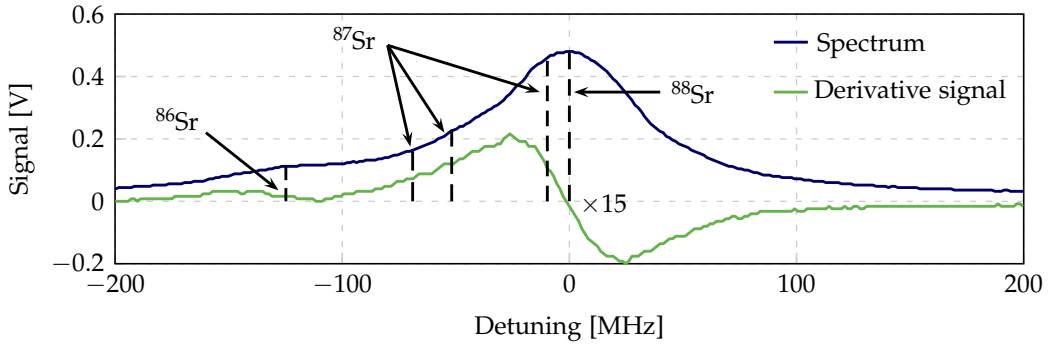

Figure 4.2: Spectrum from orthogonal crossed-beam spectroscopy of an atomic beam line when scanning across $|{}^1S_0\rangle \rightarrow |{}^1P_1\rangle$ of Sr. Also shown is the corresponding derivative signal as a function of ^{88}Sr-detuning.

The lock-in signal yields a most useful error signal readily fed to a PID-controller constituting the servo. Its output is used to modulate a high-voltage amplifier controlling the master laser piezo-mounted grating, thus closing the loop. The relatively weak flourescence prevents locking to third and higher (odd) orders. This could otherwise reduce the Doppler background, yielding a more precise lock since the signal close to resonance is narrower, but this would also result in a smaller recapture range. The SNR is optimized by adjusting the direction of the incident linear polarization and by carefully retro-reflecting the beam as any misalignment will broaden the signal width. The stability of the lock is characterized in the next section.

A schematic of the setup is shown in figure 4.3. The modulation is generated by the lock-in amplifier itself, which is sent to a sum amplifier (SA) such that a DC signal can be added to it. This enables the possibility to offset-lock to the resonance. The combined signal is sent to the voltage-controlled oscillator (VCO) driving the AOM.

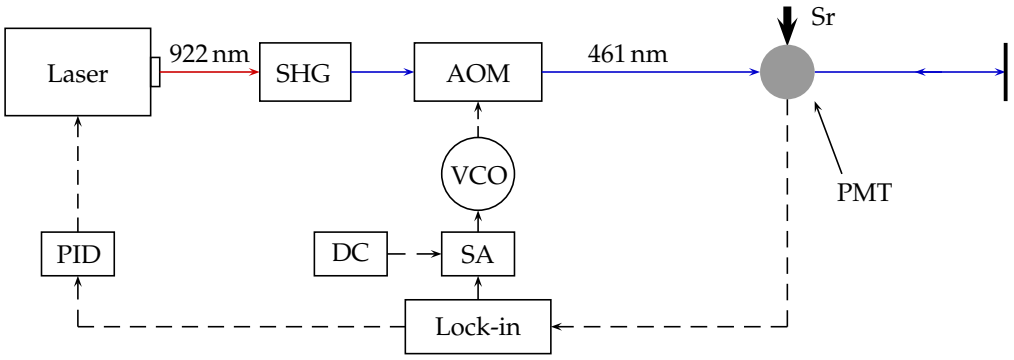

Figure 4.3: Schematic diagram of the locking system for the 461 nm laser. The VCO (voltage-controlled oscillator) driving the AOM is fed a signal from the sum-amplifier (SA). The signal provided by the SA is a constant DC-voltage added to the harmonically varying signal generated by the lock-in amplifier. The flourescence is picked up by a photomultiplier tube (PMT).

Generally, the spectrum from effusing atoms is a convolution between the thermally-broadened Gaussian profile and a Lorentzian associated with the natural linewidth. This is known as a Voigt function, represented as

$$S_V(x,y) = \frac{y}{\pi}\int_{-\infty}^{\infty} \frac{e^{-u^2}}{y^2+(x-u)^2}\,du, \tag{4.23}$$

where $x = \sqrt{\ln 2}(\nu-\nu_0)/\alpha_G$ and $y = \sqrt{\ln 2}\alpha_L/\alpha_G$. Here ν_0 denotes the transition frequency and α_L (α_G) the Lorentzian (Gaussian) HWHM.

Through nonlinear least squares fitting the FWHM of the ^{88}Sr-signal can be extracted, where the total spectrum is represented as the sum of five Voigt profiles, one for each isotope and hyperfine component. Using the known values for the linewidth, relative abundances, relative transition frequencies and hyperfine splittings [50], only three degrees of freedom are left, namely an overall amplitude, signal background and Gaussian HWHM. Note that as (4.23) is not available in closed form, the rapidly converging approximation [51] is used instead. The resulting profile is shown in figure 4.4, yielding the total FWHM $= (78.8 \pm 0.3)$ MHz for ^{88}Sr.

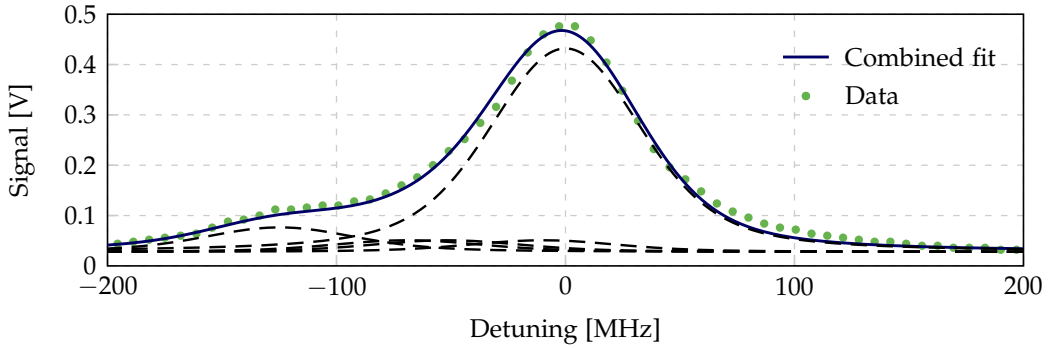

Figure 4.4: Experimental spectrum of the Sr transition $|^1S_0\rangle \rightarrow |^1P_1\rangle$ (green dots) with the associated fit (blue line), consisting of five Voigt profiles (dashed, black lines). The adjusted R^2 of the fit is 0.994.

From the Gaussian FWHM $\Delta_G = (59.9 \pm 0.3)\,\mathrm{MHz}$ the transverse velocity HWHM $\sigma_\perp$ is estimated as $\sigma_\perp = \Delta_G \lambda/2 \simeq 14\,\mathrm{m/s}$. It should be noted that this estimate implicitly assumes that other broadening mechanism are negligible, but since the transit-time broadening $\Delta\nu_{tt} \sim$ kHz is much smaller than Γ and power saturation effects are negligible $(I/I_{\mathrm{sat}} \ll 1)$, this is a decent assumption.

An overview of the final trapping setup is shown in figure 4.5. A number of different frequencies are required for both cooling and trapping, which are generated by three AOMs that additionally serve as power controls and fast light switches.

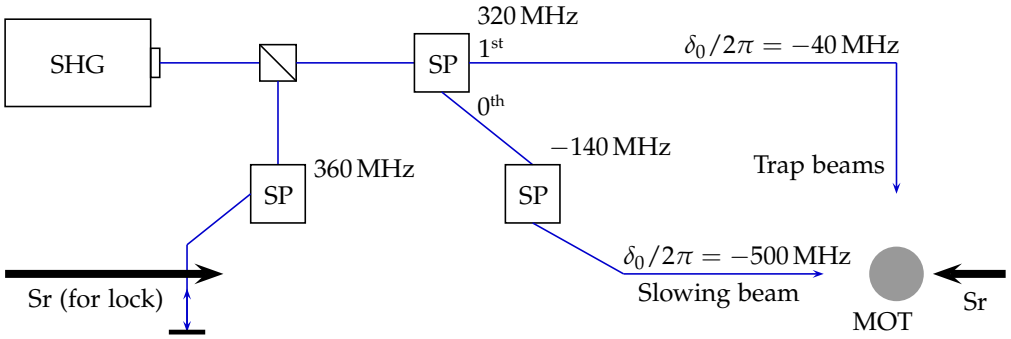

Figure 4.5: Setup used for magneto-optical trapping of ^{88}Sr using the $|^1S_0\rangle \rightarrow |^1P_1\rangle$ transition, 461 nm. For each AOM it is indiciated that it is operating in single pass (SP) configuration.

4.2.4 Characterizing the Lock

We utilize the Allan variance to characterize the stability provided by the lock, specifically the two-sample deviation over the integration time τ with zero dead-time

$$\sigma_y^2(\tau) = \frac{1}{2}\left\langle (\overline{y}_{k+1} - \overline{y}_k)^2 \right\rangle, \tag{4.24}$$

where $\overline{y}_k$ denotes the frequency fluctuations sampled over τ for the kth measurement cycle

$$\overline{y}_k = \frac{1}{\tau}\int_{t_k}^{t_k+\tau} y(t)\,dt. \tag{4.25}$$

From (4.24) it is possible to infer what type and level of noise is present in the system. Oscillator data is often nonstationary due to time dependent noise. For this reason the classical standard deviation does not converge to a particular value, as it would for stationary data [52]. Herein lies the usefulness of (4.24), since it basically differences successive data points.

The Allan deviation $\sigma_y(\tau)$ of the residual in-loop error signal is shown in figure 4.6. It is dominated by a $\tau^{-1/2}$ behavior for slow time scales $\tau \gtrsim 20\,\mathrm{ms}$, a signature of the stationary white noise contributed by the continuously interrogated atoms. The instability is ultimately limited by the shot-noise of both the signal as well as the atomic beam in addition to nonstationary electronic noise in the circuit and temperature fluctuations of the oven.

The lock is satisfactory when the trapping light is stable over time scales longer than the typical MOT lifetime $\sim 50\,\mathrm{ms}$. Specifically, the Allan deviation is found to be $(20 \pm 2)\,\mathrm{kHz}$ at 50 ms, which is much smaller than Γ so the lock is sufficient. In principle the error signal can be derived from a Doppler-free signal by going beyond the linear regime and thereby locking

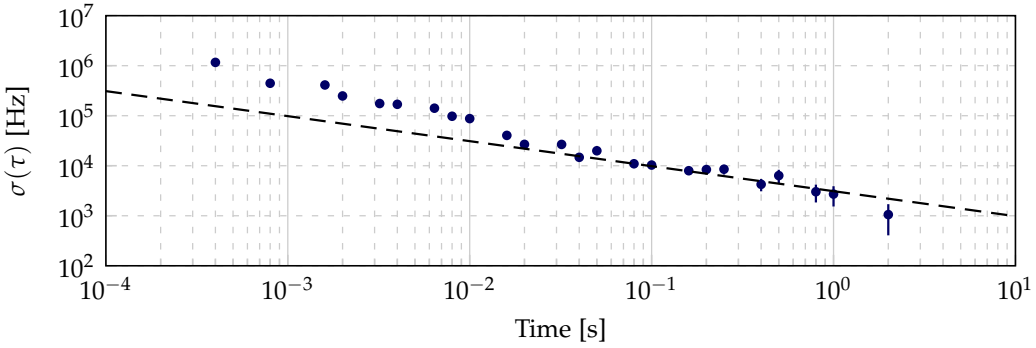

Figure 4.6: The Allan deviation of the residual error signal of the stabilized 461 nm-light. As the integration time is increased, the instability of the carrier frequency decreases due to the nature of the white noise in the system. The dashed line is proportional to $\tau^{-1/2}$. The bump occuring at fast time scales is due to overcompensation by the servo loop as its bandwidth is not sufficiently wide to account for mechanical vibrations at these time scales. The relative standard deviation on $\sigma(\tau)$ is estimated as $0.87/\sqrt{N}$, where N is the number of cycles at time τ [53].

to the Lamb dip. The currently achieved short-term instability is, however, more than sufficient for the MOT to function properly even though it is an underestimation due to the measurement being in-loop. During operation the performance of the lock is limited by the SNR, but the signal is generally sufficient when operating the oven at $T = 450\,^{\circ}\mathrm{C}$.

4.3 Trap Dynamics

With the trapping light stabilized, the MOT is now operational. In the following the trap dynamics will be discussed, which will enable characterizing the trap in terms of atomic population and loss rate. The loss rate is investigated in depth, which is necessary for subsequent optimization.

The steady-state of a continuously operated MOT is a dynamic equilibrium: The number of trapped atoms N is a balance between various loss channels and the rate at which new atoms are captured. There are three different contributions to the rate equation: The loading rate L of capturable atoms, one- and two-body losses, characterized by the rates α and β, respectively. Higher-order losses become important at atomic densities much higher than those currently attainable in our setup. The behaviour of the atomic cloud can thus be described by the time-dependent phenomenological expression

$$\dot{N} = L - \alpha N - \beta N^2. \tag{4.26}$$

The atoms in the trap are often treated as being Gaussianly distributed. This assumption is based on the steady-state solution to the Fokker-Planck equation for Brownian motion in an external harmonic potential, equivalent to the Langevin equation (4.4) including spatial confinement [54]. This assumption breaks down when the optical trap depth is much greater than 1, in which case the distribution is practically uniform due to reabsorption of spontaneously emitted photons [55]. However, for the present system it will be valid since sub-Doppler cooling is not present and consequently the temperature and occupied volume is larger than in, e.g., alkali-metal traps.

The one-body loss rate per atom α contains three terms: Collisions with thermal background atoms/molecules with rate α_B, collisions with the thermal loading beam with rate

α_L and shelving losses α_S. Ignoring the velocity of the cold atoms relative to the thermal background and assuming every constituent i of the background (BG) atmosphere contributes linearly to the loss rate, α_B is given by

$$\alpha_B = \sum_i n_{\mathrm{BG},i}\, \sigma_{\mathrm{Sr-BG},i}\, \sqrt{\langle v_i^2 \rangle}. \tag{4.27}$$

Here $\sigma_{\text{Sr-BG},i}$ is the collisional cross section, which is assumed to be independent of the collision velocity. Since the loss rate scales with the background density, a dense MOT requires optimal vacuum conditions in addition to elimination of shelving losses.

The latter term in (4.26) accounts for two-body losses. These are due to inelastic collisions between trapped atoms by which internal energy is converted to kinetic energy. At least one atom per collision acquires enough energy to be ejected from the trap.

4.3.1 Loading Rate and One-Body Losses

For relatively small trap sizes $\simeq 20 \cdot 10^6$ atoms, $N(t)$ is well described by neglegting two-body losses resulting in the loading behavior

$$N(t) = N_{\max}\left(1 - e^{-\alpha t}\right), \tag{4.28}$$

with $N_{\max} = L/\alpha$. This is readily measured by observing the emitted power P during load of the trap, which is related to the number of atoms N by

$$N = \frac{P}{\hbar\omega}\frac{\tau}{\rho_{AA}}\frac{1}{\Omega\eta}, \tag{4.29}$$

where Ω is the solid angle from which the light is collected, τ the lifetime of the excited $\left|{}^1\mathrm{P}_1\right\rangle$ trapping state, $\eta = 0.96^2$ the fraction of transmitted light and $\rho_{AA} \equiv \rho_{ee,t\to\infty}$ the excited trapping state probability. From the loading curve in figure 4.7 it is found that $L = (2.56 \pm 0.09) \cdot 10^9$ atoms/s at the oven temperature 530 °C, smaller than the predicted value $\mathcal{L} \simeq 9.9 \cdot 10^{10}$ atoms/s in (3.33). This was also expected, since the estimate did not take into account transverse heating. The measured value is in good correpondence with a similar system [32].

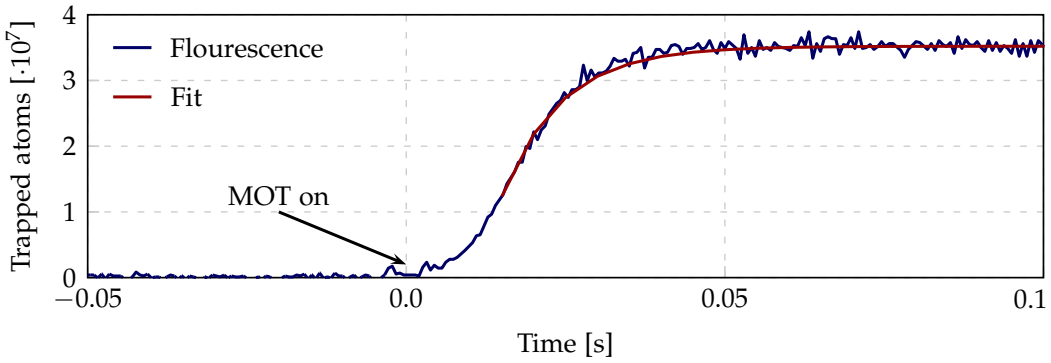

Figure 4.7: The loading of atoms in the MOT (blue line) and the corresponding fit to (4.28) (red line). Each trapping beam carries roughly 5 mW/cm^2.

As was explained in relation to the level diagram in figure 4.1, the one-body loss rate is determined by leaks into the metastable triplet state $\left|{}^3\mathrm{P}_2\right\rangle$ and hence we can already state that

it must depend on the scattering rate. We quantify this statement further by looking at the dynamics of the trap, which is governed by

$$\dot{N}_0 = L + \Gamma_{10} N_1 - \rho_{AA}\Gamma_{12} N_0 - \alpha_T N_0 \tag{4.30}$$

$$\dot{N}_1 = \Gamma_{21} N_2 - \Gamma_{10} N_1 - \alpha_T N_1 \tag{4.31}$$

$$\dot{N}_2 = \rho_{AA}\Gamma_{12} N_0 - (\Gamma_{21} + \Gamma_{22}) N_2 - \alpha_T N_2, \tag{4.32}$$

where $\{N_0, N_1, N_2\}$ are the number of atoms in the atomic states $\{{}^1\mathrm{S}_0, {}^3\mathrm{P}_1, {}^1\mathrm{D}_2\}$, α_T accounts for thermal losses including both α_B and α_L and the decay rates $\{\Gamma_{10}, \Gamma_{12}, \Gamma_{21}, \Gamma_{22}\}$ denote $\{\Gamma_{{}^3\mathrm{P}_1 \to {}^1\mathrm{S}_0}, \Gamma_{{}^1\mathrm{P}_1 \to {}^1\mathrm{D}_2}, \Gamma_{{}^1\mathrm{D}_2 \to {}^3\mathrm{P}_1}, \Gamma_{{}^1\mathrm{D}_2 \to {}^3\mathrm{P}_2}\}$. In order to simplify the expressions the main transition has been assumed to be a two-level system in steady-state, which is reasonable due to the small leakage-probability per event. A further simplification can be carried out by adiabatically eliminating $\dot{N}_1$ since $\Gamma_{10} > \Gamma_{12}$. The trap population is detemined by atoms residing in N_0, so the loss rate α is readily found by Laplace transforming (4.30)-(4.32) and then solving for $N_0(t)$. This yields two analytical solutions of the form (4.28), each having its own rate α, which are given by

$$\begin{aligned}\alpha = \frac{1}{2}\alpha_T + \frac{1}{2}(\Gamma_{21} + \Gamma_{22} + \Gamma_{12}\rho_{AA}) \\ \pm \frac{1}{2}\sqrt{(\alpha_T + \Gamma_{21} + \Gamma_{22} + \Gamma_{12}\rho_{AA})^2 - 4(\alpha_T\Gamma_{21} + \alpha_T\Gamma_{22} + \Gamma_{12}\Gamma_{22}\rho_{AA})}.\end{aligned} \tag{4.33}$$

The positive solution is more than three orders of magnitude larger than the negative, and the positive solution can thus be neglegted. The loading time in figure 4.7 is then given by the remaining "slow" timescale, which can be expanded to

$$\alpha \simeq \frac{1}{2}\alpha_T + \frac{\Gamma_{22}}{\Gamma_{21} + \Gamma_{22}}\Gamma_{12}\rho_{AA} \tag{4.34}$$

$$\equiv \frac{1}{2}\alpha_T + B_{22}\Gamma_{12}\rho_{AA}, \tag{4.35}$$

where the branching ratio $B_{22} = 0.33$ for $\left|{}^1\mathrm{D}_2\right\rangle \to \left|{}^3\mathrm{P}_2\right\rangle$ has been introduced. The loss rate indeed depends on the trapping intensity through ρ_{AA} as we anticipated. Neglegting α_T, this expression is identical to the one derived in [56] by a more pragmatic approach: By realizing that the decay to $\left|{}^1\mathrm{D}_2\right\rangle$ basically constitutes the trap losses at this stage, α must be given by $B_{22}\Gamma_{12}\rho_{AA}$ when $\left|{}^1\mathrm{D}_2\right\rangle$ is in steady state.

One channel has been neglegted so far, which is the loss due to $\left|{}^1\mathrm{D}_2\right\rangle$-atoms leaving the trapping area before decaying back to $\left|{}^1\mathrm{S}_0\right\rangle$. This is readily taken into account by the factor

$$\chi = \zeta \int_0^\infty f(v) e^{-R/v\tau}\, dv \tag{4.36}$$

$$= 4\pi\zeta \left(\frac{m}{2\pi k_B T}\right)^{3/2} \int_0^\infty v^2 e^{-mv^2/2k_BT} e^{-R/v\tau}\, dv, \tag{4.37}$$

where R is the trap radius and τ the lifetime of $\left|{}^1\mathrm{D}_2\right\rangle$. It is reasonable to assume that atoms can only escape between trapping beams, due to which the ratio is weighted by $\zeta = 1 - [6 \times 2\pi(1 - \cos\theta)]/4\pi$. Assuming a spherical trap, the term $6 \times 2\pi(1 - \cos\theta)$ is the solid angle subtended by all six beams, where 2θ is the full apex of the cone inside the sphere, which represents the area a single beam traces out. Taking $\theta = \pi/2$ ($\zeta = 0.12$) and a temperature of 5 mK yields $\chi = 2 \cdot 10^{-4}$ and thus it is neglegted in the following. It could otherwise be included by generalizing $\Gamma_{21}N_2$ to $(1 - \chi)\Gamma_{21}N_2$.

By utilizing (4.28) the loss rate has been measured for various trapping powers, shown in figure 4.8. The value $\Gamma_{12} = (4.15 \pm 0.13) \cdot 10^3\,\mathrm{s}^{-1}$ is obtained by a nonlinear least squares fit using (4.33), where Γ_{21} and Γ_{22} are assumed known. This is within the expected $(3.85 \pm 1.47) \cdot 10^3\,\mathrm{s}^{-1}$ [57], but our result is of limited value since it is based on the laser intensity. This can pose a problem if the beam possesses structure. The associated thermal loss is $(7.62 \pm 4.85)\,\mathrm{s}^{-1}$ for an oven temperature 530 °C.

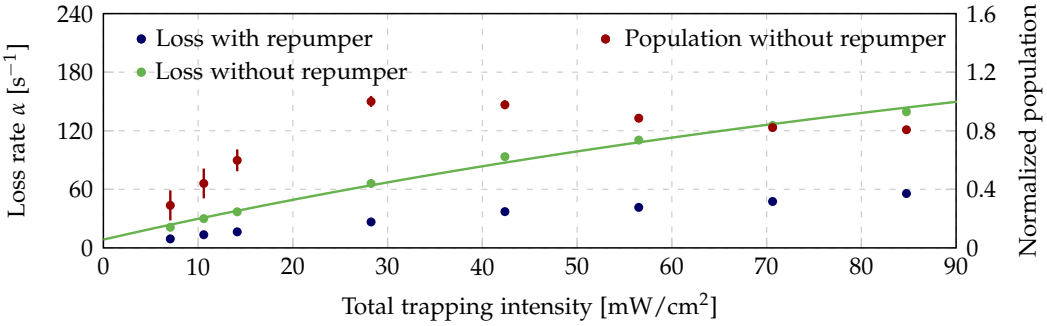

Figure 4.8: The one-body loss rate as a function of total trapping intensity (left side). The solid line is a weighted nonlinear least squares fit to (4.33). The corresponding trap population is shown to the right for the case where the repumper is not applied, normalized to its largest value. Uncertainties for most data points are smaller than the dot size.

The population as a function of trapping intensity conforms with the presented theory, in addition to the results obtained by [58], i.e. it decreases when the transition starts to saturate.

The 707 nm laser is a standard ECDL, mounted in the Littrow configuration. Its effect is clearly seen on the measurements, where it decreases the loss rate by a factor 2.5 on average, in reasonable correspondence with the factor of three usually obtained [46, 59]. This value should ideally be the same for all our measurements, since the gain only depends on how efficiently the atoms are pumped out of the dark state. Since the repumper in the current experiment is free-running, it was necessary to tune it into resonance prior to each measurement, which may have resulted in minor inconsistencies. The frequency should ideally have been modulated by application of a sawtooth waveform to the piezo transducer, where the amplitude of modulation frequency could easily have been chosen by empirically optimizing the trap size. The effect of the repumper on the cloud dynamics is investigated in the next section.

The repumper does not alter the loading rate, so a given decrease in the loss rate α translates into a corresponding increase in the number of trapped atoms.

4.3.2 Including the Repumper

Having succesfully implemented the 707 nm repumper and verified its effect, we now wish to take its effect on the atomic dynamics into account by extending the rate equations.

The repumper is switched on at $t = t_0$, which we describe by the step-function $\theta(t - t_0)$. The rate equations then become

$$\dot{N}_0 = L + \Gamma_{10}N_1 - \rho_{AA}\Gamma_{12}N_0 - \alpha_T N_0 \tag{4.38}$$

$$\dot{N}_1 = \Gamma_{21}N_2 + \Gamma_{41}N_4 - \Gamma_{10}N_1 - \alpha_T N_1 \tag{4.39}$$

$$\dot{N}_2 = \rho_{AA}\Gamma_{12}N_0 - (\Gamma_{21} + \Gamma_{22})N_2 - \alpha_T N_2 \tag{4.40}$$

$$\dot{N}_3 = \Pi(t - t_0)\Gamma_{22}N_2 - \theta(t - t_0)[R_{707}(N_3 - N_4) - \Gamma_{43}N_4] - \alpha_T N_3 \tag{4.41}$$

$$\dot{N}_4 = \theta(t - t_0)[R_{707}(N_3 - N_4)] - N_4(\Gamma_{40} + \Gamma_{41} + \Gamma_{43}) - \alpha_T N_4, \tag{4.42}$$

where $\{N_0, N_1, N_2, N_3, N_4\}$ are the number of atoms in the states $\{{}^1S_0, {}^3P_1, {}^1D_2, {}^3P_2, {}^3S_1\}$. The driving rate R_{707} is given by $\rho B_{43} S(\nu)$ with the Einstein B-coefficient B_{43}, radiation density $\rho = I/c$ and Lorentzian profile $S(\nu)$. The decay rates are denoted according to $\{\Gamma_{40}, \Gamma_{41}, \Gamma_{43}\} = \{\Gamma_{{}^3S_1 \to {}^3P_0}, \Gamma_{{}^3S_1 \to {}^3P_1}, \Gamma_{{}^3S_1 \to {}^3P_2}\} = \{9.0 \cdot 10^6\,\mathrm{s}^{-1}, 2.8 \cdot 10^7\,\mathrm{s}^{-1}, 4.6 \cdot 10^7\,\mathrm{s}^{-1}\}$ [44].

The function $\Pi(t - t_0)$ occuring in (4.41) is defined as $\Pi(t - t_0) = 0.4[1 - \theta(t - t_0)] + \theta(t - t_0)$. This factor of 0.4 needs to be taken into account for times $t < t_0$, since only the two weak-field seeking substates $m_J = \{1, 2\}$ of $|{}^3P_2\rangle$ are confined in the magnetic trap when the repumper is not applied. Since $g_J m_J > 0$, only they are able to minimize the quantum mechanical interaction energy $U = \mu_B g_J m_J B$ originating from the interaction between their magnetic dipole and the quadropole field B. In contrast, the strong-field seeking substates $m_J = \{-1, -2\}$ ($g_J m_J < 0$) are repelled from the trap, since static field maxima in free space are not permitted by Maxwell's equations [60]. After applying the repumper, $t > t_0$, all five substates of $|{}^3P_2\rangle$ will be excited to $|{}^3S_1\rangle$.

Neglecting thermal losses as a first approximation, the increase in steady-state trap population after applying the repumper is analytically given by $1 + \Gamma_{43}/\Gamma_{40} \simeq 4.11$. It is independent of R_{707}, since the repumper in this case connects $|{}^3P_2\rangle$ to $|{}^3S_1\rangle$. As the former is continuously loaded ($\alpha_T \to 0$), the population gain can only depend on the remaining loss channel Γ_{40}.

Conversely, the gain is found to depend on R_{707} when taking into account that $\alpha_T \approx 0.2\,\mathrm{s}^{-1}$. This is anticipated, since R_{707} determines the number of atoms coupled out of $|{}^3P_2\rangle$ whose steady-state value is now fixed by α_T. An analytical solution is possible, but it is not elucidating and consequently a numerical approach is taken in the following.

Figure 4.9 illustrates how the gain in trap population saturates when the intensity satisfies $R_{707} \sim B_{22}\Gamma_{12}\rho_{AA} \approx 59\,\mathrm{s}^{-1}$ ($\rho_{AA} \simeq 0.05$ with $5\,\mathrm{mW/cm^2}$ per trapping beam). The repumper

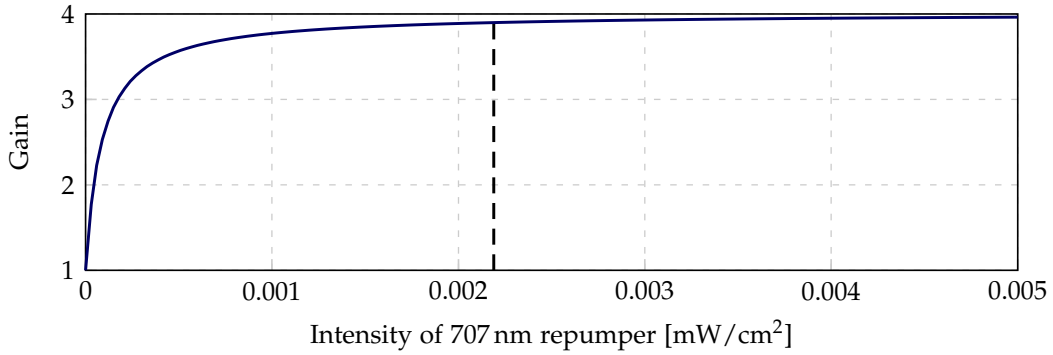

Figure 4.9: The steady-state gain in trap population as a function of 707 nm intensity. The dashed line $I = 0.0022\,\mathrm{mW/cm^2}$ corresponds to $R_{707} = B_{22}\Gamma_{12}\rho_{AA} \approx 59\,\mathrm{s}^{-1}$.

is assumed to be detuned by 50 MHz, estimated with an optical wavemeter. Atoms entering $|{}^3P_2\rangle$ are immediately transferred to $|{}^3S_1\rangle$ when the intensity is increased beyond $B_{22}\Gamma_{12}\rho_{AA}$, and the gain is only weakly intensity-dependent in this domain.

The transient behavior $N_0(t)$ is illustrated in figure 4.10 for different repumping-rates: Given that $N_0(t_0)/N_3(t_0) \lesssim 0.1$, when $R_{707} \gtrsim B_{22}\Gamma_{12}\rho_{AA}$ a transient overshoot occurs when turning on the repumper at t_0, since a large number of atoms on the order of $N_0(t = t_0)$ enters the trap during a very short time. Compared to other transients this happens almost instantly since Γ_{41} is the fastest timescale in the system. Conversely, the gain is gradual in the opposite limit $R_{707} < B_{22}\Gamma_{12}\rho_{AA}$. The load in this respect does not alter the gain as it merely acts as a scaling factor for the various level populations.

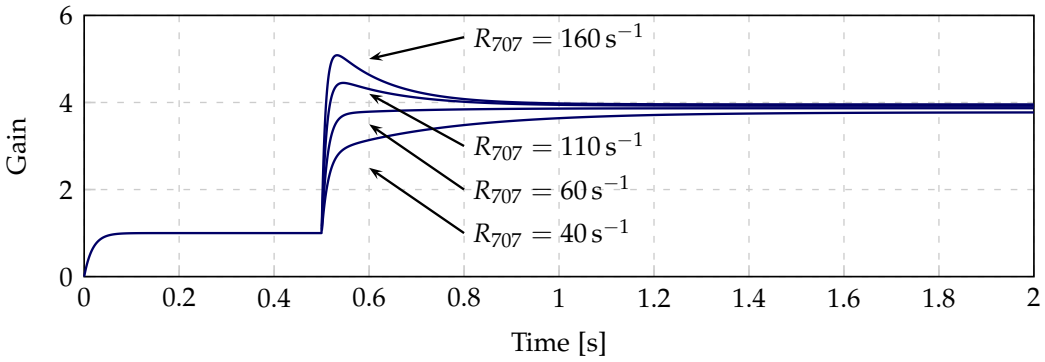

Figure 4.10: The transient behavior of $N_0(t)$ when turning on the MOT at $t = 0\,\mathrm{s}$ and applying the repumper at $t = 0.5\,\mathrm{s}$ for various repumping rates corresponding to (from top to bottom): $0.0065\,\mathrm{mW/cm^2}$, $0.004\,\mathrm{mW/cm^2}$, $0.0025\,\mathrm{mW/cm^2}$ and $0.0015\,\mathrm{mW/cm^2}$.

Figure 4.11 shows a comparison between the predicted and measured temporal behavior after switching on the repumper. Based on figure 4.9, at intensities on the order of $\mathrm{mW/cm^2}$ we would expect to be well within the domain of $R_{707} \gg B_{22}\Gamma_{12}\rho_{AA}$, which evidently is not the case experimentally.

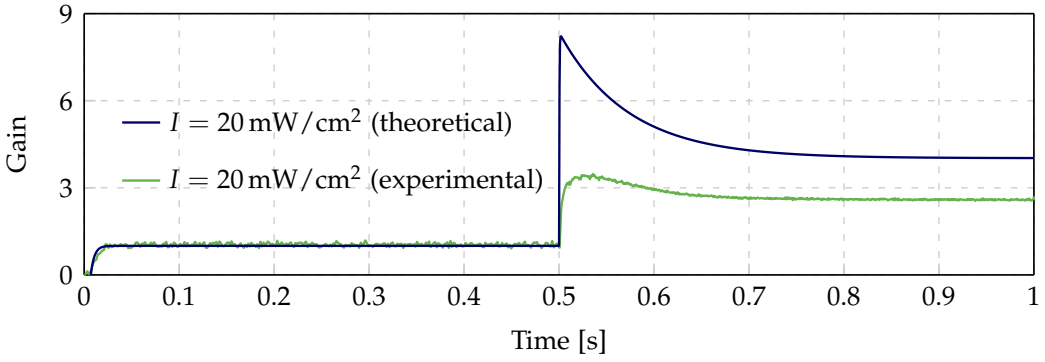

Figure 4.11: The measured transient behavior of the MOT-population after applying the 707 nm-repumper at $t_0 = 0.5\,\mathrm{s}$ containing $20\,\mathrm{mW/cm^2}$ ($R_{707} \approx 5.4 \cdot 10^5\,\mathrm{s}^{-1}$). Also shown is the expected behavior for $20\,\mathrm{mW/cm^2}$.

There are several possible explanations for this lack of compatibility:

- The optical-frequency PSD of the grating-stabilized 707 nm diode laser is not peaked around the $|^3\mathrm{P}_2\rangle \rightarrow |^3\mathrm{S}_1\rangle$ transition frequency, so the effective intensity in the required mode is most likely lower.
- The model implicitly assumes that all atoms are affected by the repumper, which is not necessarily the case. Geometrical misalignments between trap and repumper are possible, such that only a fraction of the $|^3\mathrm{P}_2\rangle$-atoms interact with the 707 nm laser at a given time. As an example, in [61] it is estimated that only 1 % of the atoms interact with the repumper. In the current setup, however, this effect is not believed to be a major issue.
- Improper trapping beam alignment will increase the cloud temperature and thus alter the atomic dynamics. The consequence of this enters through the quadropole field: The

repumper is linearly polarized so a rigorous analysis would have to properly take into account how often π- and σ-transitions are driven. This will as a minimum alter the steady-state population gain in figure 4.9 due to coupling to dark states. Specifically, $|^3P_2, m_J = \pm 2\rangle$ are dark states when π-transitions are driven.

Experimentally it is observed that the peak at $t = t_0$ varies with trapping beam alignment, suggesting that a proper treatment indeed requires taking into account the cloud dynamics. It is possible that the discrepancy of a factor of 1.5 between steady-state values in figure 4.11 is accounted for when solving the rate equations over the whole atomic cloud. In the case where the trap radius goes to zero, this extended treatment should yield the idealized model we have treated so far.

Besides dark states, the quadropole field will also decrease the rate R_{707} for a given intensity due to the varying Zeeman shift, which occurs for both π- and σ-transitions as the Landé factor is not the same for $|^3P_2\rangle$ and $|^3S_1\rangle$. In [61, 62] this is remedied by rescaling the intensity-dependency of R_{707} until there is a qualitative agreement with the data. This rudimentary treatment is too simple for our system as it does not yield a better correspondence.

In principle it is possible to extract the various decay rates by fitting (4.38)-(4.42) to the data. Given that the measurements are strongly sensitive to the trapping beam alignment, it does not seem feasible to extract values with an acceptable precision through this approach, even if the quadropole field is accounted for. The practical use of our model thus seems limited at this stage.

4.4 Summary

This chapter has described the work leading to a functioning ^{88}Sr-MOT, currently able to trap $\sim 10^7$ atoms. The one-body loss rate has been measured explicitly for various trapping intensities and agree quantitatively with the theory derived for this system. The analytical expressions reduce to already well-known decay descriptions for Sr, thereby corroborating the model.

The 707 nm repumper has been succesfully employed in the experiment, increasing the amount of trapped atoms by almost a factor of three after proper alignment, in good agreement with similar systems. The theoretical model has been extending to account for this perturbation, and there is an acceptable qualitative agreement with the measurements within the capabilities of the model. A full, quantitative understanding as a minimum requires extending the rate equations to account for the individual magnetic sublevels of $|^3S_1\rangle$, $|^3P_2\rangle$ and $|^3P_1\rangle$ and the varying transition strengths. These equations would when have to be solved over the Gaussianly distributed cloud in the quadropole field, thereby accounting for dark states and Zeeman shifts. Given that this solves the discrepancy, it is possible to extract the various decay rates by fitting the rate equations to a measured transient curve, such as the one in figure 4.11. This will require excellent agreement between the experimental cloud size and the one used in the model, which may render the method too crude for precise measurements.

Future work consist of employing the 679 nm repumper, which should increase the number of trapped atoms by a total factor of six [59], and even ten has been reported [46]. This should yield an atomic sample large enough to be able to see the anticipated signal in figure 2.9, thereby directly confirming the considerations in chapter 2. One way to gauge the number of trapped atoms is to look for two-body collisions, which should occur for $\gtrsim 10^8$ atoms [63]. This manifests itself it a load- and decay behavior, which is not strictly exponential, c.f. (4.26).

Before performing the spectroscopy it is also necessary to set up the low-finesse cavity around the trapped atoms, preferably mounting the mirrors directly onto the chamber in order

to utilize common-mode rejection.

This chapter concludes the experimental part of this thesis, which has been focused on achieving magneto-optical trapping of ^{88}Sr. Consequently, we will not deal with the ongoing experimental work towards performing nonlinear spectroscopy, but instead investigate the possibility of producing a high flux of cold atoms, suitable for continuous cavity-enhanced spectroscopy.

Chapter 5

Cold Atoms for Continuous Cavity-QED

The lifetime of localized atoms in an optical lattice is limited to a few seconds due to imperfect vacuum and technical fluctuations in the harmonic lattice potential due to noise in the laser creating the lattice. In the framework of cavity-enhanced nonlinear spectroscopy it is thus necessary to feed the system with atoms, e.g. by loading the lattice periodically. An alternative is to have a constant flux of cold atoms flow through the cavity, but this requires that the transit-time broadening is less than the FWHM of the interrogated transition. For $|{}^1S_0\rangle \rightarrow |{}^3P_1\rangle$ of ${}^{88}Sr$ and an interrogation $1/e^2$-waist diameter of 1 mm (all beam sizes reported in the following also refer to the $1/e^2$-waist diameter), velocities around 15 m/s result in a broadening of roughly 15 kHz. This is comparable to $\Gamma/2\pi = 7.6$ kHz such that the transition Q-factor is not degraded severely.

These velocities are readily produced by conventional methods, as explained in chapter 3. With (2.61) in mind a second requirement is that the atoms must have a velocity less than or at least comparable to $\Gamma/k = 0.52$ cm/s along the axis of interrogation. In order to investigate if it is possible to meet these requirements in theory, the Monte Carlo simulation introduced to describe atomic deceleration in the Zeeman slower has been extended to find the atomic trajectories for the apparatus proposed in figure 5.1.

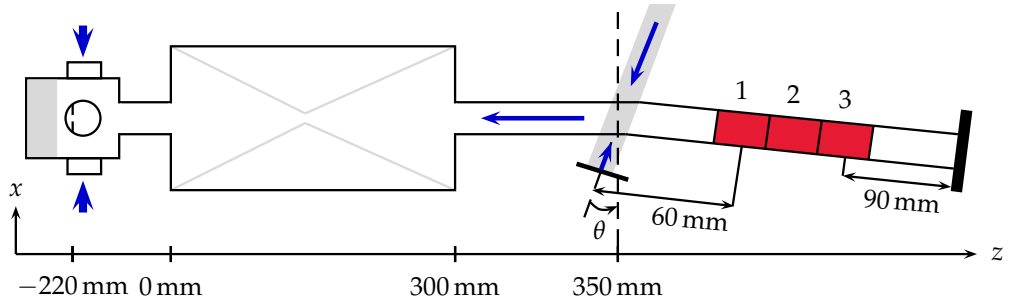

Figure 5.1: A proposal for a beamline potentially capable of producing a sufficient flux of cold atoms for continuous cavity-enhanced nonlinear spectroscopy, consisting of five separate stages: An initial 2D MOT after the atoms effuse from the oven, a Zeeman slower, a bend, a second 2D MOT stage for collimation and finally the cavity for spectroscopy. A blue (red) color refers to cooling using the transition $|{}^1S_0\rangle \rightarrow |{}^1P_1\rangle$ ($|{}^1S_0\rangle \rightarrow |{}^3P_1\rangle$).

5.1 Monoenergetic Cold Strontium Beam

The beamline is divided into the following three sections: The oven/Zeeman slower to produce a high flux of slow atoms, a deflection stage and the final 2D MOT stage for compression. The optical resonator is assumed to support a TEM_{00} mode with waist 1 mm and Rayleigh length at least a few cm. The three sections are separately investigated in the following in order to find the various parameters that maximize the number of interrogated atoms in the cavity, whose velocities satisfy the required criteria. We start by treating the section consisting of oven and Zeeman slower.

5.1.1 First Section: Oven and Zeeman Slower

The oven at temperature T has an aperture of area A and contains atoms of mass m at density n, which are assumed to be in thermal equilibrium. Given that the atomic mean free path is much greater than the aperture radius, atoms will effuse out without colliding with each other when a pressure gradient is present. This in turn implies that the equilibrium inside is undisrupted. The velocity distribution of the atoms contained in the solid angle corresponding to the opening aperture is then simply described by the standard 3D Maxwell-Boltzmann distribution $f_{\mathbf{v}} \propto \exp(-m(v_x^2 + v_y^2 + v_z^2)/2k_BT)$. Given that the walls of the oven are infinitely thin, the atomic spatial distribution along A is flat. The atomic velocity distributions reaching a second aperture A' a distance d away can then be found by numerically propagating N atoms from A to A'. The initial velocities are sampled from $f_{\mathbf{v}}$ and the initial positions chosen to lie randomly in A.

In this setup $d = 220\,\text{mm}$ and the radius of the circular aperture A (A') is 0.5 mm (8 mm). The speed distribution of $3.2 \cdot 10^3$ atoms reaching A' is shown in figure 5.2, where $N = 10^7$ atoms initially left the oven. It follows the 3D Boltzmann distribution $\propto v^2 \exp(-mv^2/2k_BT)$ as expected and fitting to the data yields an oven temperature $(514 \pm 13)\,°\text{C}$ in good correspondence with $T = 530\,°\text{C}$, which was used to generate the initial velocities. This oven temperature will be used in the following. Given the limited statistics, there is good agreement with the measured distribution.

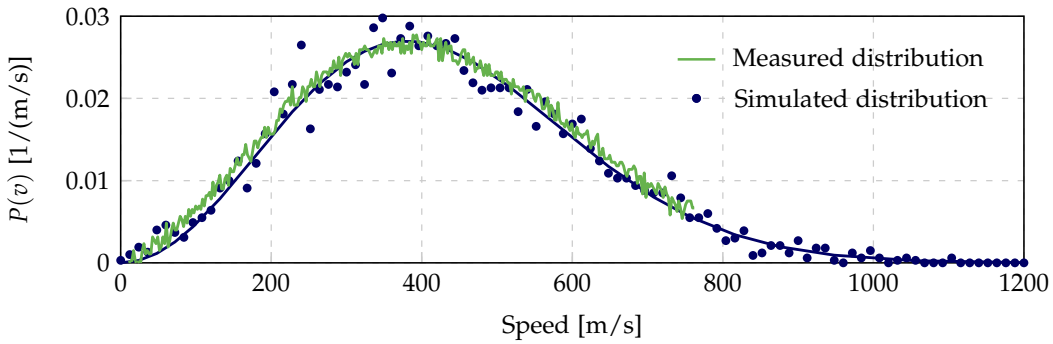

Figure 5.2: The simulated speed distribution of atoms reaching an aperture with radius 8 mm a distance $d = 220\,\text{mm}$ after the oven from which they effused out of (aperture with radius 0.5 mm). The solid blue curve is a fit to the 3D Boltzmann speed distribution. Also shown is an experimental measurement of the distribution, but the laser was not able to scan through the entire spectrum at the time of the measurement.

The individual velocity components of the atoms reaching A' are shown in figure 5.3. The axial component v_z is to a good approximation distributed according to $\propto v_z^2 \exp(-mv_z^2/2k_BT)$

as well, but with a smaller temperature $T \simeq 495\,^{\circ}\mathrm{C}$. This is also the anticipated behavior, since a usual transverse component is small in comparison. The transverse velocity components are normally distributed with mean $\approx 0\,\mathrm{m/s}$ and FWHM $= 18.6\,\mathrm{m/s}$, so the assumption utilized when modelling the slower in chapter 3 was not that poor.

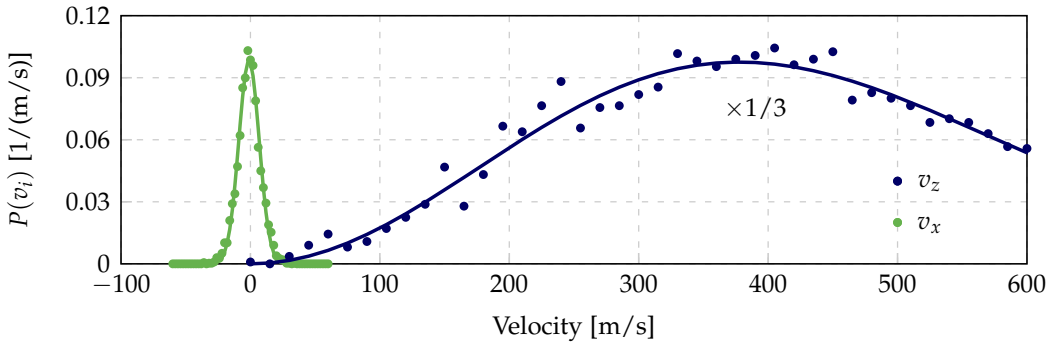

Figure 5.3: The simulated velocity components (v_x, v_z) of the atoms reaching A' and associated fits (solid curves). Only v_x is shown, but v_y follows similar statistics.

Ideally $> 10^5$ atoms should reach A' in order to obtain sufficient statistics, but this requires a large initial sample, at least 10^8 atoms. Since each trajectory must be integrated through Runge-Kutta methods, this large ensemble size requires an overwhelming computation time. We can circumvent this issue by utilizing the velocity distributions in figure 5.3 at the oven instead of the general $f_{\mathbf{v}}$. This ensures that the atoms that reach A' to a good approximation have velocities that obey the geometry defined by A, A' and d.

With the initial distributions in order, it is now possible to realistically send a single batch of N atoms through the system, out of which N' reach A' and $\varepsilon N'$ reach the cavity, $\varepsilon \ll 1$. We are, however, ultimately interested in the flux. This can be found by the relation (c.f. appendix C)

$$\Phi' = \frac{1}{4} n A \sqrt{\frac{8 k_B T}{\pi m}} \frac{A'}{A' + \pi d^2}, \tag{5.1}$$

which is the analytical expression for the flux of atoms that leave the oven through A and pass through A'. From this the number N' can be converted to flux, thus constituting the calibration in the model.

A 2D MOT performed on the $\left|{}^1\mathrm{S}_0\right\rangle \rightarrow \left|{}^1\mathrm{P}_1\right\rangle$ transition is employed after the oven to increase collimation. As shown in appendix B, four straight conducting wires arranged in a square configuration will produce a quadropole magnetic field inside the square, whose magnitude is determined by the current flowing through the wires. The gradient (B.5) is employed in the model, assuming a realistic distance $a = 10\,\mathrm{mm}$ between adjacent wires. This roughly corresponds to a gradient $0.4\,\mathrm{G/(cm\,A)}$. Figure 5.4 shows how this combination is able to focus the atoms in the extreme limit, where the cooling transition is highly saturated. Also shown is the random walk in v_x for a single atom starting at the center of the Zeeman slower with velocity $\mathbf{v} = (0, 0, 300)^T$ as an example.

The power, detuning and current in this compression stage is found by iteratively altering their values and optimizing. The final optimized values are 20 mW per beam, −15 MHz and 20 A, respectively, given that the beams measure 20 mm × 10 mm. This value of the detuning is corroborated by the same value employed in [64]. Figure 5.5 shows how the number of interrogated atoms varies with both detuning and current for a constant power. This suggests

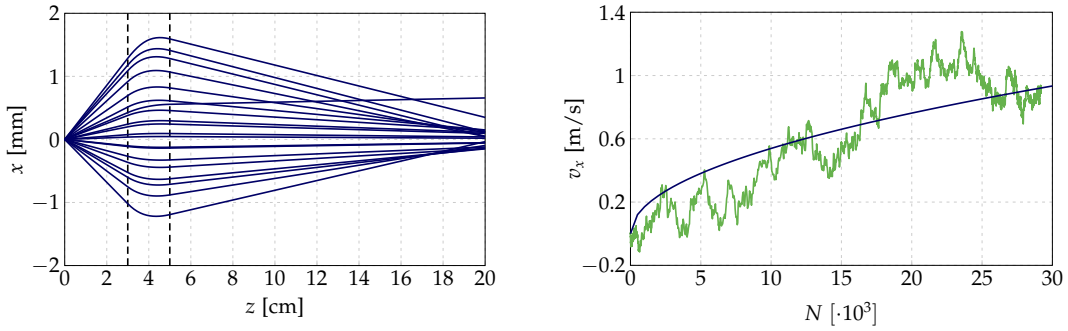

Figure 5.4: Left: Compression of an atomic beam after effusing from an oven, where the dashed lines mark the 2D MOT. The transition is highly saturated. Right: Random walk in a Zeeman slower in v_x-space as a function of scattered photons N for a single atom, plotted alongside the expected average $\sqrt{0.9 v_{\text{rec}}^2 N/3}$ (solid blue line), c.f. (3.34). The initial velocity of the atom is $\mathbf{v} = (0, 0, 300)^T$.

that the detuning $\delta_0/2\pi = -40\,\text{MHz}$ in our system is not the optimal value. It is interesting to note that the gain decreases for currents above 20 A due to excessive compression of the atomic beam, c.f. figure 5.4. This stage roughly yields a gain of a factor of 15 in interrogated atoms.

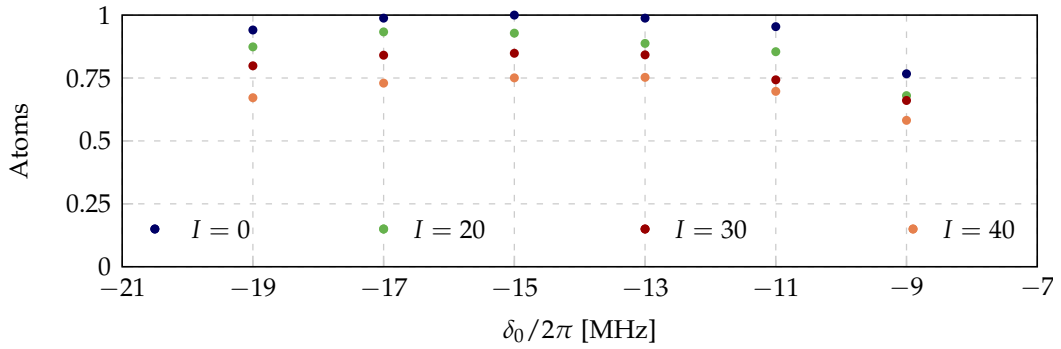

Figure 5.5: Numerical behavior of the number of interrogated atoms (normalized to the largest value) for various values of the detuning and current of the 2D MOT employed right after the oven. The power is fixed at 20 mW per beam.

5.1.2 Second and Third Section: Deflection and Final Collimation

After exitting the slower the atoms are bent by an angle θ. This has two advantages, namely that residual 461 nm light and hot atoms will not perturb the spectroscopy. In practice bending the atoms is accomplished by employing yet another 2D MOT using the strong transition $|^1\text{S}_0\rangle \rightarrow |^1\text{P}_1\rangle$, where the 20 mm $\times$ 20 mm beams are tilted by the angle θ. The value $\theta = 20°$ is deemed sufficient for this purpose. Numerically, bending the atoms is simplified by transforming to the coordinate system imposed by the bending beams, i.e. all coordinates are rotated along y by an amount θ. The optimized values for the power, detuning and current in the bend are 5 mW per beam, -5 MHz and 4 A. Figure 5.6 shows how the number of interrogated atoms vary with current for fixed values of the detuning and power.

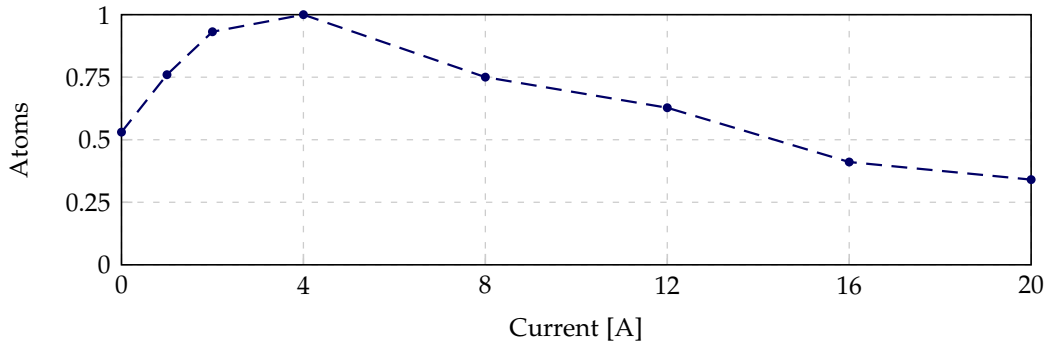

Figure 5.6: Numerical behavior of the number of interrogated atoms (normalized to the largest value) for various values of the current through the wires creating the quadropole field at the bend. The detuning and power is fixed at $\delta_0/2\pi = -5\,\mathrm{MHz}$ and 5 mW per beam, respectively.

The final compression consists of three independent stages, each having its own beam measuring 50 mm × 20 mm which drives the narrow intercombination line $|{}^1S_0\rangle \rightarrow |{}^3P_1\rangle$ due to the attainable 1D Doppler velocity $\sqrt{\hbar\Gamma/2m} = 0.42\,\mathrm{cm/s}$. This allows us to reach velocities smaller than $\Gamma/k = 0.52\,\mathrm{cm/s}$ along the interrogation axis, in contrast to $|{}^1S_0\rangle \rightarrow |{}^1P_1\rangle$ which has a Doppler velocity of 26.9 cm/s per dimension. It should be noted that our classical approach is justified, since the condition (3.3) is also satisfied for the intercombination line.

In order to capture a broad range of atoms, the frequency of each stage is harmonically scanned at a rate $\Omega = 50\,\mathrm{kHz}$, in practice accomplished by each stage having its own dedicated AOM. The scan depth has been optimized for each stage such that stage 1 oscillates through the frequency interval $\delta_1/2\pi = (-1.5, -0.8)\,\mathrm{MHz}$, stage 2 through $\delta_2/2\pi = (-0.8, -0.3)\,\mathrm{MHz}$ and stage 3 through $\delta_3/2\pi = (-0.3, -0.1)\,\mathrm{MHz}$. These values ensure that an atom with a transverse velocity component up to 0.65 m/s can be captured and slowed down sufficiently.

The number of interrogated atoms is sensitive to the power used in each of the three red-cooling stages, as shown in figure 5.7. Even though the saturation intensity of the transition is merely $I_{\mathrm{sat}} = 3\,\mu\mathrm{W/cm^2}$, the transition linewidth is heavily power-broadened for powers above 1 mW, which increases the efficiency of sweeping the frequency. It is found that no magnetic gradient is necessary at this section. The power 5 mW will be used in the following. Table 5.1 summarizes the parameters obtained from optimizing the three sections treated so

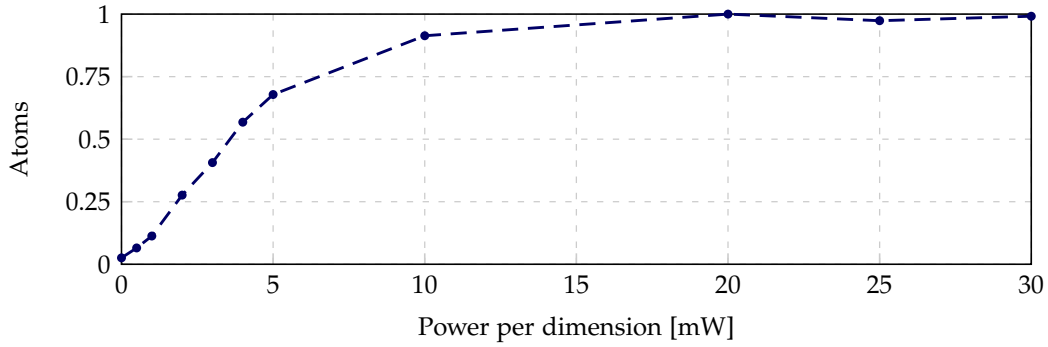

Figure 5.7: Numerical behavior of the number of interrogated atoms (normalized to the largest value) as a function of the power per beam in each red-cooling stage. No magnetic gradient is employed.

far, and these parameters will be utilized from now on.

Section	Transition	Power per beam [mW]	$\delta_0/2\pi$ [MHz]	Current [A]	Beam dimensions [mm × mm]
1	$\left\|{}^1S_0\right\rangle \rightarrow \left\|{}^1P_1\right\rangle$	20	-15	20	20×10
2	$\left\|{}^1S_0\right\rangle \rightarrow \left\|{}^1P_1\right\rangle$	5	-5	4	20×20
3_1	$\left\|{}^1S_0\right\rangle \rightarrow \left\|{}^3P_1\right\rangle$	5	$-(1.5 \ldots 0.8)$	0	50×20
3_2	$\left\|{}^1S_0\right\rangle \rightarrow \left\|{}^3P_1\right\rangle$	5	$-(0.8 \ldots 0.3)$	0	50×20
3_3	$\left\|{}^1S_0\right\rangle \rightarrow \left\|{}^3P_1\right\rangle$	5	$-(0.3 \ldots 0.1)$	0	50×20

Table 5.1: Final parameters for the beamline in figure 5.1. The detuning δ_0 is relative the respective transition frequency.

For illustrative purposes, figure 5.8 shows the projected trajectories through the system for various atoms. Here it is clearly seen how the divergence of the atomic beam is increased during deceleration in the Zeeman slower.

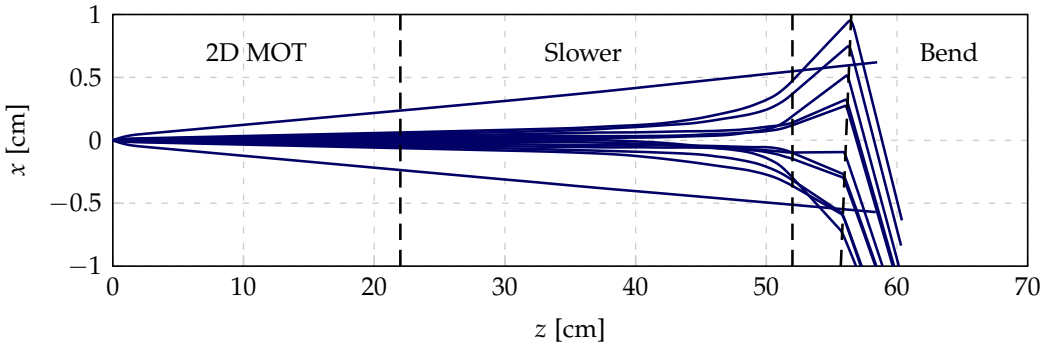

Figure 5.8: The computed trajectories for atoms ($v_z = 300\,\mathrm{m/s}$) through the beamline with transverse velocities ranging from $(0 \ldots \pm 5)$ m/s in integer steps and $\pm 12\,\mathrm{m/s}$, where the latter two atoms are not slowed down. The last part consisting of the red cooling stage has not been included for clarity. The dashed lines are separators between the initial 2D MOT, the Zeeman slower and the bend.

The distribution of the velocity component perpendicular to the interrogation axis is shown in figure 5.9 (right) for the atoms entering the cavity. It has the mean $\langle v_z \rangle = 11.7\,\mathrm{m/s}$, such that the transit-time broadening is merely $12\,\mathrm{kHz} \sim \Gamma/2\pi = 7.6\,\mathrm{kHz}$ as desired. This velocity component cannot be decreased further, since gravity will then degrade the flux substantially. The spatial distribution of the atoms entering the cavity is shown in figure 5.9 (left), and it is much denser around $y \simeq -0.25\,\mathrm{mm}$ due to gravity. The atoms enter the cavity through an area measuring $6\,\mathrm{mm} \times 1\,\mathrm{mm}$, placed at the cavity center $(0, 0)$.

Through calibration the atomic flux through the area $6\,\mathrm{mm} \times 1\,\mathrm{mm}$ at the cavity is found to be $3.6 \cdot 10^{11}$ atoms/s. The flux $\mathcal{F}$ in units of $\mathrm{s^{-1}\,m^{-2}}$ is related to $\langle v_z \rangle$ by the particle density ρ, $\mathcal{F} = \rho \langle v_z \rangle$. Utilizing this relation then yields a particle density $5.1 \cdot 10^9\,\mathrm{atoms/cm^3}$, corresponding to $N = 3.1 \cdot 10^7$ atoms at each instant of time in the volume $6\,\mathrm{mm} \times 1\,\mathrm{mm} \times 1\,\mathrm{mm}$ at the cavity center. This volume is covered by the cavity TEM_{00} mode, which we assumed had a waist of 1 mm. It should be noted that in reality only 83 % of this population is ^{88}Sr, amounting to $2.5 \cdot 10^7$ atoms. This is the main result of this section.

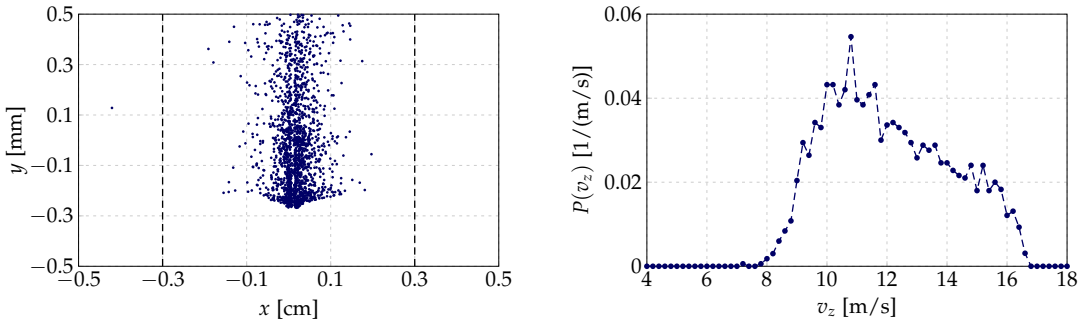

Figure 5.9: Left: The spatial distribution of 10^3 atoms reaching the cavity. The interrogation axis is placed along x. Right: The distribution of the atomic velocity component v_z perpendicular to the interrogation axis for the atoms entering the cavity, displaying the mean $\langle v_z \rangle = 11.7\,\mathrm{m/s}$.

This atomic population is more than sufficient for nonlinear spectroscopy. Specifically, with a cavity finesse of 200 and $P_{\mathrm{in}} = 16\,\mu\mathrm{W}$ of incoupled power, the attainable linewidth (2.58) with $N = 10^7$ atoms is $\Delta\nu_{\mathrm{FWHM}} \simeq 11\,\mathrm{mHz}$, showing that the proposed beamline in figure 5.1 is in principle able to realize the spectroscopy scheme continuously. These numbers correspond to a 1 Hz bandwidth-normalized SNR of $\sqrt{\kappa \mathcal{C}^2 n_0 \beta} \simeq 3 \cdot 10^6$ [15], assuming unity photodetector quantum efficiency.

It is interesting to investigate how this number behaves with the oven temperature. More specifically, the vapor pressure P of Sr as a function of oven temperature T goes as [65]

$$\log_{10}(P\,[\mathrm{Pa}]) = 14.232 - \frac{8572}{T\,[\mathrm{K}]} - 1.1926 \log_{10}(T\,[\mathrm{K}]). \tag{5.2}$$

Increasing T by roughly 100 K thus increases the flux by almost an order of magnitude, but in turn this also shifts the axial velocity distribution to higher velocities, which reduces the efficiency of the deceleration process in the Zeeman slower. The change in atomic population as a function of T has been tested out explicitly, showing that the increase in flux is the dominant effect. The results are shown in figure 5.10, revealing that the population is almost doubled when increasing the oven temperature from 530 °C to 565 °C. The loading rate of a MOT behaves similarly [32].

5.2 Summary

Our Monte Carlo simulation shows that the proposed beamline in figure 5.1 is promising in the context of realizing cavity-enhanced nonlinear spectroscopy and may serve as a continuous alternative to an optical lattice. One should keep in mind that the calculations in this chapter are performed under highly idealized conditions and the number of interrogated atoms will depend on how well the situation treated here is realized experimentally. As an example, there may be structure in the beam used for the Zeeman slower which decreases its efficiency. In this respect figure 3.9 suggests that we are describing the physics in the Zeeman slower reasonably. Another discrepancy may be due to misaligned beams in the various 2D MOTs, but it is reassuring that a decrease in interrogated atoms up to a factor of six due to imperfect beam alignment can be compensated for by increasing the oven temperature.

The beamlime also has the feature that it can be used for other isotopes of Sr, simply by varying the detunings of the various cooling beams by the associated isotope shifts.

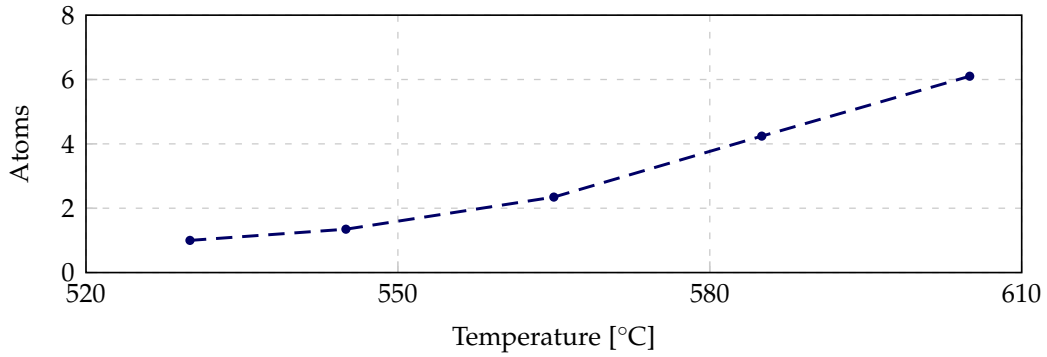

Figure 5.10: Numerical behavior of the number of interrogated atoms as a function of the oven temperature T, normalized to the value at 530 °C treated so far. At 600 °C the number of atoms is increased by roughly a factor of six.

It may also prove relevant in other experiments where a monoenergetic atomic beam is desired. For example, it could be used when referencing a laser against an optical transitition as was done with the trapping light used for the MOT in figure 4.3. Here the beamline would completely eliminate the Doppler background, in which case locking to the transition would yield the same performance as if one had locked directly to the Lamb dip. As a first approximation, the obtained instability can be estimated using (1.1), where the clock cycle T_c is the transit time, yielding $\sigma(\tau) \simeq 2.2 \cdot 10^{-16}/\sqrt{\tau}$. This is not a realistic estimate, since fluctuations in the oven temperature and shot-noise of both the signal and atomic beam have not been included. Nonetheless, it serves as a motivation for a more thorough analysis, revealing how far down the instability can be integrated.

Chapter 6

Epilogue

The work presented in this thesis has been concerned with the theory and work towards realization of cavity-enhanced nonlinear spectroscopy. This is motivated by the fact that it theoretically enables performing direct continuous spectroscopy on ultranarrow optical transitions of localized atoms, something which is otherwise extremely complicated by the small sub-Hz transition linewidth. This enables stabilizing a laser to the transition in question, thereby circumventing the fundamental limit on the stability caused by thermal noise in the mirrors of the high-Q cavities that lasers are currently stabilized to.

6.1 Conclusion and Outlook

The main idea behind cavity-enhanced nonlinear spectroscopy is quite simple: Since the saturation intensity of a transition scales with its linewidth, performing continuous spectroscopy on ultranarrow optical transitions is technically challenging. One way to counteract this is to increase the optical depth of the atomic sample, which is done by placing the atoms inside a cavity. Since this is the only function of the cavity, it does not have to be high-Q. As we showed both classically and quantum mechanically, in the linear regime $I/I_{\text{sat}} \ll 1$ a consequence of the increased optical depth is that the combined system is strongly absorptive over a frequency range many linewidths broad. Consequently, very large intensities $I/I_{\text{sat}} \gtrsim 100$ are needed to see a signal, which brings with itself nonlinear effects such as optical bistability. Above this bistable domain we showed both classically and quantum mechanically that a transmission peak emerges around the combined resonance of the atom and cavity due to strong bleaching of the atomic transition. The cavity also increases the optical throughput by a factor on the order of the cooperativity squared, amounting to at least three orders of magnitude. This is what enables detecting the signal, but it is at the expense of a power-broadened transition. Despite this, as we showed the ultimate lock precision can still potentially outperform state-of-the-art currently set by the sub-40 mHz linewidth attained in [14].

The work performed during this thesis has been towards the realization of this spectroscopy scheme with ^{88}Sr, utilizing the $\left|{}^1\mathrm{S}_0\right\rangle \rightarrow \left|{}^3\mathrm{P}_1\right\rangle$ transition at 689 nm. This ideally requires localizing the atoms in a three-dimensional optical lattice during interrogation, operating at the magic wavelength. However, this is not available in the experiment at the current stage. A poor man's approach is simply to keep the atoms confined in the magneto-optical trap operating on the $\left|{}^1\mathrm{S}_0\right\rangle \rightarrow \left|{}^1\mathrm{P}_1\right\rangle$ transition at 461 nm during interrogation, which we showed explicitly does not pose a problem. The main disadvantage is that a stronger requirement is put on the number of optically trapped atoms, but this is well within the limits of currently achievable

populations.

Having established the framework of our system, we initiated the construction of a magneto-optical trap. A large population of trapped atoms is greatly aided by a continuous flux of cold atoms, and for this purpose we designed, built and implemented a Zeeman slower in the vacuum system. Its flux and efficiency has been measured, showing that its performance is similar to that of other systems for ^{88}Sr. Along with this a Monte Carlo simulation of the atomic trajectories has also been constructed, which takes into account the transverse heating associated with axial deceleration. This simulation optimized the implementation of the slower.

At this stage the magneto-optical trap is operational, which allows for spectroscopy on the atomic cloud. We measured the one-body loss rate as a function of the total trapping beam intensity, and the measurements corroborate our analytical treatment. A repumper has also been employed, which increases the trap population by almost a factor of three. The same efficiency is displayed in similar systems. We numerically investigated the dynamics of the atomic cloud immediately after turning on the repumper, but no quantitiative agreement was found between measurements and theory. It is plausible that this discrepancy is caused by coupling to dark states and a reduced repumping efficiency due to the varying Zeeman shift in the quadropole field, something that we have not included in our highly idealized model. Future work on the trap consists of employing the 679 nm repumper in order to reach the necessary trap population.

With cavity-enhanced nonlinear spectroscopy in mind, we have proposed a design for a beamline which serves as a continuous alternative to the required three-dimensional optical lattice. In order not to transit-time broaden the interrogated transition, the velocity of the cold atomic beam must be on the order of 15 m/s. Additionally, the velocity along the interrogation axis must be within one linewidth, $\pm\Gamma/k$. We have simulated the proposed design stochastically, and it is found that under optimal experimental conditions more than 10^7 atoms can satisfy these requirements inside the cavity at each instant of time with a favorable SNR, which is sufficient for our purpose.

6.2 Outlook

The beamline may also be relevant in observing and utilizing a completely different phenomenon, namely superradiance which is based on collective emission. This is briefly outlined in the following section, where it is also explained how this can be used for laser stabilization.

6.2.1 Superradiance

Looking at a single two-level atom placed in free space and in its excited state, it can either display resonant flourescence by continuously driving the dipole with an external quasi-resonant EM-field or it can spontaneously decay. Assuming the incoming laser is linearly polarized, the emitted intensity pattern of resonant flourescence is given by the usual expression $\propto \sin^2\theta$, where θ is taken relative the polarization axis and the pattern thus takes the shape of a torus. Spontaneous emission is, however, due to the coupling of the atomic dipole to the vacuum field modes and the associated exponential decay emerges from the Wigner-Weisskopf theory. The characteristic decay time is $\tau = 1/\Gamma$, where Γ is the transition linewidth.

We now turn to a dilute ensemble of N independent atoms, fully inverted at $t = 0$. Denoting the random phase of each atom by ϕ_n and the electric field emitted by a single atom by E_1, the

intensity I_N of the total spontaneous emission is

$$I_N \propto \left| \sum_n E_1 e^{i\phi_n} \right|^2 \tag{6.1}$$

$$= I_1 \left(N + \sum_{n \neq m} e^{i(\phi_n - \phi_m)} \right) \tag{6.2}$$

$$= I_1 N, \tag{6.3}$$

where the last term of (6.2) is zero due to unit length random walk. Since the atoms are independent, the emission pattern is completely isotropic. This situation describes the usual incoherent spontaneous relaxation of an excited atomic ensemble.

The temporal and spatial behavior of the emitted pulse is altered considerably if the sample is dense, $N \gg 1$. Specifically, by mapping the N two-level atoms onto a pseudo-spin system of total spin $N/2$, Dicke [66] showed that the N atoms, which have no optical dipole moment at $t = 0$, would be coupled together through their common radiation fields when their volume $V \leq \lambda^3$, where λ is the emitted wavelength. In other words, the initial spontaneous emission from a fraction of the system will correlate the various dipoles in the system, thereby forming one macroscopic dipole moment. In the extreme case where all emitters become phase-locked ($\phi_n = \phi_1$) we obtain from (6.1) that $I_N = I_1 N^2$, and due to conservation of energy the collective sample is deexcited after the characteristic time τ/N. This introduces the concept of cooperative emission, generally known as superradiance. This process is inherently quantum mechanical in nature, since vacuum fluctuations are required to initiate the relaxation process. It also contains a classical aspect as the subsequent emission is due to the radiation of an ordered array of dipoles, which has an immediate classical analogue in terms of coherently radiating antennas.

The description so far has only treated superradiance in a transient domain, and since vacuum fluctuations initiate the process, the phases of independent bursts are not correlated. In principle such a system can be realized in a three-level system with states $\{|0\rangle, |1\rangle, |2\rangle\}$ [67]. The pump with rate w is resonant with the transition $|0\rangle \rightarrow |2\rangle$, from which collective relaxation occurs to $|1\rangle$. Steady-state superradiance is achieved by periodically creating population inversion on the superradiant transition $|2\rangle \rightarrow |1\rangle$.

Recent proposals suggest using ultracold alkaline-earth atoms trapped in an optical lattice inside a high-finesse cavity to achieve steady-state superradiance [68, 69]. Unlike dipole-allowed transitions, narrow optical intercombination lines allow for population inversion to build up in the metastable excited state faster than the depletion due to the fast collective decay. Since $\Gamma \sim$ Hz and $\kappa >$ kHz, this system operates deep in the optical bad-cavity limit $\kappa \gg \Gamma$, where the intracavity photon number $\lesssim 1$. From the system master equation it follows that the atom-field coupling g_0 is directly responsible for the nonzero dipole correlations [68], so in this setup the collective behavior does not originate from the sample size as in usual Dicke superradiance. The correlation is instead mediated by the weak intracavity field, originating from the coupling g_0.

In addition to $V/\lambda^3 \sim 1$, the conditions for self-sustained superradiance are quantified by $NC_0\Gamma \gg (\Gamma, T_2^{-1})$ and $w \sim NC_0\Gamma$ [69]. Increasing the pumping rate above this threshold destroys the coherences between various dipoles faster than the intracavity light can induce them. The use of ultracold atoms in this respect minimizes the effective dephasing rate T_2^{-1}, allowing for longer superradiant behavior.

Such a light source is inherently different from conventional good-cavity lasers, where $\kappa \lesssim \Gamma$. In a standard laser above threshold the coherence is contained in the photons propagating inside the cavity. The phase information is retained through stimulated emission, but

consequently the phase carried by the photons is easily perturbed by thermal motion of the cavity mirrors. In contrast, in a superradiant light source the phase information is entirely contained within the macroscopic dipole moment formed by the atoms. The intracavity photons merely act as to synchronize the various moments and extract the phase through stimulated emission, so the sensitivity to thermal and mechanical mirror motion is greatly reduced, allowing them to reach linewidths given by $\Delta\nu = \mathcal{C}_0\Gamma/\pi$ [68]. Specifically, for the doubly forbidden $\left|{}^1\mathrm{S}_0\right\rangle \rightarrow \left|{}^3\mathrm{P}_0\right\rangle$ of fermionic ^{87}Sr the linewidth of the emitted light is projected at the µHz-level, two orders of magnitude smaller than current state-of-the-art. Such a stabilized laser could readily be employed as LO in an optical lattice clock.

The output power only reaches the maximum $P = \hbar\omega N^2\mathcal{C}_0\Gamma/8 \sim$ nW, but this is sufficient for subsequent phase-locking [70] of a secondary laser. This characterizes an active system, where the phase reference light is derived directly from the atomic transition, which is another way to circumvent the residual thermal noise floor of reference cavity mirrors.

The proposed beamline is more than able to satisfy the required strong coupling $N\mathcal{C}_0 = \mathcal{C} \gg 1$ for $\left|{}^1\mathrm{S}_0\right\rangle \rightarrow \left|{}^3\mathrm{P}_1\right\rangle$ of ^{88}Sr needed for superradiance. A cavity with finesse 200 has a linewidth κ on the order of MHz $\gg \Gamma$ such that the single-atom cooperativity $\mathcal{C}_0 \sim 10^{-5}$ and the linewidth of the emitted light is projected at $\Delta\nu \simeq 0.5$ Hz. The authors of [71] have recently demonstrated a superradiant laser with a linewidth of a few Hz that contains less than one intracavity photon on average, but the emission only lasts for roughly 140 ms, limited by the atomic loss of the one-dimensional optical lattice. The advantage of the beamline is that this loss is not an issue, serving as a further motivation for obtaining superradiance in the proposed system and for realizing the beamline.

6.3 Acknowledgment

Thanks to my advisors J. W. Thomsen and P. G. Westergaard for the many enlightening discussions and helpful comments. I would also like to thank M. J. Martin at JILA NIST-CU for useful discussions.

Appendix A

Pound-Drever-Hall Stabilization Scheme

The spectral width of a laser can be reduced by locking it to a stable reference. This can be accomplished by the Pound-Drever-Hall scheme, which is a heterodyne sideband technique that derives an antisymmetric error signal based on the phase of the light reflected from a stable reference cavity.

The scheme is realized by modulating the phase of a linearly polarized laser beam by an EOM. Assuming a modulation frequency Ω and depth β, the field impinging on the cavity can be expanded in terms of sidebands using the Jacobi-Anger expansion

$$E_I = E_0 e^{i[\omega t + \beta \sin(\Omega t)]} \tag{A.1}$$

$$= E_0 \sum_{n=-\infty}^{\infty} J_n(\beta) e^{i(\omega + n\Omega)t} \tag{A.2}$$

$$\simeq E_0 \Big(J_0(\beta) e^{i\omega t} + J_1(\beta) e^{i(\omega+\Omega)t} - J_1(\beta) e^{i(\omega-\Omega)t} \Big), \tag{A.3}$$

where the relation $J_{-1}(\beta) = -J_1(\beta)$ has been utilized in (A.3) in addition to the assumption $\beta \ll 2$. Upon reflection from the cavity the field becomes

$$E_R = F(\omega) E_0 J_0(\beta) e^{i\omega t} + E_0 J_1(\beta) \Big(F(\omega+\Omega) e^{i(\omega+\Omega)t} - F(\omega-\Omega) e^{i(\omega-\Omega)t} \Big), \tag{A.4}$$

where $F(\omega)$ denotes the reflection coefficent for the reference cavity of length L and FSR $= c/2L$,

$$F(\omega) \equiv \frac{E_R}{E_I} = r \frac{e^{i\omega/\mathrm{FSR}} - 1}{1 - r^2 e^{i\omega/\mathrm{FSR}}}. \tag{A.5}$$

The carrier and two FM sidebands are reflected with different phases. Their interference is detected by a photodiode, which measures the power $P_R \equiv |E_R|^2$, yielding [72]

$$\begin{aligned} P_R = P_c |F(\omega)|^2 + P_s \Big[|F(\omega+\Omega)|^2 + |F(\omega-\Omega)|^2 \Big] \\ + 2\sqrt{P_c P_s} \Re[F(\omega) F^*(\omega+\Omega) - F^*(\omega) F(\omega-\Omega)] \cos(\Omega t) \\ + 2\sqrt{P_c P_s} \Im[F(\omega) F^*(\omega+\Omega) - F^*(\omega) F(\omega-\Omega)] \sin(\Omega t) \\ + \mathcal{O}(2\Omega), \end{aligned} \tag{A.6}$$

where $P_c = J_0^2(\beta) P_I$ ($P_s = J_1^2(\beta) P_I$) refers to the optical power in the carrier (single sideband component). The first term of (A.6) is a DC term, whereas the second and third terms are in phase and in quadrature with the photodiode current, respectively. The latter terms are due

to the interference between the carrier and the sidebands, whereas the higher-order harmonics are due to the sidebands interfering with each other and hence uninteresting. In what follows they are neglegted, and in practice they are filtered away. The signal from the photodiode (A.6) is then phase-sensitively detected by mixing it with the LO $\sin(\Omega t + \phi)$ after which it is low-pass filtered (LPF), collectively realizing the signal lock-in. Assuming a relative LO phase $\phi = 0$ and a properly chosen cutoff frequency for the low-pass, only the DC term from $\sin^2(\Omega t)$ survives resulting in the signal

$$\varepsilon(\omega) = \eta_{\text{PD}}\zeta\sqrt{P_c P_s}\Im[F(\omega)F^*(\omega+\Omega) - F^*(\omega)F(\omega-\Omega)], \tag{A.7}$$

where η_{PD} denotes the quantum efficiency of the photodetector and ζ the power-to-voltage conversion factor. This constitutes the error signal, which is fed to the servo controlling the laser frequency, thus locking the laser to a mode of the stable reference cavity. A setup is illustrated in figure A.1, where the optical isolator (OI) ensures that no unwanted feedback is sent to the laser.

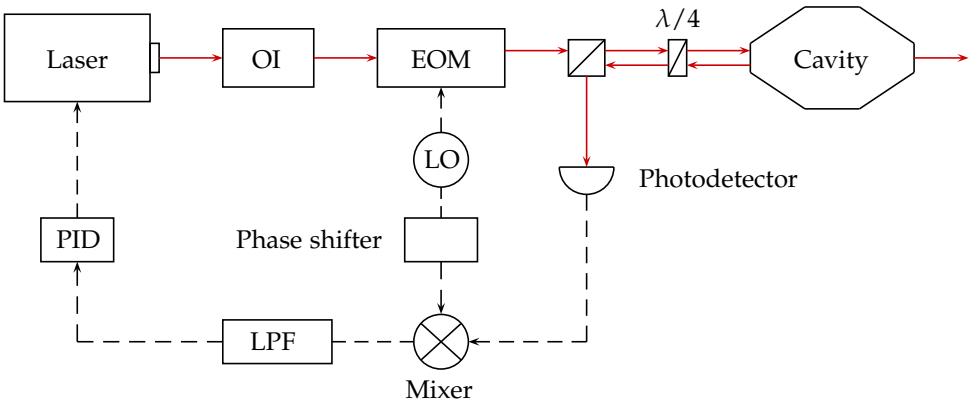

Figure A.1: The Pound-Drever-Hall locking setup. The optical isolator (IO) enures that no unwanted feedback is sent to the laser. After the low-pass filter (LPF) the error signal $\varepsilon(\omega)$ is fed to a PID controller, which constitutes the servo loop.

The term $\Im[F(\omega)F^*(\omega+\Omega) - F^*(\omega)F(\omega-\Omega)]$ contains information about the phase of E_R. This is seen when recalling that Ω is generally large enough for the sidebands to be far from resonance, in which case $F(\omega \pm \Omega) \simeq -1$ such that $\Im[F(\omega)F^*(\omega+\Omega) - F^*(\omega)F(\omega-\Omega)] = -2\Im[F(\omega)]$. Unlike the intensity, the phase of the reflected light reveals which side of the cavity resonance the reflected light is on, which is why this scheme works. The sidebands in this respect effectively set a phase standard with which the phase of the reflected beam is extracted through the beat pattern with the reflected carrier [72].

For $F(\omega \pm \Omega) \simeq -1$ the error signal (A.7) reduces to

$$\varepsilon(\omega) = -2\eta_{\text{PD}}\zeta\sqrt{P_c P_s}\Im[F(\omega)]. \tag{A.8}$$

This expression can be explored more carefully when the carrier is close to resonance, in which case

$$\frac{\omega}{\text{FSR}} = 2\pi n + \frac{\delta\omega}{\text{FSR}} \tag{A.9}$$

for $n \in Z_+$ and $\delta\omega$ is the deviation of the laser from resonance. In the limit $R = |r|^2 \simeq 1$ the cavity finesse $\mathcal{F}$ becomes

$$\mathcal{F} \equiv \frac{\text{FSR}}{\kappa} = \frac{\pi\sqrt{R}}{1-R} \tag{A.10}$$

$$\simeq \frac{\pi}{1-R}. \tag{A.11}$$

Expanding (A.5) to first order and utilizing (A.11) yields

$$F(\omega) \simeq i\frac{\mathcal{F}}{\pi\,\text{FSR}}\kappa, \tag{A.12}$$

in which case (A.8) reduces to

$$\varepsilon(\omega) = -2\eta_{\text{PD}}\zeta\sqrt{P_c P_s}\frac{1}{\pi\kappa}\delta\omega. \tag{A.13}$$

The error signal is proportional to the laser frequency deviation from resonance. The quantity $-2\eta_{\text{PD}}\zeta\sqrt{P_c P_s}/(\pi\kappa)$ gives the slope of the error signal, and maximimizing this slope requires maximizing $J_0(\beta)J_1(\beta)$. Numerically the optimum value $\beta \simeq 1.082$ is found, yielding $J_0(\beta)J_1(\beta) \simeq 0.339$. A high-finesse cavity is seen also to be a requirement for an efficient lock. The error signal is shown in figure A.2.

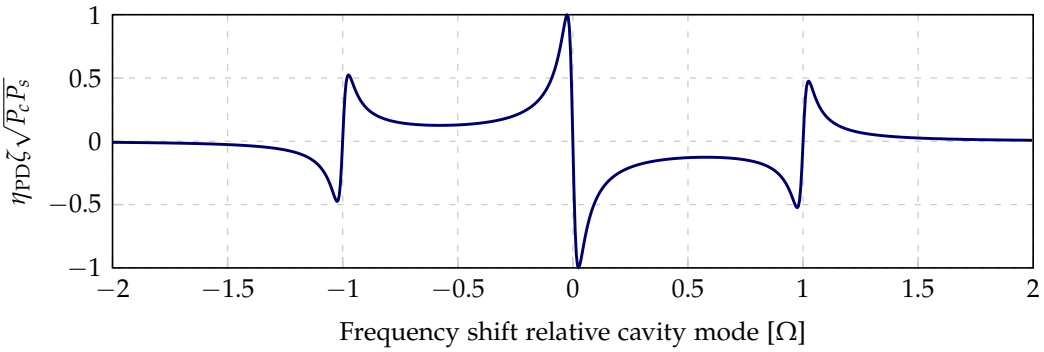

Figure A.2: The Pound-Drever-Hall error signal (A.7) given a cavity with finesse $\mathcal{F} = 5 \cdot 10^4$ and modulation frequency $\Omega/2\pi = 10\,\text{MHz}$.

Appendix B

Magnetic Field of Parallel Conductors

Four parallel straight wires are arranged at the corners of a square as illustrated in figure B.1 (left), where the currents in adjacent wires flow in opposite directions. The magnetic field gradient $\nabla_{\mathbf{B}}$ must satisfy

$$\frac{dB_x}{dx} = -\frac{dB_y}{dy} \equiv \nabla_{\mathbf{B}} \tag{B.1}$$

since $\nabla \cdot \mathbf{B} = 0$. The magnetic field for a single wire situated at (x_i, y_i) is readily obtained from the Biot-Savart law under the assumption that it is infinitely long and thin

$$\mathbf{B} = \frac{\mu_0 I}{2\pi}\left(\frac{1}{(x-x_i)^2 + (y-y_i)^2}\right)[-(y-y_i)\mathbf{e}_x, (x-x_i)\mathbf{e}_y]. \tag{B.2}$$

Here we have utilized that the azimuthal angle ϕ of (r, ϕ, z) satisfies $\mathbf{e}_\phi = -\sin(\phi)\mathbf{e}_x + \cos(\phi)\mathbf{e}_y$ and

$$\sin\left[\arctan\left(\frac{y}{x}\right)\right] = \frac{y}{x\sqrt{1+y^2/x^2}} \tag{B.3}$$

$$\cos\left[\arctan\left(\frac{y}{x}\right)\right] = \frac{1}{\sqrt{1+y^2/x^2}}. \tag{B.4}$$

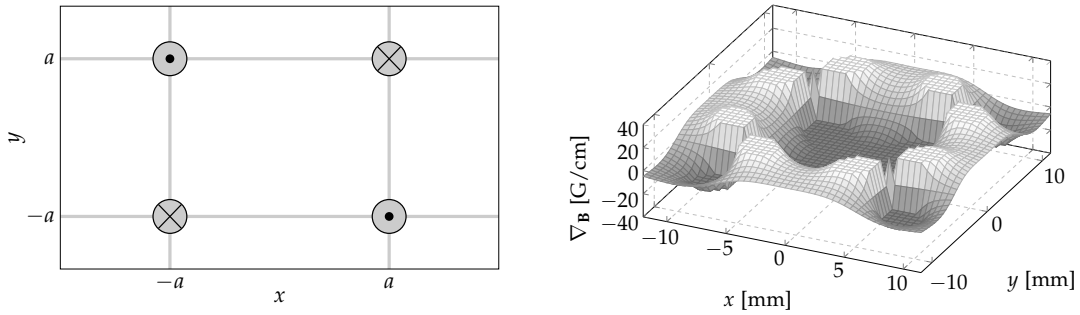

Figure B.1: Left: The square configuration resulting in a quadropole field. Right: The corresponding gradient for the case where $a = 6\,\text{mm}$ and $I = 60\,\text{A}$. Between wires typical gradient magnitudes are around $0.4\,\text{G}/(\text{cm}\,\text{A})$.

Summing the contribution from all four wires yields the gradient

$$\begin{aligned}\nabla_{\mathbf{B}} = &-\frac{I(a+x)(a-y)\mu_0}{\pi[(a+x)^2+(-a+y)^2]^2}+\frac{I(-a+x)(a-y)\mu_0}{\pi[(-a+x)^2+(-a+y)^2]^2}\\ &-\frac{I(-a+x)(-a-y)\mu_0}{\pi[(-a+x)^2+(a+y)^2]^2}+\frac{I(a+x)(-a-y)\mu_0}{\pi[(a+x)^2+(a+y)^2]^2},\end{aligned} \tag{B.5}$$

shown in figure B.1. In reality the field magnitude at the ends will be smaller since they are of finite length, but this discrepancy is neglegted in favor of the analytically simpler expressions. As illustrated in figure B.2 the field is indeed linear inside the square.

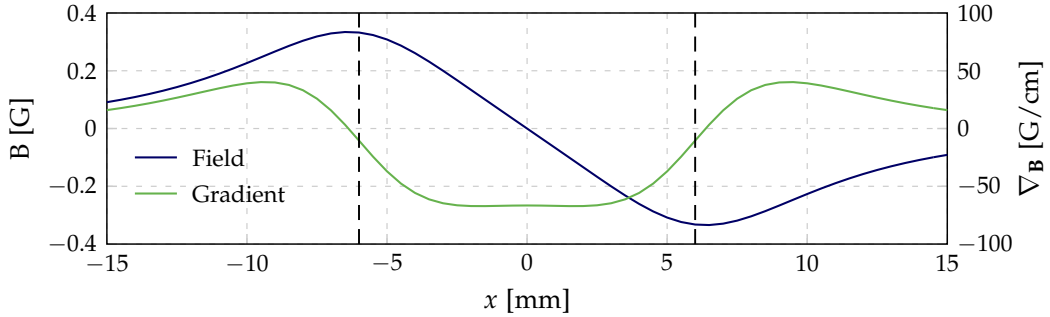

Figure B.2: A cross section along $y = 1\,\text{mm}$ of the magnetic field and gradient for the square configuration in figure B.1 with $a = 6\,\text{mm}$ and $I = 60\,\text{A}$.

Appendix C

Flux of a Collimated Atomic Beam

An ideal atomic gas at temperature T and density n is assumed to be in thermal equilibrium, contained in an oven. Given that the oven is placed in vacuum and that it has a circular aperture of area A, atoms will escape through it due to the pressure gradient. In what follows the mean free path of escaping atoms is assumed much greater than the aperture radius, due to which the atoms effuse out of the oven without colliding with eachother. In turn this implies that the velocity distribution of the atoms left inside the oven is not changed by the presence of the aperture and the equilibrium is thus left undisrupted.

We will start by finding the flux of atoms that effuse out of the oven at an angle θ with speed v, see figure C.1. This corresponds to the volume $Av\cos\theta dt$ and the number of atoms

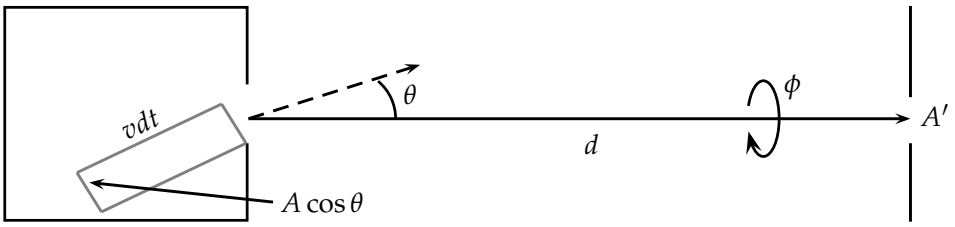

Figure C.1: Atoms with speed v effusing out of an oven with circular aperture A at an angle θ, after which they are collimated by a secondary circular aperture of area A' a distance d away.

$nAv\cos\theta dt$, so the flux leaving through A during dt is given by $nAv\cos\theta$. Since the atoms are in thermal equilibrium, the total flux is readily found by averaging over the speed probability distribution, which in spherical coordinates (v, θ, ϕ) is given by

$$f(v)dv = \left(\frac{m}{2\pi k_B T}\right)^{3/2} \exp\left(-\frac{mv^2}{2k_B T}\right) v^2 dv \sin\theta d\theta d\phi. \tag{C.1}$$

The total flux Φ effusing through A (or, equivalently, into the solid angle π) is thus given by

$$\Phi = 2\pi nA \int_0^\infty f(v)vdv \int_0^{\pi/2} \cos\theta \sin\theta d\theta \tag{C.2}$$

$$= \frac{1}{4} nA\langle v\rangle\,, \tag{C.3}$$

where $\langle v\rangle = \sqrt{8k_B T/\pi m}$ is the average speed of the 3D Boltzmann gas.

The effect of collimating the atomic beam a distance d away with an aperture of area A' can in the limit $A' \gg A$ be included by simply generalizing the maximal inclination to $\arctan[(\sqrt{A'/\pi})/d]$, yielding

$$\Phi' = \Phi \frac{A'}{A' + \pi d^2}. \tag{C.4}$$

Bibliography

[1] W. M. Itano, J. C. Bergquist, J. J. Bollinger, J. M. Gilligan, D. J. Heinzen, F. L. Moore, M. G. Raizen, and D. J. Wineland, "Quantum Projection Noise: Population Fluctuations in Two-Level Systems," *Phys. Rev.* **A47** (1993) 3554–3570.

[2] G. Santarelli, P. Laurent, P. Lemonde, A. Clairon, A. G. Mann, S. Chang, A. N. Luiten, and C. Salomon, "Quantum Projection Noise in an Atomic Fountain: A High Stability Cesium Frequency Standard," *Phys. Rev. Lett.* **82** (1999) 4619–4622.

[3] J. L. Hall, "Nobel Lecture: Defining and Measuring Optical Frequencies," *Rev. Mod. Phys.* **78** (2006) 1279–1295.

[4] G. J. Dick, "Local Oscillator Induced Instabilities in Trapped Ion Frequency Standards," *in Proceedings of the Nineteenth Annual Precise Time and Time Interval* (1987) 133–147.

[5] P. G. Westergaard, *Horloge à Réseau Optique au Strontium: En Quête de la Performance Ultime*. PhD thesis, SYRTE, 2010.

[6] P. Westergaard, J. Lodewyck, and P. Lemonde, "Minimizing the Dick Effect in an Optical Lattice Clock," *IEEE Transactions on Ultrasonics, Ferroelectrics and Frequency Control* **57** 3, (2010) 623–628.

[7] F. Riehle, *Frequency Standards: Basics and Applications*. Wiley-VCH, 2004.

[8] J. Ye, H. J. Kimble, and H. Katori, "Quantum State Engineering and Precision Metrology Using State-Insensitive Light Traps," *Science* **320** (2008) 1734–1738.

[9] I. Courtillot, *Première Observation de la Transition Fortement Interdite* $^1S_0 - {}^3P_0$ *du Strontium, Pour Une Horloge Optique à Atomes Piégés*. PhD thesis, SYRTE, 2003.

[10] T. L. Nicholson, M. J. Martin, J. R. Williams, B. J. Bloom, M. Bishof, M. Swallows, S. Campbell, and J. Ye, "Comparison of Two Independent Sr Optical Clocks with 1×10^{-17} Stability at 10^3s," *Phys. Rev. Lett.* **109** (2012) 230801.

[11] R. H. Bishop, *The Mechatronics Handbook*. CRC Press, 2002.

[12] M. Notcutt, L.-S. Ma, J. Ye, and J. L. Hall, "Simple and Compact 1-Hz Laser System via an Improved Mounting Configuration of a Reference Cavity," *Opt. Lett.* **30** 14, (2005) 1815–1817.

[13] A. D. Ludlow, X. Huang, M. Notcutt, T. Zanon-Willette, S. M. Foreman, M. M. Boyd, S. Blatt, and J. Ye, "Compact, Thermal-Noise-Limited Optical Cavity for Diode Laser Stabilization at 1×10^{-15}," *Opt. Lett.* **32** 6, (2007) 641–643.

[14] T. Kessler, C. Hagemann, C. Grebing, T. Legero, U. Sterr, F. Riehle, M. J. Martin, L. Chen, and J. Ye, "A Sub-40mHz Linewidth Laser Based on a Silicon Single-Crystal Optical Cavity," *Nature Photonics* **6** (2012) 687–692.

[15] M. J. Martin, D. Meiser, J. W. Thomsen, J. Ye, and M. J. Holland, "Extreme Nonlinear Response of Ultranarrow Optical Transitions in Cavity QED for Laser Stabilization," *Phys. Rev. A* **84** (2011) 063813.

[16] M. A. Armen and H. Mabuchi, "Low-Lying Bifurcations in Cavity Quantum Electrodynamics," *Phys. Rev. A* **73** (2006) 063801.

[17] J. Gripp, S. L. Mielke, and L. A. Orozco, "Evolution of the Vacuum Rabi Peaks in a Detuned Atom-Cavity System," *Phys. Rev. A* **56** (1997) 3262–3273.

[18] D. F. Walls and G. J. Milburn, *Quantum Optics*. Springer, 2008.

[19] R. Miller, T. E. Northup, K. M. Birnbaum, A. Boca, A. D. Boozer, and H. J. Kimble, "Trapped Atoms in Cavity QED: Coupling Quantized Light and Matter," *J. Phys. B: At. Mol. Opt. Phys.* **38** (2005) S551–S565.

[20] H. J. Carmichael, *An Open Systems Approach to Quantum Optics*. Springer, 1993.

[21] K. Murch, U. Vool, D. Zhou, S. Weber, S. Girvin, and I. Siddiqi, "Cavity-Assisted Quantum Bath Engineering," *Phys. Rev. Lett.* **109** (2012) 183602.

[22] R. Thompson, G. Rempe, and H. Kimble, "Observation of Normal-Mode Splitting for an Atom in an Optical Cavity," *Phys. Rev. Lett.* **68** (1992) 1132–1135.

[23] A. Wickenbrock, P. Phoonthong, and F. Renzoni, "Collective Strong Coupling in a Lossy Optical Cavity," *Journal of Modern Optics* **58** 15, (2011) 1310–1316.

[24] H. Tanji-Suzuki, I. D. Leroux, M. H. Schleier-Smith, M. Cetina, A. T. Grier, J. Simon, and V. Vuletic, "Interaction Between Atomic Ensembles and Optical Resonators: Classical Description," *Advances in Atomic, Molecular, and Optical Physics* **60** (2011) 201–237.

[25] C. Cohen-Tannoudji, J. Dupont-Roc, and G. Grynberg, *Atom-Photon Interactions: Basic Processes and Applications*. Wiley-VCH, 1998.

[26] J. Dalibard and C. Cohen-Tannoudji, "Dressed-Atom Approach to Atomic Motion in Laser Light: The Dipole Force Revisited," *J. Opt. Soc. Am. B* **2** 11, (1985) 1707–1720.

[27] W. Ertmer, R. Blatt, J. L. Hall, and M. Zhu, "Laser Manipulation of Atomic Beam Velocities: Demonstration of Stopped Atoms and Velocity Reversal," *Phys. Rev. Lett.* **54** (1985) 996–999.

[28] W. D. Phillips and H. Metcalf, "Laser Deceleration of an Atomic Beam," *Phys. Rev. Lett.* **48** (1982) 596–599.

[29] M. Schioppo, *Development of a Transportable Strontium Optical Clock*. PhD thesis, University of Florence, 2010.

[30] T. A. Savard, *Raman Induced Resonance Imaging of Trapped Atoms*. PhD thesis, Duke University, 1998.

[31] J. Steinmann, *Multiphoton Ionization of Laser Cooled Lithium*. PhD thesis, Heidelberg University, 2007.

[32] I. Courtillot, A. Quessada, R. P. Kovacich, J.-J. Zondy, A. Landragin, A. Clairon, and P. Lemonde, "Efficient Cooling and Trapping of Strontium Atoms," *Opt. Lett.* **28** (2003) 468–470.

[33] M. Bober, J. Zachorowski, and W. Gawlik, "Designing Zeeman Slower for Strontium Atoms – Towards Optical Atomic Clock," `arXiv:1006.1554v1 [physics.atom-ph]`.

[34] S. C. Bell, M. Junker, M. Jasperse, L. D. Turner, Y.-J. Lin, I. B. Spielman, and R. E. Scholten, "A Slow Atom Source Using a Collimated Effusive Oven and a Single-Layer Variable Pitch Coil Zeeman Slower," *Review of Scientific Instruments* **81** 1, (2010) 013105.

[35] G. Scoles, *Atomic and Molecular Beam Methods*, vol. 1. Oxford University Press, 1988.

[36] M. A. Joffe, W. Ketterle, A. Martin, and D. E. Pritchard, "Transverse Cooling and Deflection of an Atomic Beam Inside a Zeeman Slower," *J. Opt. Soc. Am. B* **10** 12, (1993) 2257–2262.

[37] W. H. Press, B. P. Flannery, S. A. Teukolsky, and W. T. Vetterling, *Numerical Recipes in C: The Art of Scientific Computing*. Cambridge University Press, 1992.

[38] T. Bergeman, G. Erez, and H. J. Metcalf, "Magnetostatic Trapping Fields for Neutral Atoms," *Phys. Rev. A* **35** (1987) 1535–1546.

[39] J. Krieger, "Zeeman-Slower und Experimentsteuerung für das NaLi-Experiment," Master's thesis, Heidelberg University, 2008.

[40] Y. B. Ovchinnikov, "A Zeeman Slower Based on Magnetic Dipoles," *Optics Communications* **276** 2, (2007) 261–267.

[41] E. R. Eliel, W. Hogervorst, T. Olsson, and L. R. Pendrill, "High Resolution Laser Spectroscopy of Low-Lying *p*-States in Sr I and Ba I," *Zeitschrift für Physik A* **311** (1983) 1–6.

[42] W. Shao-Kai, W. Qiang, L. Yi-Ge, W. Min-Ming, L. Bai-Ke, Z. Er-Jun, L. Tian-Chu, and F. Zhan-Jun, "Cooling and Trapping ^{88}Sr Atoms with 461nm Laser," *Chinese Physics Letters* **26** 9, (2009) 093202.

[43] H. J. Metcalf and P. van der Straten, *Laser Cooling and Trapping*. Springer, 1999.

[44] A. D. Ludlow, *The Strontium Optical Lattice Clock: Optical Spectroscopy with Sub-Hertz Accuracy*. PhD thesis, University of Colorado, 2008.

[45] M. Yasuda and H. Katori, "Lifetime Measurement of the $^3P_2$ Metastable State of Strontium Atoms," *Phys. Rev. Lett.* **92** (2004) 153004.

[46] X. Xu, T. H. Loftus, J. L. Hall, A. Gallagher, and J. Ye, "Cooling and Trapping of Atomic Strontium," *J. Opt. Soc. Am. B* **20** 5, (2003) 968–976.

[47] B. Ueberholz, S. Kuhr, D. Frese, V. Gomer, and D. Meschede, "Cold Collisions in a High-Gradient Magneto-Optical Trap," *Journal of Physics B: Atomic, Molecular and Optical Physics* **35** 23, (2002) 4899.

[48] K. M. F. Magalhaes, S. R. Muniz, G. D. Telles, P. W. Courteille, V. S. Bagnato, and L. G. Marcassa, "The Escape Velocity in a Magneto-Optical Trap and its Importance to Trap Loss Investigation," *Laser Physics* **12** 1, (2002) 145–151. `http://cat.inist.fr/?aModele=afficheN&cpsidt=13785782`.

[49] T. W. Hänsch and B. Couillaud, "Laser Frequency Stabilization by Polarization Spectroscopy of a Reflecting Reference Cavity," *Optics Communications* **35** 3, (1980) 441–444.

[50] S. Mauger, J. Millen, and M. P. A. Jones, "Spectroscopy of Strontium Rydberg States Using Electromagnetically Induced Transparency," *Journal of Physics B: Atomic, Molecular and Optical Physics* **40** 22, (2007) F319.

[51] S. M. Abrarov, B. M. Quine, and R. K. Jagpal, "Rapidly Convergent Series for High-Accuracy Calculation of the Voigt Function," *Journal of Quantitative Spectroscopy and Radiative Transfer* **111** 3, (2010) 372–375.

[52] D. W. Allan, "Time and Frequency (Time-Domain) Characterization, Estimation, and Prediction of Precision Clocks and Oscillators," *IEEE Transactions on Ultrasonics, Ferroelectrics and Frequency Control* **34** 6, (1987) 647–654.

[53] O. Ishida, "Delayed-Self-Heterodyne Measurement of Laser Frequency Fluctuations," *Journal of Lightwave Technology* **9** 11, (1991) 1528–1533.

[54] H. Risken, *The Fokker-Planck Equation: Methods of Solutions and Applications*. Springer-Verlag, 1988.

[55] T. P. Dinneen, K. R. Vogel, E. Arimondo, J. L. Hall, and A. Gallagher, "Cold Collisions of Sr^*-Sr in a Magneto-Optical Trap," *Phys. Rev. A* **59** (1999) 1216–1222.

[56] T. Kurosu and F. Shimizu, "Laser Cooling and Trapping of Alkaline Earth Atoms," *Japanese Journal of Applied Physics* **31** (1992) 908–912.

[57] L. R. Hunter, W. A. Walker, and D. S. Weiss, "Observation of an Atomic Stark-Electric-Quadrupole Interference," *Phys. Rev. Lett.* **56** (1986) 823–826.

[58] J. Millen, *A Cold Strontium Rydberg Gas*. PhD thesis, Durham University, 2011.

[59] S. B. Nagel, *Ultracold Collisions in Atomic Strontium*. PhD thesis, Rice University, 2008.

[60] W. Ketterle, D. S. Durfee, and D. M. Stamper-Kurn, "Making, Probing and Understanding Bose-Einstein Condensates," `arXiv:9904034v2 [cond-mat]`.

[61] U. Dammalapati, I. Norris, C. Burrows, A. S. Arnold, and E. Riis, "Spectroscopy and Isotope Shifts of the $4s3d\,^1D_2 - 4s5p\,^1P_1$ Repumping Transition in Magneto-Optically Trapped Calcium Atoms," *Phys. Rev. A* **81** (2010) 023424.

[62] U. Dammalapati, I. Norris, C. Burrows, and E. Riis, "Laser Spectroscopy of the $4s4p\,^3P_2 - 4s3d\,^1D_2$ Transition on Magnetically Trapped Calcium Atoms," *Phys. Rev. A* **83** (2011) 062513.

[63] P. G. Mickelson, Y. N. M. de Escobar, P. Anzel, B. J. DeSalvo, S. B. Nagel, A. J. Traverso, M. Yan, and T. C. Killian, "Repumping and Spectroscopy of Laser-Cooled Sr Atoms Using the $(5s5p)\,^3P_2$-$(5s4d)\,^3D_2$ Transition," *Journal of Physics B: Atomic, Molecular and Optical Physics* **42** 23, (2009) 235001.

[64] S. Stellmer, R. Grimm, and F. Schreck, "Production of Quantum Degenerate Strontium Gases: Larger, Better, Faster, Colder," `arXiv:1212.2539v1 [cond-mat.quant-gas]`.

[65] M. Asano and K. Kubo, "Vapor Pressure of Strontium Below 660K," *Journal of Nuclear Science and Technology* **15** 10, (1978) 765–767.

[66] R. H. Dicke, "Coherence in Spontaneous Radiation Processes," *Phys. Rev.* **93** (1954) 99–110.

[67] M. Gross and S. Haroche, "Superradiance: An Essay on the Theory of Collective Spontaneous Emission," *Physics Reports* **93** 5, (1982) 301–396.

[68] D. Meiser, J. Ye, D. R. Carlson, and M. J. Holland, "Prospects for a Millihertz-Linewidth Laser," *Phys. Rev. Lett.* **102** (2009) 163601.

[69] D. Meiser and M. J. Holland, "Steady-State Superradiance with Alkaline-Earth-Metal Atoms," *Phys. Rev. A* **81** (2010) 033847.

[70] A.-C. Liao, W.-T. Ni, and J.-T. Shy, "Pico-Watt and Femto-Watt Weak-Light Phase Locking," *International Journal of Modern Physics D* **11** 07, (2002) 1075–1085.

[71] J. G. Bohnet, Z. Chen, J. M. Weiner, D. Meiser, M. J. Holland, and J. K. Thompson, "A Steady-State Superradiant Laser With Less Than One Intracavity Photon," *Nature Letters* **484** 7392, (2012) 78–81.

[72] E. D. Black, "An Introduction to Pound–Drever–Hall Laser Frequency Stabilization," *American Journal of Physics* **69** 1, (2001) 79–87.